DOKUZ EYLÜL UNIVERSITY
GRADUATE SCHOOL OF NATURAL AND APPLIED SCIENCES

A NUMERICAL AND EXPERIMENTAL STUDY ON ACTIVE COOLING SYSTEM AND POLYMER COMPOSITE LAMINATION OF PHOTOVOLTAIC-CELLS

by
Talha Batuhan KORKUT

July, 2023
İZMİR

A NUMERICAL AND EXPERIMENTAL STUDY ON ACTIVE COOLING SYSTEM AND POLYMER COMPOSITE LAMINATION OF PHOTOVOLTAIC-CELLS

A Thesis Submitted to the
Graduate School of Natural and Applied Sciences of Dokuz Eylül University
In Partial Fulfillment of the Requirements for Master of Science in
Department of Mechatronics Engineering Program

by

Talha Batuhan KORKUT

July, 2023

İZMİR

THESIS EXAMINATION RESULT FORM

We have read the thesis entitled **"A NUMERICAL AND EXPERIMENTAL STUDY ON ACTIVE COOLING SYSTEM AND POLYMER COMPOSITE LAMINATION OF PHOTOVOLTAIC-CELLS"** completed by **TALHA BATUHAN KORKUT** under supervision of **ASSOC. PROF. DR. AYTAÇ GÖREN** and we certify that in our opinion it is fully adequate, in scope and in quality, as a thesis for the degree of Master of Science.

Assoc. Prof. Dr. Aytaç GÖREN

Supervisor

Prof. Dr. Can Özgür ÇOLPAN

Jury Member

Assoc. Prof. Dr. Koray ÜLGEN

Jury Member

Prof. Dr. Okan FISTIKOĞLU

Director

Graduate School of Natural and Applied Sciences

ACKNOWLEDGMENT

First of all, I would like to thank my advisor Assoc. Prof. Dr. Aytaç GÖREN who supported and guided me throughout this study. Also, I would like to thank Prof. Dr. Ahmed RACHID from Université de Picardie Jules Verne (UPJV) for his support and experience in the Laboratory of Innovative Technologies (LTI).

I sincerely thank my colleague Zeynep PASİNLİ for her support in the preparation and implementation of the experimental environment, besides encouraging me in every part of my life.

I would like to thank Halis KANDAŞ for his support in the polymer matrix composites, and production methods.

Lastly, I would also like to thank my cat for all the entertainment and emotional support.

Talha Batuhan KORKUT

A NUMERICAL AND EXPERIMENTAL STUDY ON ACTIVE COOLING SYSTEM AND POLYMER COMPOSITE LAMINATION OF PHOTOVOLTAIC-CELLS

ABSTRACT

One of the renewable energy types, solar energy, is widely used in various fields. Especially in recent years, besides solar farms, it has become increasingly common in areas related to building-related needs and public transportation. Solar energy is converted into two useful forms, electrical and thermal, in photovoltaic (PV) cells. Therefore, in academic studies, diverse studies are carried out on increasing the electrical efficiency of PV cells and the use of thermal energy produced, especially in residences or industrial areas.

In the present study, fiber-reinforced polymer matrix composite (FRPMC) materials and the vacuum-assisted resin transfer molding (VARTM) method have been investigated to perform the lamination of photovoltaic cells. Also, an improved active cooling system with a thermally conductive material such as carbon fiber has been designed and combined with the laminated PV module. Laminated photovoltaic/thermal (PV/T) and PV modules have been operated in February, March, and April 2023 to the definition of the performances and differences between each other. During experiments, weather conditions, temperatures of the PV/T and PV modules, and inlet and outlet temperatures of the active cooling system have been logged. Except for the experiments, a computational fluid dynamics (CFD) model has been implemented, simultaneously for the verification of the numerical model and the definition of the average error rate for future studies. For the CFD model, the realizable k-ε turbulence model and SIMPLE scheme have been preferred to determine the high flow rates and pressure-velocity coupling.

Keywords: Photovoltaic/thermal system, lamination, polymer matrix composite, cfd

FOTOVOLTAİK HÜCRELERİN AKTİF SOĞUTMA SİSTEMİ VE POLİMER KOMPOZİT LAMİNASYONU ÜZERİNE SAYISAL VE DENEYSEL BİR ÇALIŞMA

ÖZ

Yenilenebilir enerji türlerinden biri olan güneş enerjisi, çeşitli alanlarda yaygın olarak kullanılmaktadır. Özellikle son yıllarda güneş enerjisi santrallerinin yanı sıra bina ile ilgili ihtiyaçlar ve toplu taşıma ile ilgili alanlarda giderek yaygınlaşmaya başlamıştır. Güneş enerjisi, fotovoltaik (PV) hücrelerde elektriksel ve termal olmak üzere iki faydalı forma dönüştürülür. Bu nedenle akademik çalışmalarda özellikle konutlarda veya endüstriyel alanlarda PV hücrelerin elektriksel verimlerinin arttırılması ve üretilen ısıl enerjinin kullanılmasına yönelik çeşitli çalışmalar yapılmaktadır.

Bu çalışmada, fotovoltaik hücrelerin laminasyonunu gerçekleştirmek için fiber takviyeli polimer matris kompozit (FRPMC) malzemeler ve vakum destekli reçine transfer kalıplama (VARTM) yöntemi araştırılmıştır. Ayrıca, karbon fiber gibi termal olarak iletken bir malzeme ile geliştirilmiş bir aktif soğutma sistemi tasarlanmış ve lamine PV modülü ile birleştirilmiştir. Lamine fotovoltaik/termal (PV/T) ve PV modülleri, performansları ve aralarındaki farklar belirlenecek şekilde Şubat, Mart ve Nisan 2023'te çalıştırılmıştır. Deneyler sırasında hava koşulları, PV/T ve PV modüllerinin sıcaklıkları ve aktif soğutma sisteminin giriş ve çıkış sıcaklıkları kaydedilmiştir. Deneyler dışında, sayısal modelin doğrulanması ve gelecekteki çalışmalar için ortalama hata oranının tanımlanması için eş zamanlı olarak bir hesaplamalı akışkanlar dinamiği (CFD) modeli uygulanmıştır. CFD modeli için, yüksek debileri ve basınç-hız bağlantısını belirlemek için gerçekleştirilebilir k-ε türbülans modeli ve SIMPLE şeması tercih edilmiştir.

Anahtar kelimeler: Fotovoltaik/termal sistem, laminasyon, polimer matris kompozit, had

CONTENTS

Page

LIST OF FIGURES

Page

LIST OF TABLES

Page

LIST OF SYMBOLS

I_{solar}	:	Solar Radiation (W/m^2)
t_{PV}	:	Thickness of the PV cell (mm)
q_{conv}	:	Convective heat transfer (W)
q_{rad}	:	Radiative heat transfer (W)
q''	:	Heat flux (W/mm^2)
ε	:	Emissivity constant
σ	:	Stefan-Boltzmann constant
T_{surf}	:	Surface temperature (°C)
T_{sky}	:	Sky temperature (°C)
T_{amb}	:	Ambient temperature (°C)
T_{avg}	:	Average temperature (°C)
T_{ref}	:	Reference temperature of the PV cell (°C)
T_g	:	Glass transition temperature (°C)
T_{in}	:	Water inlet temperature in the active cooling system (°C)
T_{out}	:	Water outlet temperature in the active cooling system (°C)
T_{max}	:	Maximum temperature (°C)
T_{min}	:	Minimum temperature (°C)
h_{total}	:	Total heat transfer coefficient ($W/m^2°C$)
$h_{natural}$	:	Natural convection ($W/m^2°C$)
h_{forced}	:	Forced convection ($W/m^2°C$)
V_{wind}	:	Wind speed (m/s)
η_e	:	Electrical efficiency of the PV cell
η_{ref}	:	Reference efficiency of the PV cell
η_{th}	:	Thermal efficiency of the PV/T
η_{total}	:	Total efficiency of the PV/T
A_s	:	PV surface area (m^2)
β_{PV}	:	Temperature coefficient of the PV cell
α_{PV}	:	Absorptivity of the PV cell
τ_{PV}	:	Transmissivity of the PV cell

$\dot{Q}$	:	Thermal power
D_{in}	:	Inner diameter of the cooling channel (mm)
D_{out}	:	Outer diameter of the cooling channel (mm)
R_{total}	:	Total thermal resistance ($°C/W$)
R_{layer}	:	Thermal resistance of the layer ($°C/W$)
c_p	:	Specific heat capacity ($J/kg°C$)
ρ	:	Density (kg/m^3)
k	:	Heat conduction coefficient ($W/m°C$)
μ_t	:	Turbulent viscosity (kg/ms)
K_r	:	Ratio of the total radiation on the horizontal to the extraterrestrial radiation
$	:	Dollar currency

ABBREVIATIONS

ACRL	:	Automatic Control and Robotics Labs
ARC	:	Anti-Reflective Coating
AT	:	Ambient Temperature
BC	:	Boundary Condition
CFD	:	Computational Fluid Dynamics
CS	:	Clock Speed
CV	:	Current Voltage
D	:	Diameter
DC	:	Direct Current
DEU	:	Dokuz Eylul University
EV	:	Electric Vehicle
EVA	:	Ethylene Vinyl Acetate
EXP	:	Experimental
FEM	:	Finite Element Method
FRPMC	:	Fiber-Reinforced Polymer Matrix Composite
GB	:	Gigabyte
GEM	:	Generated Energy Meter
HTP	:	Heat Transfer Performance
IV	:	Input Voltage
LiFePO4	:	Lithium Iron Phosphate
Li-Ion	:	Lithium Ion
LiPo	:	Lithium Polymer
MAX	:	Maximum
MIN	:	Minimum
MPPT	:	Maximum Power Point Tracker
MDOT	:	Mass Flow Rate
NiMH	:	Nickel Metal Hydride
NU	:	Nusselt Number
NUM	:	Numerical
OT	:	Operating Temperature

OV	:	Operating Voltage
Prepreg	:	Pre-Impregnated
PC	:	Personal Computer
PV	:	Photovoltaic
PV/T	:	Photovoltaic/Thermal
RAM	:	Random Access Memory
RE	:	Reynolds Number
RES	:	Renewable Energy Sources
RF	:	Radio Frequency
RTC	:	Real-Time Clock
SD Card	:	Secure Digital Card
SE	:	Solar Energy
Si	:	Silicon
SR	:	Solar Radiation
S2S	:	Surface to Surface
TDIST	:	Temperature Distribution
UV	:	Ultraviolet Radiation
VARTM	:	Vacuum Assisted Resin Transfer Molding
WS	:	Wind Speed
3D	:	Three Dimensional
2D	:	Two Dimensional

CHAPTER ONE
INTRODUCTION

1.1. Introduction

Contemporarily, climate change's effects are increasing daily, and one of the reasons has been seen as global carbon emission rates which could be mitigated by employing renewable energy sources (RES). One of the RES, solar energy (SE) plays a key role and is usually converted into two useful forms of electricity and heat by photovoltaic (PV) cells, principally (Prasad, et al., 2017). Today, the use areas of PVs getting increasing. For instance, it is also an electricity and thermal energy source for industry and residences. Besides, electric vehicles (EVs) which charging by PV modules started to present their use by humanity. Common PV usage areas are known as electricity sources for industries, residences, or space stations. Today, PVs are started to be common in different areas such as transportation, military uses, and stand-alone power. Some of the PV use areas have been shown in Figure 1.1.

(a) New generation EVs.

(b) Transportation.

(c) Military use.

(d) Power in space.

Figure 1.1 Different implementations of photovoltaics (PVs).

The electrical conversion efficiency of PV cells could be improved by mitigating their average temperature. Thus, thermally developed PV cells namely photovoltaic/thermal (PV/T) technology, had been started deeply investigated end of the 70s (Zondag, 2008). PV is the conversion of light into direct current (DC) electrical energy using semiconductor materials. The semiconductor layer engages photons, which boosts the energy level of the electrons there. The negative layer is where free electrons shift here, where they are used to cause electricity. Although PV cells have the ability to absorb a high amount of energy, their electrical conversion efficiency currently varies between 7% and 40% (Makki, et al., 2015; Joshi and Dhoble, 2018; Green, et al., 2021). Among the parameters affecting the performance of PV cells are the material of the PV cell, the operating temperature (OT), and the coefficients originating from some manufacturing methods (Nahar, et al., 2017). Over the years, the electrical performance of PV cells has been studied and studies have been carried out on their thermal development. Studies on PV/T have progressed on three main topics. These are grid-connected applications, autonomous systems, and concentrator PV (Zondag, 2008). Related studies have been seen as an incentive at the beginning of the 1990s to increase the performance of PV cells, as well as to use the thermal energy obtained for residences. The critical triangle for PVs has been shown in Figure 1.2. Ideally, the best lifetime, electrical efficiency, and cost are expected from PVs (Giannouli, et al., 2015). However, as seen in Figure 1.2, this is not possible in practice. For this reason, research studies also focused on obtaining optimum efficiencies besides improving lifetime and costs.

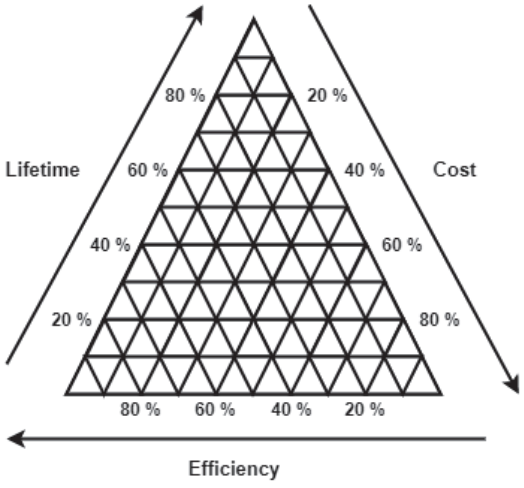

Figure 1.2 A critical triangle graph for the PV cell.

This study focused on the new type of lamination for PV cells means obtaining different heat transfer performances (HTP) from conventional PV cells. After the lamination phase of the present research, this indicated HTP difference has also been compared with and without thermally developed PV cells. The purpose of the study has also been discussed in subsection 1.3.

1.2. Literature Review, Theory

As the temperature of PV cells increases, their electrical efficiency (η_e) and generated electrical energy decrease. Previous research studies focused on varying electrical efficiencies of PV cells under changing operating conditions with respect to developed mathematical models. Besides, active and passive cooling systems have been integrated into PV modules in order to keep the temperatures of PV modules in the efficient range. While all these studies were carried out, energy production was monitored according to the changing months and energy saving in economic terms was investigated.

The thermal (η_{th}) and η_e of PV/Ts with different absorber designs (serpentine, u-flow, and spiral types) with different mass flow rates (MDOT) have been investigated by Rosli et al (2018). During numerical (NUM) studies, the radiation between PV module and air has been modeled with the surface to surface (S2S) model (Rosli, et al., 2018). Nahar et al. developed a three-dimensional (3D) numerical PV/T model which has a pancake-shaped absorber design that is attached to the PV module with the usage of thermal paste. Governing equations have been computed numerically by using Galerkin's weighted residual finite element method (FEM). Indicated PV/T module has been investigated under diverse velocities up to 0.05 m/s. End of the study, temperatures of PV and PV/T modules have been found to be increased approximately by 5.4 °C and 9.2 °C for every 100 W/m^2 increase in solar radiation (SR) level, respectively (Nahar, et al., 2017). New absorber design configurations have been investigated by Ibrahim et al. under different SR, ambient temperature (AT), and MDOT conditions. Consequently, the spiral-shaped absorber design has been found as the best efficient design and it has been declared that the η_{th} of the improved PV/T module has reached 50.12% (Ibrahim, et al., 2009). Effects of laminar and turbulent flow regimes/characteristics on the thermal side of hybrid PV modules with and

without glass covers have been focused on by Yazdanifard et al. under different parameters such as SR, Reynolds number (RE), and some physical constraints. In most cases, it has been seen that the total energy efficiency was higher in turbulent regimes. Besides the investigation of the performances of PV/T modules, the error rate of the NUM model has been obtained with respect to experiments (Yazdanifard, et al., 2016). Tse et al. have aimed to indicate the profits of implementing a PV/T system in a real office scale building via computer program simulations. Following that, they have analyzed economic profits between PV/T and the conventional PV systems (Tse, et al., 2016). Skoplaki and Palyvos have investigated the convenient temperature dependence of η_e and, equivalently, solar power and presented it in algebraic forms. Finally, the thermal aspects of the major power/energy rating methods are briefly discussed (Skoplaki and Palyvos, 2009). Cattani (2012) focused on the influence of the curvature profile on the convective heat transfer mechanism. Besides the performances of the geometry, friction factor and Nusselt number (NU) have been investigated. End of the study, flow patterns, and tube sections under different REs have been investigated with respect to changing η_e of PV modules (Cattani, 2012). Predicting the monthly and the long-term average electrical output of PV arrays has been investigated by Evans, and the procedure implemented in the study has been combined with the mean local temperature and K_r parameters (Evans, 1981). The maximum (MAX) yield of different PV/T module designs has been investigated in order to the definition of divergence by Zondag et al. In the other study, they prepared a historical overview of PV/T modules in the form of a thematic overview, addressing the different research issues of PV/T (Zondag, et al., 2003; Zondag, 2008). Misha et al. focused on the new type of dual oscillating pipeline flow design for water-based PV/T modules. The new cooling system design has also been investigated under different MDOT values and weather conditions. Besides experiments, the PV/T module has been modeled in 3D and implemented under a numerical model to validate experimental (EXP) results. The MAX average η_{th} of the PV/T module design has reached 59.6% and the MAX average η_e of PV and PV/T modules have been found at 10.86% and 11.73% (Misha, et al., 2020). In another study, the two different types of PV cells (mono and multi-crystalline) have been investigated by Dubey and Tay (2013). EXP studies have been implemented under typical day climate conditions and

validated with the basic energy balance equations and design parameters. It was found that the average η_e difference between PV/T and PV modules was about 0.4% (Dubey and Tay, 2013). In a similar study, Atmaca and Pektemir (2019) designed two different hybrid PV modules. The water heat exchanger was used in the first PV/T system. Two different heat exchangers which operate with water and air were used for the second PV/T system. PV/T systems were compared with the PV system simultaneously. At the end of the study, it has been seen that the combination of two different coolants, water and air, is more efficient than the single coolant type usage in a hybrid PV module (Atmaca and Pektemir, 2019). Charalambous et al. focused on the optimization of PV/T collector absorber. To predict and validate the performance of configurations, EES code has been developed. It was found that 40.50% less material was used in the redesigned absorber (Charalambous, et al., 2011). Hussain et al. studied the η_{th} of hexagonal honeycomb type absorber plate. It was found that the η_{th} of the system without honeycomb is 27% and with is 87% (Hussain, et al., 2015). Gang et al. developed a new type of heat-pipe PV/T module which can provide electricity and thermal energy simultaneously. Experiments have been validated with the developed NUM model and results showed that the PV/T module can be used under cold weather conditions also. Daily η_{th} and η_e efficiencies of the PV/T system were found as 41.9% and 9.4% (Gang, et al., 2011). Tripanagnostopoulos et al. focused on the hybrid PV/T solar systems. End of the study, it was found that thermal output can be improved by using additional glazing, and a booster diffuse reflector (Tripanagnostopoulos, et al., 2002).

1.3. Purpose of the Study

The aim of this study includes two different topics and one of the topics is the lamination of PV cells using polymer matrix composite (PMC) materials. The second topic of the current study is the investigation of the generated electrical energy values of PV modules laminated with FRPMC materials with and without thermal development and their comparisons. Besides the EXP investigations of PV modules, a NUM model has been developed and obtained the error rate with respect to outcomes from experiments. The steps of the present research have been summarized in the list below.

- Clarification of the required equipment and working conditions for the implementation of the lamination of PV modules.
- The investigation of FRPMC materials with respect to their thermophysical and optical properties under indicated research limitations.
- After the identification of FRPMC materials, the lamination of PV module methods has been investigated. With respect to the decided lamination method, tools, and materials have been supplied. Also, the manufacturing environment has been prepared.
- Measurement parameters and instruments have been defined. Measurement instruments have been developed to measure ambient temperature (AT) (°C), solar radiation (SR) (W/m^2), and wind speed (WS) (km/h), besides the generated electrical energy of the laminated PV and PV/T modules.
- The developed computational fluid dynamics (CFD) model has been implemented for the validation of energy generations with error rates of PV and PV/T modules to do further generated electrical energy estimation under changing operational conditions.

The satellite photo of the experimental environment has shown in Figure 1.3. In this Figure, laminated PV and PV/T modules have been placed on the roof side of the Desarj 3 contained which is indicated in the red box. Measurement systems have also been placed in this container. Numerical studies have been performed via logged experiment measurements in the Automatic Control and Robotics Labs (ACRL) which is indicated as the yellow box in Figure 1.3.

Figure 1.3 Satellite photo of the experimental environment (Desarj 3).

The present study has been implemented under limited conditions and has some assumptions for the numerical model. Research limitations have been indicated below.

- Economical: Experimental environment and measurement instruments have been implemented under a limited budget (335 $). 120 $ for PMC materials, 150 $ for the measurement instruments, 50 $ for the workmanship source, and 15 $ for the active cooling system have been disbursed.
- Computational: Numerical studies have been implemented under limited software packages and computational hardware (Intel(R) Core(TM) i7-8565U, 32 GB RAM).
- Operational: Experiments have been implemented for one day of these months: February, March, and April 2023.

CHAPTER TWO
METHODOLOGY

2.1 Photovoltaic Cells

The photovoltaic (PV) effect is a process that generates a current in a PV cell when it is exposed to sunlight. The PV effect was first discovered in 1839 by Edmond Becquerel. PV cells are made up of p-type and n-type semiconductors that are fused together to form a p-n junction (Figure 2.1). In the junction area created by the merging of these two semiconductor types, an electric field is created as electrons flow to the positive p-side and holes move to the negative n-side. Positively charged particles flow in the opposite direction from negatively charged particles as a result of this field (Palz, 2010).

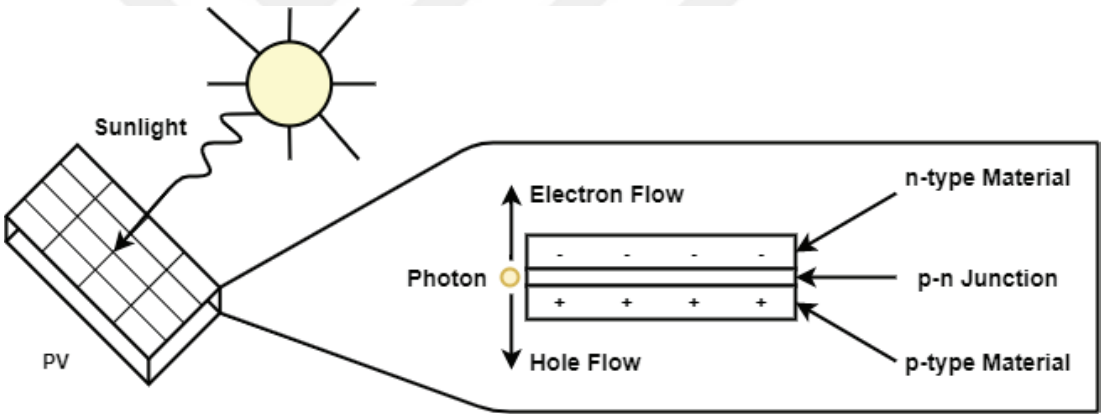

Figure 2.1 A schematic diagram of the photovoltaic effect (Palz, 2010).

The photon's energy is transmitted to an atom of the semiconductor material in the p-n junction when enough wavelengths of light strike these cells. The electrons in the substance receive the energy in a certain way. The electrons' energy rises, reaching the conduction band as a consequence. The consequence is a hole in the valence band where the electron jumped up from. When the electron travels as a result of the additional energy, an electron-hole pair is created (Everett, et al., 2012). The PV cell typically acts as a continuous current source whose output is exactly proportional to the amount of light hitting it. Figure 2.2 depicts the electrical equivalent of a PV cell.

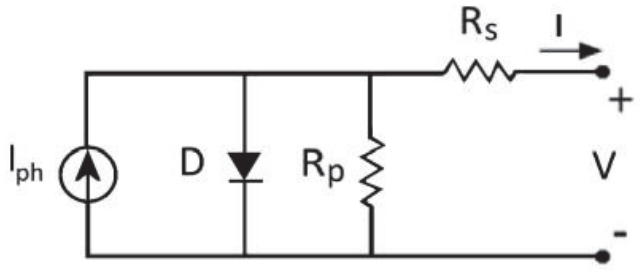

Figure 2.2 PV cell single diode module.

PV cells made of silicon (Si) are categorized into single and multi-crystalline varieties, respectively. Presently, the electrical efficiency (η_e) range of Si-based PV cells without concentrators is between 14 to 26.7% (Levi, et al., 2017). Equation 2.1 defines the amount of current shifting into the external circuit besides the definition of the efficiency loss of the PV module (Gören, 2017). The current generation rate from PV cells is assumed to be constant and directly proportional to the light. The temperature of the cell affects η_e in addition to the condition of exposed illumination. When Equation 2.1 is taken into account, it is clear that when the temperature rises, the output current of the cell lowers and the efficiency falls.

$$I = I_L - I_S * \left[e^{(q/nKT_C)(V+IR_S)} - 1\right] - \frac{V + IR_S}{R_P} \tag{2.1}$$

A silicon module's typical features are shown in Figure 2.3 and Figure 2.4. These curves are generated by manufacturers at ideal conditions (1000 W/m^2 and 25 °C). In general, PV cells are regarded as a constant current source. As can be seen from these figures, cell current increases directly with solar radiation (SR), and temperature increase decreases the maximum (MAX) power of the PV cells (Gören, 2017). The AM 1.5 Standard defines how to test the performance of PV cells and relates to two common terrestrial sun spectrum irradiance spectra. Reference spectra are produced using the BRITE radiative transfer model (Myers, et al., 2004; Blättner, 1983). The performance of several PVs is compared using reference spectra. Modeling is done for the worldwide AM 1.5 standard spectrum using a sun-facing collector surface that is 37° inclined from the horizontal. A 5.8° field of view with the sun directly overhead is used to mimic the direct AM 1.5 spectrum.

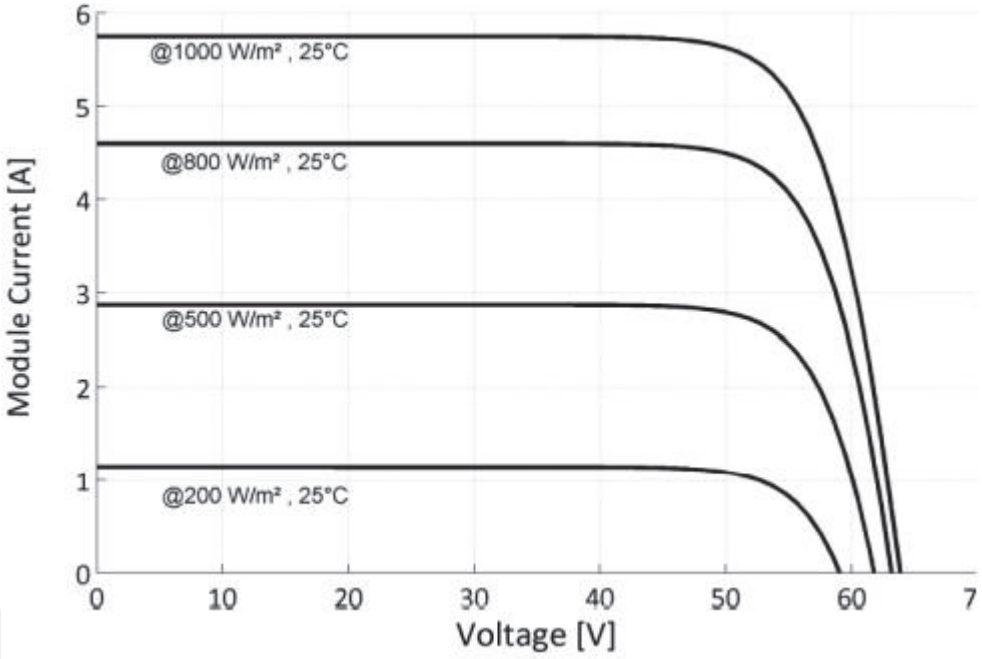

Figure 2.3 I-V curve of a serially linked PV cell module.

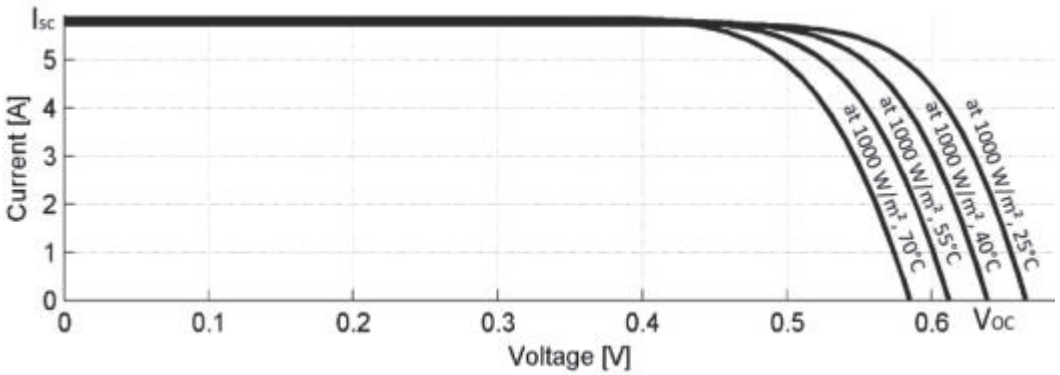

Figure 2.4 A PV cell's I-V curve at various cell temperatures.

2.2 Polymer Matrix Composite Materials

An organic polymer matrix holds a variety of short or continuous fibers together to form a fiber-reinforced polymer matrix composite or FRPMC. FRPMCs have certain benefits. These include low specific weight, good corrosion resistance, shapability, and appealing optical qualities (Goren and Atas, 2008). FRPMCs have two main

components named matrix and dispersed, and this section has considered these components separately.

2.2.1 Matrix Materials

The purpose of the matrix in FRPMCs is to bond the dispersed fibers together and the matrix provides some abilities such as transferring mechanical loads that the related structure is exposed to between the dispersed fibers. In polymer, matrix materials are classified into two main types. These are organic and inorganic matrix materials (Elsanadedy, et al., 2019). The present study focused on organic matrix materials and has been divided into four different types.

- Epoxy resin is generally used for structural assemblies or structural matrix material in the aerospace industry. Besides, after the curing process of epoxy resin, looks the matrix material getting transparent (Jin, et al., 2015).
- Most of the polyester resins look yellowish in color. Additionally, polyester resins are frequently coated since they have a propensity to degrade over time and are UV-sensitive. It is often used in the construction of surfboards and for marine applications.
- Vinyl ester resin is more translucent and has a lower viscosity than polyester resin. It is more flexible and exhibits less deterioration over time than polyester resin. Vinyl ester resin is typically thought of as fuel-resistant (Launikitis, 1982).
- Shape memory polymer resins are those substances that can be heated above their glass transition temperature to form and change on a regular basis. When heated, they become elastic and flexible, making configuration simple, and when cooled, they hold their new shape (Liu, et al., 2007).

Matrices are also classified as thermosets and thermoplastics. To create a cured or completed product, thermoset matrices require the addition of a curing agent or hardener, impregnation onto a reinforcing material, and a curing phase. The FRPMC industry's current share of thermoplastics is quite minor. They are normally supplied as non-reactive solids, which means that no chemical reactions take place during processing; all that is needed to make the completed item is heat and pressure. In

contrast to thermosets, thermoplastics may frequently be warmed and reshaped if needed (Pilato and Michno, 1994; Campbell Jr, 2003).

If the matrix material is a type of thermoset, another important phase of FRPMC material production is the curing process and uncured epoxy resins mean to have poor mechanical and heat resistance properties in chemical science. Epoxy resins should be interacting with curatives to create three-dimensional (3D) cross-linked thermoset structures in order to acquire the desired characteristics. This process is generally called as curing phase of the production. Besides, an exothermic reaction happens during the curing phase of production. Heat transfer between the product and environment during the curing process should be checked to prevent thermal degradation (Takeichi and Furukawa, 2012; Hakiki, et al., 2015). The curing phase of the epoxy resins starts with a suitable substance, a hardener. Hardeners classify into six different types amines, acids, acid anhydrides, phenols, alcohols, and thiols (Hara, 1990). The curing temperatures of epoxy resin with hardener are generally seen to vary between room temperature and 200 °C. Insufficient heat energy during the curing will result in problems with incomplete polymerization and thus unexpected mechanical, chemical, and heat resistance. The range of temperatures across which this glass transition happens is defined by a material's glass-transition temperature (T_g), and the cure temperature should reach the T_g (DiBenedetto, 1987).

The present research decided to use epoxy resin. While searching for epoxy resins, attention was paid to the technical requirements of the product as well as the economical in terms of prices. Thus, a thermoset epoxy resin (Product name F 1564) provided by a company (Fibermak Composites) has been used. F 1564 epoxy resin has 70-75 MPa tensile stress, and 100-125 MPa bending stress. Besides indicated stresses, transition temperatures are 65-70 °C at 50 °C (12 hours), 80-85 °C at 80 °C (4 hours), and 80-85 °C at 100 °C (2 hours). The epoxy resin which is preferred used for the lamination of PV modules is suitable for laminating systems with low viscosity and high flexibility. Also, it has long pot life during production and is clear colorless to slightly yellow liquid. The extended technical properties of matrix material have shown in Table 2.1.

Table 2.1 Technical properties of the preferred matrix material (F 1564 Epoxy Resin).

		Epoxy Resin	**Hardener**
Viscosity		1250 – 1450 MPa s	30 – 70 MPa s
Density		1.1 – 1.2 g/cm^3	0.98 – 1.0 g/cm^3
Epoxy Index		5.8 – 6.05 Eq/kg	9.3 – 10.2 Eq/kg
Appearance		Clear liquid.	Clear to slightly yellow.
Mixing Ratio (part by weight)		100:34	
Transition Temperatures		**Mechanical Properties (80 °C – 4 hours)**	
25 °C (4 days)	48 – 52 °C	Tensile Strength	70 – 74 MPa
50 °C (12 hours)	65 – 70 °C	Tensile Comp. Modulus	2850 – 3000 MPa
80 °C (4 hours)	80 – 85 °C	Bending Stress	110 – 125 MPa
100 °C (2 hours)	80 – 85 °C	Bending Modulus	2800 – 3000 MPa

2.2.2 Dispersed Materials

Within the scope of this thesis, it is aimed to laminate PV cells with the use of FRPMC materials. In this context, FRPMC materials have been classified and the dispersed material suitable for the intended use was determined. Low specific weight, resistance to corrosion, ease of forming, and correct optical properties are expected from a laminated PV module. As stated in previous sections, FRPMC materials can meet these technical requirements. Under this objective, dispersed materials are classified into three different types themselves and schematic illustrations of dispersed materials have shown in Figure 2.5. These are fibers, carbon nanotubes, and graphene. Fibers have lower stiffness but good tensile strength. Because of their remarkable inherent mechanical qualities and low densities, carbon nanotubes have been the subject of much research. One type of material that has some of the greatest observed tensile stiffnesses and strengths is carbon nanotubes. But, research on graphene materials continues.

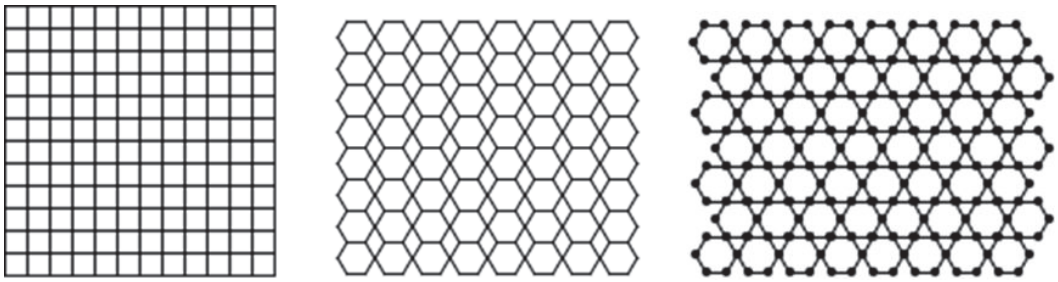

(a) Fibers. (b) Carbon Nanotubes. (c) Graphene.

Figure 2.5 Schematic illustration of dispersed fibers.

Except for dispersed materials mentioned above, prepregs have also wide application areas, especially in the production industry such as aviation and space. Prepreg means pre-impregnated fibers and it is known as partially cured polymer matrix materials (Chawla, 2012). Therefore, the prepreg materials do not need to have any additional matrix material during manufacture. Dispersed and matrix material ratio is one of the important parameters affecting the strength of FRPMC materials and this ratio is easily provided with prepregs because prepregs are already pre-impregnated. Prepregs can be processed with the hot-pressing technique or the autoclave technique (Murashov, 2012). An example of the autoclave technique of plate production with prepreg has shown in Figure 2.6 and Figure 2.7.

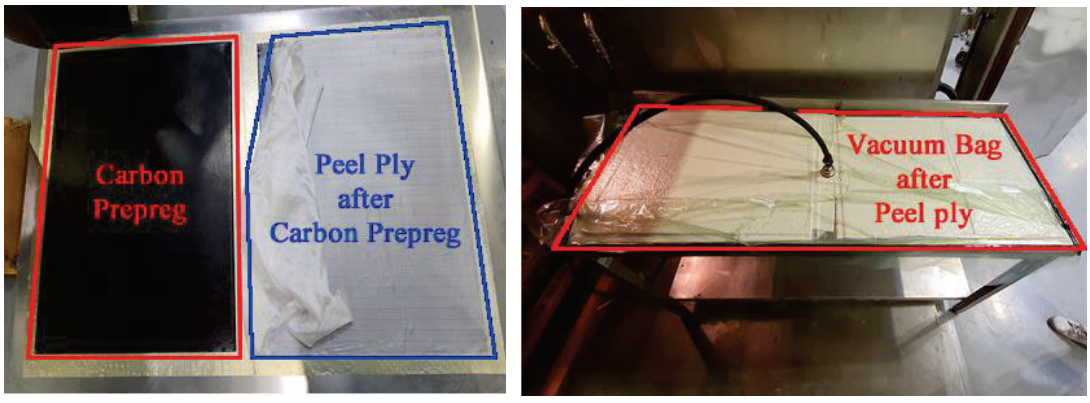

(a) Preparation of prepreg layers. (b) Preparation of vacuum sealing to autoclave.

Figure 2.6 An example for carbon prepreg plate production with autoclave technique.

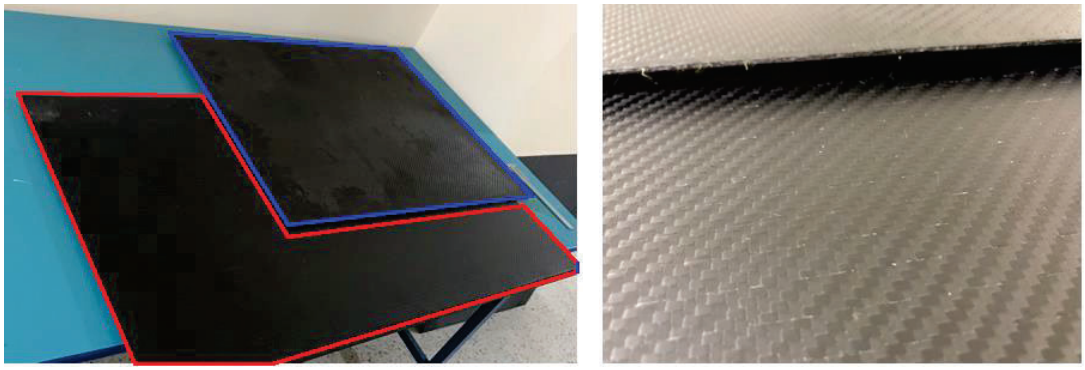

(a) Produced carbon prepreg plates. (b) A close look to weave pattern.

Figure 2.7 Produced carbon prepreg plate.

Within the scope of this research study, three different fiber materials have been focused on. These fibers are glass fiber, carbon fiber, and Kevlar. Considering its electrical insulating property, carbon fiber is an electrical conductor and carbon fiber is not suitable for lamination, because of the electrical conduct ability of PV modules (Bhatt and Goe, 2017). Considering the light transmittance parameter, Kevlar is not the right option for the lamination of PV modules, because the light transmittance of Kevlar is lowest in fiber materials (Mera and Takata, 2000). Only glass fiber remains after the light transmittance and electrical insulation abilities from dispersed materials. Glass fiber is categorized into five different types. It is classified as A-glass, C-glass, E-glass, AE-glass, and S-glass. Alkali glass is another name for A-glass. A-glass fiber resembles window glass in several ways and is chemically resistant. Equipment for processes is made with it. Chemical glass is another name for C-glass. C-glass has excellent chemical impact resistance. Alkali-resistant glass, or AE-glass. The mechanical characteristics of S-glass, also known as structural glass, are what make it useful (Zweben, 2005). E-glass is also called electrical glass. E-glass is an excellent insulator of electricity (Zweben, 1998). Because of electrical insulation properties, e-glass fibers have been preferred to be used for the lamination of PV modules. E-glass fibers have different weaving patterns as shown in Figure 2.8, these are

- Plain Weave: This type of weave pattern is known as the most basic type of fabric weave pattern. A plain weave creates a crisscross pattern that results in a fabric that

is incredibly strong, adaptable, and durable. Besides, it has high density and it means a stable weave.

- Twill: The most popular type of weave used to make textiles is twill. By alternately passing the weft yarn under and over many warp threads, this sort of weave produces a pattern of diagonal lines or ribs. The twill weave pattern is more pliable and drape than the plain weave. Therefore, twill weaves can be used for applications requiring strength in construction.
- Satin: Satin weaves have the appearance of silky, smooth cloth. This fabric's flexibility and pliability make it simple to shape it to the curved shapes found in reinforced plastics.
- Basket: Contrary to plain weave, basket weave weaves two or more warp and weft threads together into a single fabric. As a result, the cloth becomes more textured and has a checkerboard pattern that is more obvious. Compared to the plain weave, the basket weave is flatter, stronger, and more flexible, but not quite as substantial.
- Leno: Leno weaves work well in situations when lighter aerial weights are required, but certain thicknesses must be maintained. In addition to determining the bond line thickness for tapes and adhesives, Leno weave is frequently utilized in construction applications.

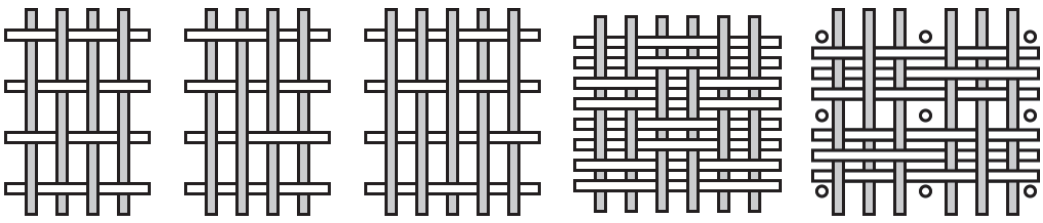

(a) Plain Weave. (b) Twill. (c) Satin. (d) Basket. (e) Leno.

Figure 2.8 A schematic illustration of different fabric weave patterns (Qureshi, 2020).

Different materials and their comparison under different parameters such as tensile strength, refractive index, density, and cost have shown in Figure 2.9. This study aims to laminate PV modules with an FRPMC material that has a low cost, refractive index, density, and high tensile strength material. Aluminum and stainless steel have low

costs and high densities than dispersed materials. Also, these two materials are heavier than fiber-dispersed materials. Thus, this study focused on fiber-dispersed materials. Kevlar is the most expensive material. Besides that, the average cost and refractive index values of glass fiber are less than other fiber-dispersed materials. Also, glass fiber is an electrically insulated material.

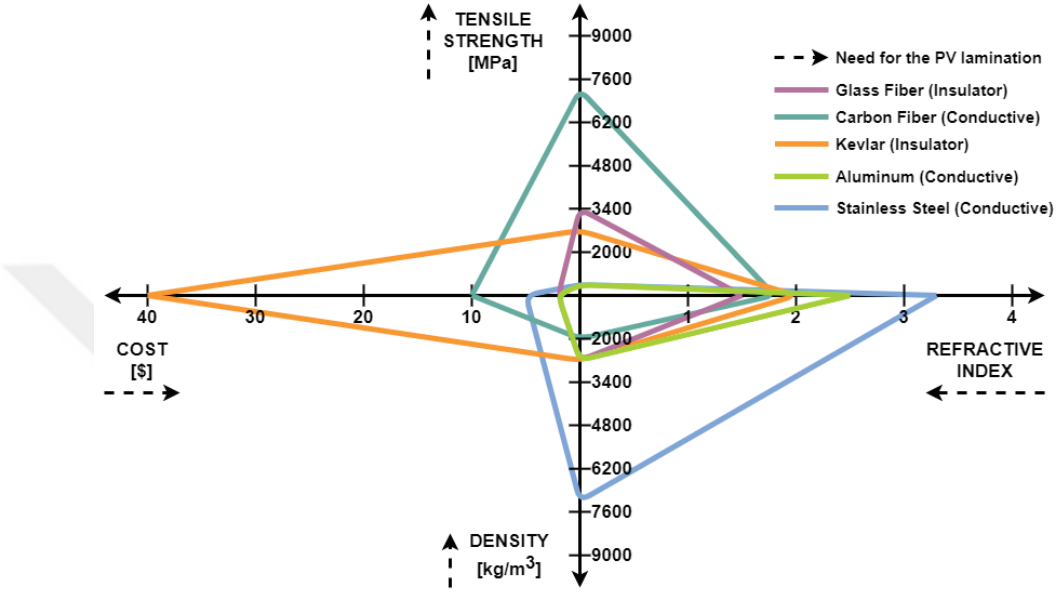

Figure 2.9 Comparison of materials under different parameters such as cost, refractive index, density, and tensile strength (Moosmüller, et al., 2021; Nishimura and Morishita, 1997; Hegedus, et al., 2017).

It was decided that the usage of seamless glass fiber in the current research. Besides, the preferred glass fiber has a density of 25 g/m^2.

2.3 Heat Transfer Performance of PMC Materials

This study has focused on three different dispersed materials as carbon fiber, glass fiber, and Kevlar. Thermophysical properties of FRPMC materials are as important as mechanical or physical properties. For this reason, a numerical (NUM) investigation of the heat transfer performance (HTP) of FRPMC materials has been implemented under different layer thicknesses and compositions before the lamination of PV modules to obtain the optimum HTP on the PV module.

Thermal conductivity could be defined as the measure of the ability to the conduction of heat and the substance's "specific heat capacity" is calculated by

dividing its "heat capacity" by its "specific mass" in a sample (Bird, 2002; Page, et al., 1974). As shown in Table 2.2, the thermophysical properties of five different carbon fibers, one Kevlar, and one glass fiber have been obtained from the producers and compared numerically and two-dimensional (2D) with respect to each other. Between these FRPMC materials, it has been seen that carbon fibers have the highest thermal conductivity ability and Kevlar has the highest specific heat capacity. For this reason, obtaining the most HTP needs to have higher thermal conductivity and lower specific heat capacity properties (Yunus, et al., 1998). HTPs of different layer thicknesses and compositions were compared with Lee et al.s' conventional PV module type. Thermal conductivity, layer thicknesses, and composition of the conventional PV module could be found in Table 2.3.

Table 2.2 Thermophysical properties of FRPMC materials.

Dispersed Material	**Carbon Fiber**				
Producer	TORAY				
Product Name	M35J	M40J	M46J	M55J	M60J
Thermal Conductivity (W/mK)	162.8	279.9	349.8	651.0	629.7
Specific Heat Capacity (J/kgK)	723		719	732	
Dispersed Material	**Aramid**		**Glass Fiber**		
Producer	DuPont		Owens Corning		
Product Name	K29 – K49		E-Glass		
Thermal Conductivity (W/mK)	0.04		1.3		
Specific Heat Capacity (J/kgK)	1420		810		

Table 2.3 Properties of the conventional PV module (Lee, et al., 2008).

#	Material	Thickness (mm)	Thermal Conductivity (W/mK)
1	Glass	3.0	0.98
2	EVA	0.5	0.23
3	ARC	0.0001	1.38
4	PV Cell	0.25 – 0.4	148.0
5	Tedlar	0.1	0.36

With respect to Table 2.3, the conventional PV module consists of glass, ethylene vinyl acetate (ETA), anti-reflective coating (ARC), PV cell, and Tedlar, orderly. The thickest component of this conventional PV module was the glass (3 mm) and the thinnest two components were ARC (0.0001 mm) and PV cell (0.25-0.4 mm). The layer and physical parameters of this study have been presented in Table 2.4. With respect to defined parameters, each FRPMC material has been investigated separately between 1 mm and 10 mm layer thicknesses. However, the combination of each FRPMC material has been investigated between 1 mm and 4 mm layer thicknesses in order to define the appropriate FRPMC material and obtain the optimum HTP on the lamination of PV modules.

Table 2.4 Parameters and physical properties.

Parameter	**Symbol**	**Values**	**Unit**
The combination of the glass fiber and carbon fiber. Each FRPMC material layer thicknesses variate between 1 and 4 mm.	P_a	$1 \leq t \leq 4$	mm
The combination of the glass fiber and Kevlar. Each FRPMC material layer thicknesses variate between 1 and 4 mm.	P_b	$1 \leq t \leq 4$	mm
The combination of the carbon fiber and Kevlar. Each FRPMC material layer thicknesses variate between 1 and 4 mm.	P_c	$1 \leq t \leq 4$	mm
Only glass fiber and layer thicknesses variate between 1 and 10 mm.	P_d	$1 \leq t \leq 10$	mm
Only carbon fiber and layer thicknesses variate between 1 and 10 mm.	P_e	$1 \leq t \leq 10$	mm
Only Kevlar and layer thicknesses variate between 1 and 10 mm.	P_f	$1 \leq t \leq 10$	mm

Representative boundary conditions (BCs) and thermal resistance circuit have been shown in Figure 2.10. Outer edges of the combined FRPMC material have been

assumed as adiabatic on the 2D NUM model. Temperatures of the top (T_1) and bottom (T_2) edges of the 2D NUM model have been defined as 70 °C and 50 °C.

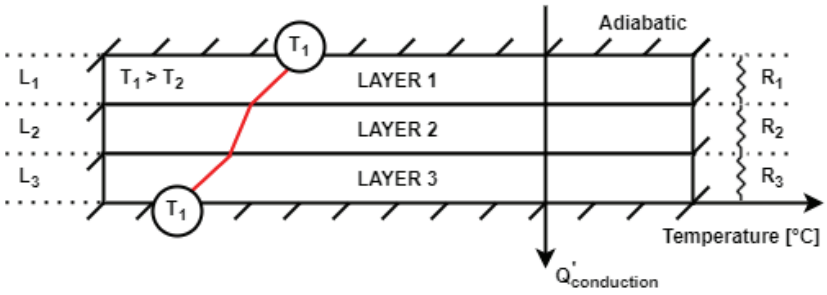

Figure 2.10 Thermal resistance circuit and BCs.

Considering a layer with a thickness of L and an average heat transmission coefficient k and two surfaces held at T_1 and T_2 temperatures, the Fourier heat conduction law

$$\dot{Q}_{conduction} = -kA\left(\frac{dT}{dx}\right) \tag{2.2}$$

Considering the composite structure consisting of three different layers seen in Figure 2.10, the continuous heat transfer rate in this structure defined as

$$\dot{Q} = (T_1 - T_2)/R_{total} \tag{2.3}$$

where R_{total} is the total thermal resistance and is defined as

$$R_{total} = R_{layer,1} + R_{layer,2} + R_{layer,3} = \frac{L_1}{k_1 A} + \frac{L_2}{k_2 A} + \frac{L_3}{k_3 A} \tag{2.4}$$

$$R_{layer} = \frac{L}{kA} \tag{2.5}$$

ANSYS Fluent package was used to solve the equations used in modeling and to obtain NUM results. The computer hardware on which the solution is implemented includes an Intel Core i7-8565U processor and 32 GB of memory. The equations used in the modeling are time-independent, based on the SIMPLE discrete solver algorithm

with the second-order upwind scheme, and the solution is carried out under the convergence criterion of 1.10^{-5}. Before the solution of the parameters specified in this problem, a grid independence study was carried out under different cell numbers of the composite structure with glass and carbon fiber. Within the scope of this study, the average heat flux values in different grid structures were compared and it was seen that the relevant NUM model results did not change after 60.000 cell numbers.

The heat flux value of each FRPMC structure has been investigated under indicated BCs and can be seen in Figure 2.11. It has been seen that the best HTP has been obtained from carbon fibers followed by e-glass and Kevlar. In this case, the best carbon fiber was the M55J and its heat flux values vary between 6.51 W/mm^2 and 0.651 W/mm^2 in the direction of thicknesses varying between 1 and 10 mm. Heat flux values have been obtained between 0.013 and 0.0013 W/mm^2 for the e-glass. Kevlar was the lowest FRPMC material with respect to the average heat flux values and was obtained between 4.10^{-4} and 4.10^{-5} W/mm^2.

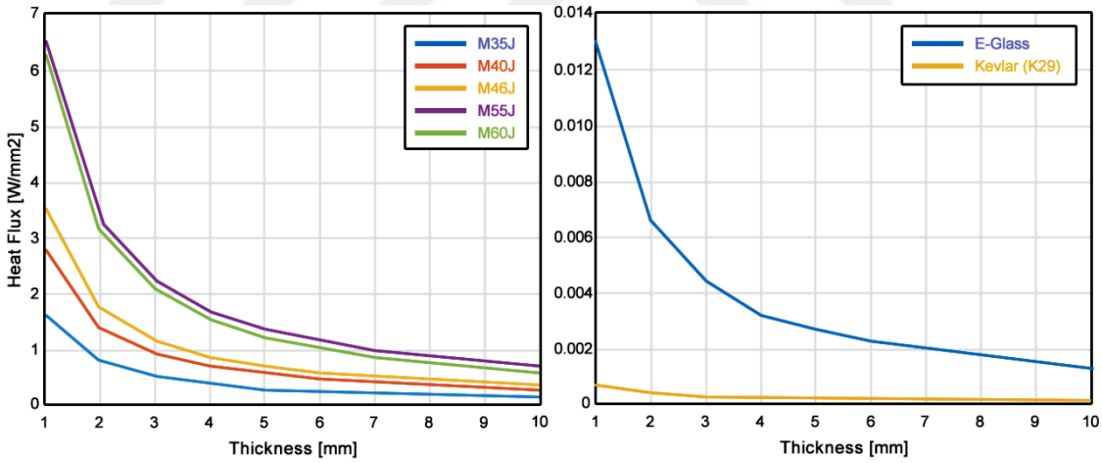

Figure 2.11 Heat flux values of each FRPMC material.

Carbon fiber is an electrically conductive material and the lamination of PV cells require electrically insulated materials at least for the first layer which contact with the PV cell. For this reason, FRPMC materials which are indicated in this study should be used as combined such as carbon fiber + glass fiber or carbon fiber + Kevlar. Under these limitations, combined FRPMC materials have also been investigated numerically

to observe HTP abilities as shown in Figure 2.12. Results showed that the average heat flux values of a composite structure that includes carbon and glass fibers are between 0.029 and 0.0032 W/mm^2. Average heat flux values of glass fiber with Kevlar have been obtained between 0.00039 and 0.0001 W/mm^2. Lastly, 0.00039 and 0.0001 W/mm^2 heat flux values have been obtained from a composite structure that includes carbon fiber and Kevlar.

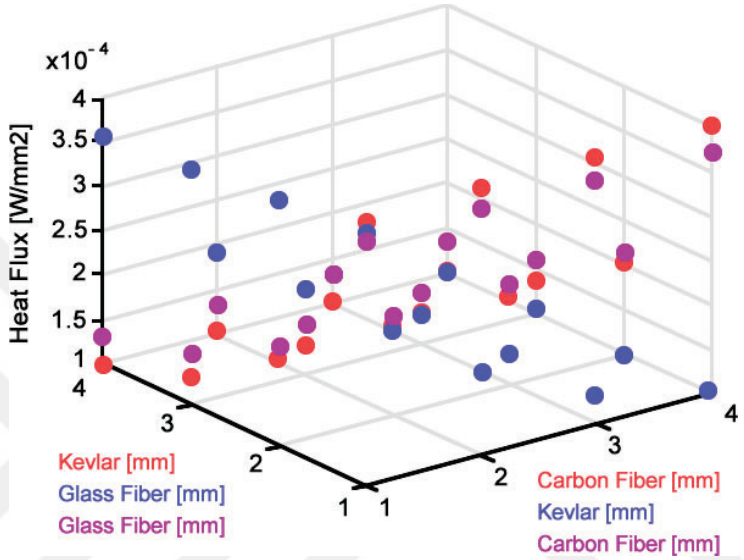

Figure 2.12 Heat flux values of the combinations of FRPMC materials under different thicknesses.

After these preliminary studies, a new composite structure that includes a PV cell, carbon fiber, and glass fiber has been compared with the conventional laminated PV module based on average heat flux values, numerically. The composition of these two laminated PV modules has shown in Figure 2.13. After implementing NUM studies, the average heat flux value of the conventional PV module has been observed as 0.0013 W/mm^2. Contrarily, the average heat flux value of the PV module laminated by FRPMC materials (Figure 2.13.b) has been found 0.0255 W/mm^2. The results support the heat flux values obtained in two different PV modules, and it has been concluded that the heat energy stored in the PV module laminated with FRPMC materials with an average heat flux value of 0.0242 W/mm^2 is transferred faster than the conventional PV module type.

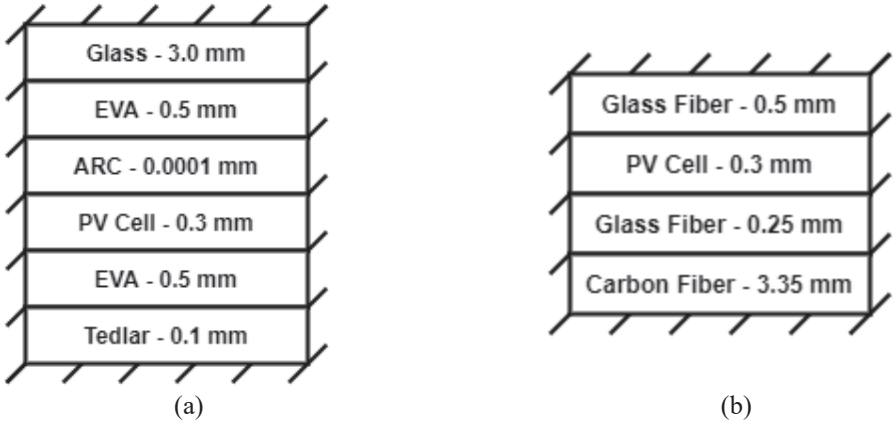

Figure 2.13 Components and their thicknesses of the conventional (a) and PV module laminated with FRPMC materials (b).

Thus, this chapter approved that the FRPMC material usage on the lamination of PV modules provides better HTP than conventional PV module types (Korkut and Gören, 2022).

2.4 Vacuum Assisted Resin Transfer Molding (VARTM) Method

VARTM is a subset of the methods of composite manufacturing. FRPMC materials fixed on the mold are vacuumed by a bag. During the vacuum, resin flow occurs and homogeneous penetration of the matrix material into the FRPMC materials is ensured. The product is cured at room temperature or a defined temperature range within the time interval specified by the producer of the matrix material, after the impregnation (Srivatsan, 1995; Matthews and Rawlings, 1999). The VARTM process can be summarized following main steps:

- On the mold surface, materials like peel plies and release films are placed out. A chosen dispersed substance is then applied to the release film following this process.
- Infusion spiral tubings are placed on the beginning and end edges of the mold to obtain a vacuum.
- Materials that have been placed on the mold are sealed with vacuum bags, and the air is drawn out of the bag by a vacuum pump.
- Prepared matrix material across the technical specifications in the external reservoir is drawn into the mold by the vacuum. When the matrix material is infused with the dispersed material and complete impregnation, the vacuum is stopped.

- Following the impregnation, the product is finished with curing and de-molding procedures.

Representative components of the VARTM process in this study are illustrated in Figure 2.14. The function of each component used in the VARTM process can be summarized as follows:

- To create a completely closed volume, vacuum bagging material is taped to the borders of the mold.
- Normally, release films are positioned just next to the laminate. They separate the distribution medium from the laminate. To ensure that any trapped air or volatiles, which could degrade the laminate's quality, are eliminated, release films are frequently perforated.
- The laminate's surface is contacted by release textiles and peel plies. These are woven goods that are sturdy and effectively withstand heat. Peel plies and release textiles leave a weave pattern imprint, whereas release films and release fabrics give the cured laminate a gloss finish. Peel plies give a surface that is clean and contaminant-free for future bonding or painting.
- To quickly release the product from tools and achieve a smooth surface finish, tool-release materials are employed. Teflon films that are self-adhered or liquid release agents are both used for this purpose. Teflon films can occasionally help with tool porosity issues as well.
- The resin is swiftly dispersed along the lateral extent of the component by a highly porous coating known as "resin distribution medium" that is put on top of the preform.
- Non-woven textiles used as bleeder/breather fabrics allow air and volatiles to be drawn out of the vacuum bag as the cure cycle progresses. In some composite lay-ups, they also absorb extra resin.

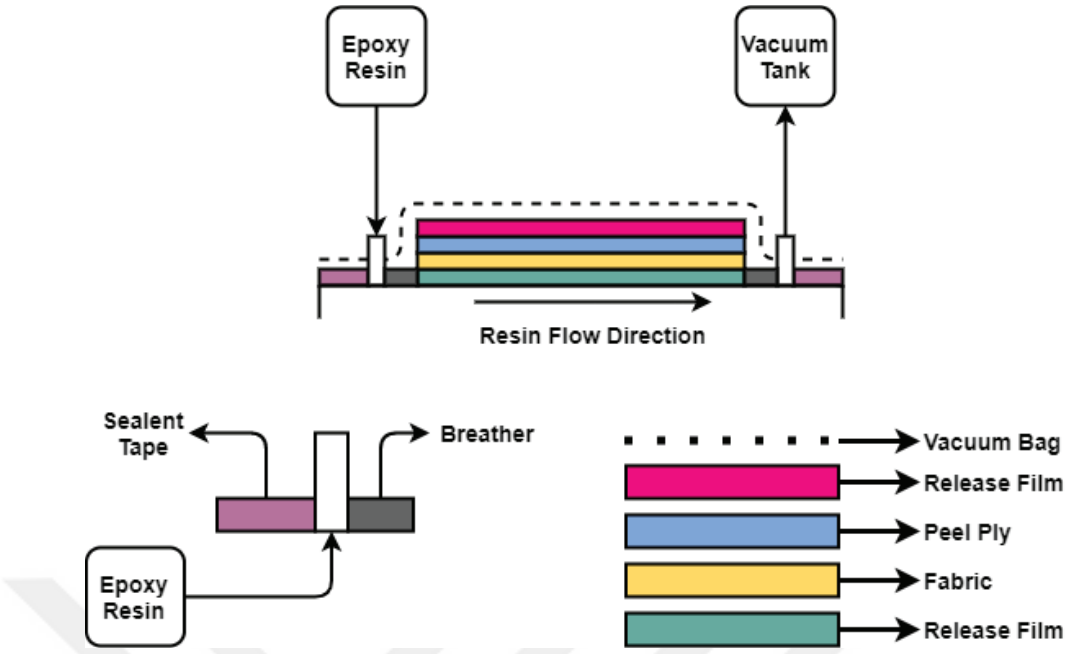

Figure 2.14 Schematic illustration of the VARTM process.

In the current study, for the lamination of the PV modules, seamless glass fiber was decided to use as dispersed materials. Two layers of seamless glass fiber were used below and a layer of seamless glass fiber was used above of the PV modules during the lamination process. The other component planned to use during the lamination of the PV modules is peel ply. Peel ply prevents the vacuum bag from sticking to the product. The other component is a vacuum bag which provides a coexistence of the components in the vacuumed area and allows the resin to penetrate homogeneously. An example production of solar car bodies with the VARTM method has shown in Figure 2.15. Figure 2.15.a refers to the mold preparation before the VARTM, Figure 2.15.b refers to the core materials placement in the planned product, Figure 2.15.c refers to the resin transfer under vacuum, and Figure 2.15.d-e refer to the after-production with the VARTM method.


(a) Preparation of molds (upper and lower body molds)

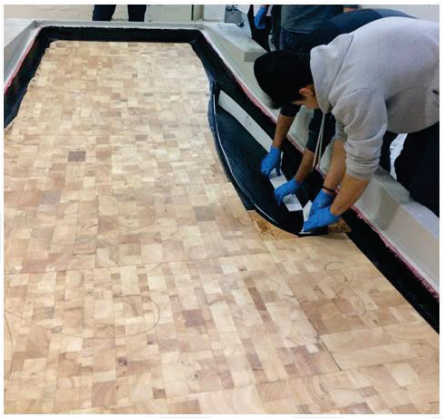

(b) Placement of core materials

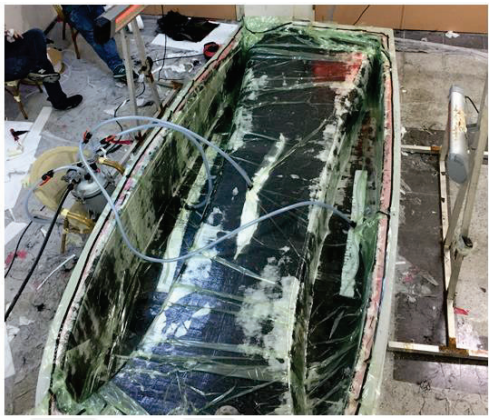

(c) Resin transfer under vacuum


(d) Produced bodies after VARTM


(e) Assembly of bodies and chassis.

Figure 2.15 An example production of Solaris 10 solar-racing car with VARTM method.

2.5 Lamination of Photovoltaic Cells

2.5.1 Preparation of the Photovoltaic Modules

The preparation of PV and PV/T modules starts with the preparation of the electrical connections between each PV cell followed by the lamination process with the use of FRPMC materials. For the present study, the m-Si type TW-158.75M-217 PV cells have been used, and the representative physical dimensions and electrical connection poles of the PV cells used in the current study have been shown in Figure 2.16, Figure 2.17, and Figure 2.18. Accordingly, the dimensions of the PV cells used are 157.15 mm in width and 158.75 mm in length. Additionally, each PV cell has 5 pole lines.

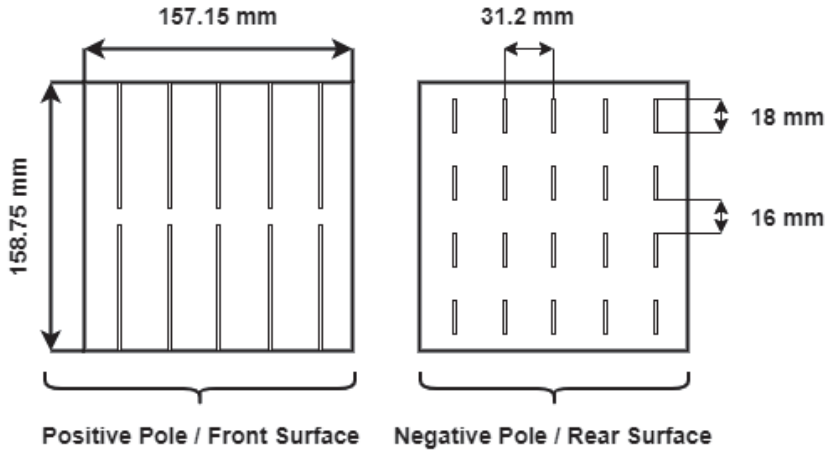

Figure 2.16 Physical dimensions of the PV cell (TW-158.75M-217).

Each PV cell has positive (+) and negative (-) poles and their solder qualities with each other have great attention during the preparation of electrical connections of PV modules. Each PV cell's positive pole connects electrically with the next PV cell's negative pole. Within the scope of the study, two 65 W PV cell modules have been aimed to laminate for comparison with and without thermally development. After the investigation of the technical specification of PV cells, the use of 24 pcs PV cells has been suitable for PV and PV/T modules to obtain the targeted power. PV cells are a power source, therefore, it was planned to make a series of connections between each PV cell. As shown in Figure 2.17, each PV cell's positive pole has been soldered to the next PV cell's negative pole.

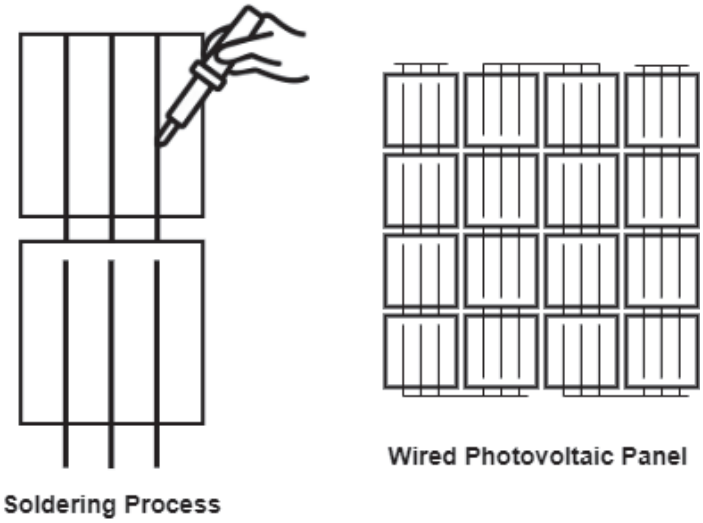

Figure 2.17 Soldering of the PV module.

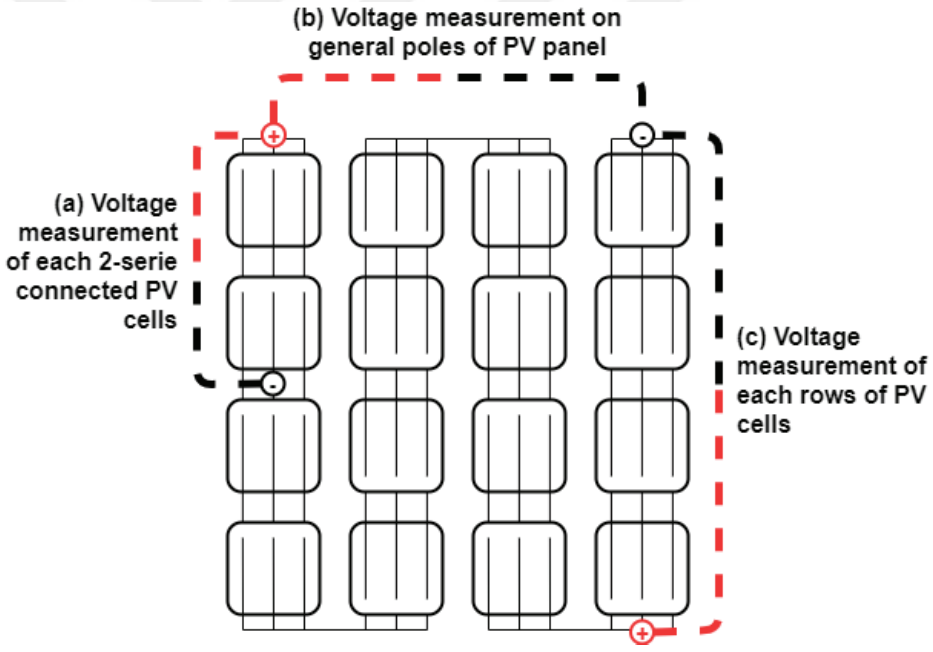

Figure 2.18 Voltage measurement control nodes of the PV module.

Besides the soldering of the poles of each PV cell, equipment, measurement instruments, and environmental conditions to be preferred during the soldering of PV cells have great importance. Before starting the electrical preparation of each PV module, the operator needs to make sure that the environment is very clean, because of the possibility of dust adhering to the PV cell surfaces. The thickness of the

unlaminated PV cell is 0.2 mm and in view of the fact that the thickness of PV cells, sudden temperature changes in the workshop should not be allowed. Also, the thermal conductivity value of the PV cell is high. For this reason, the unlaminated PV cells can be affected by the current environmental conditions changes immediately, and the PV cell can easily be physically damaged (e.t. micro-crack). After environmental necessaries, another important choice, the soldering machine must be able to reach an appropriate temperature which is indicated by the PV cell manufacturer, and the usage of a flux pen is another key point for the ability of the soldering of PV cells. For the soldering of PV cells, the use of a thin and electrically conductive wire such as tab wire is another important piece of equipment in order not to be damaged PV cells during the lamination phase (under vacuum pressure in a sealed space). The flux pen and tab wire used in the present study have been shown in Figure 2.19. Pictures from the isometric and top sides of the prepared PV module for the lamination phase have been shown in Figure 2.20. There are 24 cells in each PV module and each PV cell is connected in series with the next PV cell as indicated at the beginning of this subsection.

Figure 2.19 Flux pen and tab wire.

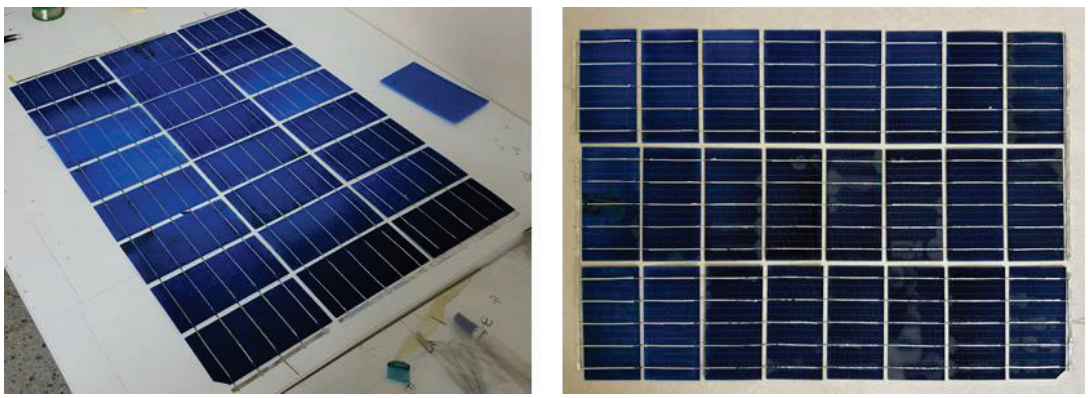

Figure 2.20 Electrically connected half-cut photovoltaic cells.

2.5.2 VARTM Process

This subsection explains the lamination of PV and PV/T modules using the VARTM method which has been explained basis in subsection 2.4. During the electrical preparation of PV and PV/T modules, defined PMC materials (matrix and dispersed) have been supplied, and the VARTM method has been adopted for the implementation of the lamination of each PV module. The order of the components and their product names for the lamination process has been shown in Figure 2.21. In this case, the first component is a mold-release film on the heated bed in the composition of the lamination process with the VARTM method. After the mold release film, there are fiber layers (seamless, e-glass fiber) followed by the PV cells. After the PV cells, there is the same dispersed material again, peel ply, and resin distribution medium, respectively. Peel ply provides simply removing any material from a sticky surface. For this reason, the use of the peel ply is highly recommended after the last layer of the dispersed material. The resin distribution medium looks like a honeycomb and provides a homogeneous penetration to the matrix material with the dispersed material under vacuum.

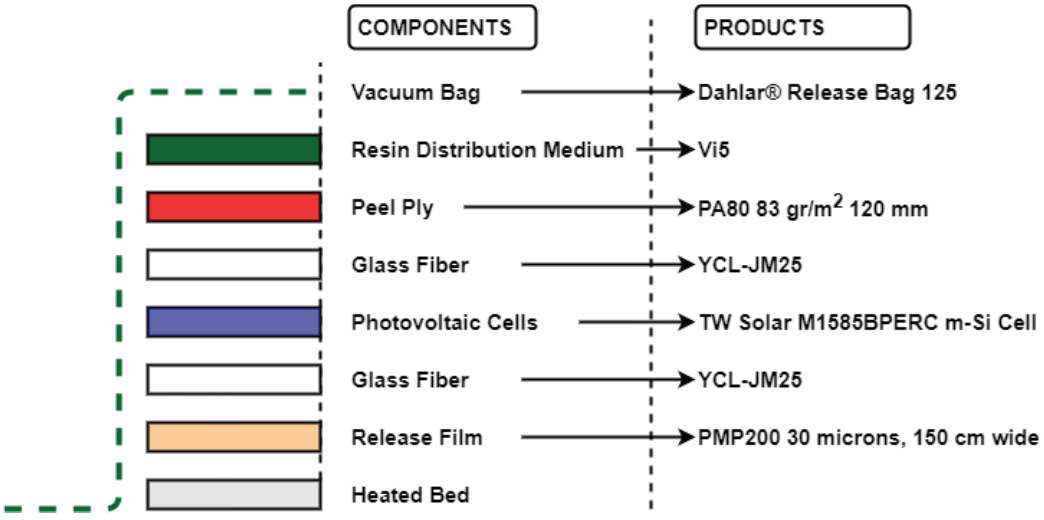

Figure 2.21 A schematic illustration of the component order during the lamination process the VARTM method.

Pictures of the preparation of the lamination process of the PV modules have been shown in Figure 2.22. In the sequence described above (Figure 2.21), the lamination process of the PV and PV/T modules has been implemented.

(a) (b) (c)

Figure 2.22 Preparation of the VARTM process. Release film on the heated bed (a), before the vacuum bag placement (b), and ready to vacuum (c).

Figure 2.23 shows the progress of the matrix material (epoxy resin) under vacuum in the lamination process. After the matrix material has reached the vacuum point, the vacuum has been stopped and the curing process has been started.

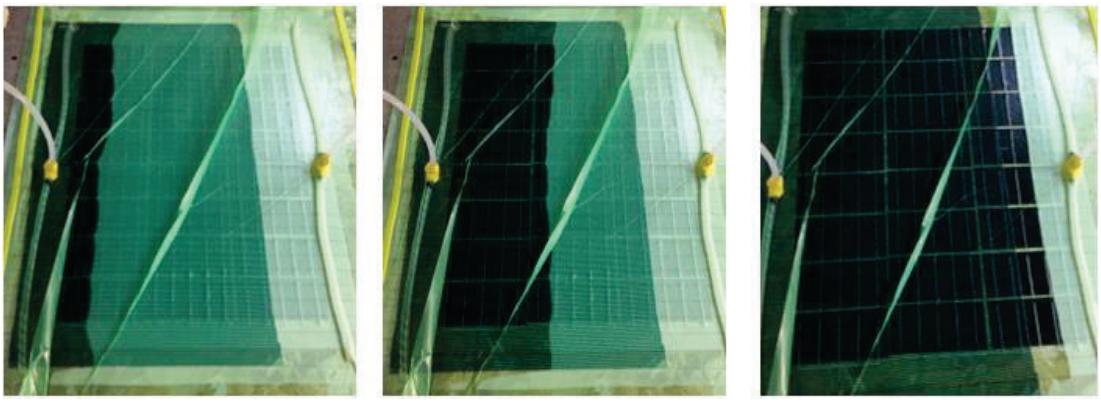

Figure 2.23 The progress of the epoxy resin homogeneously during the vacuum.

After the investigation of the technical specifications of the matrix material, curing at 100 °C for 2 hours under one step was deemed appropriate and implemented. Under

this condition, the transition temperature of the PV and PV/T modules reaches 80-85 °C and has been accepted as suitable for the usage conditions of the PV and PV/T modules. The used curing automation system implements heat under three different stages to the product and the schematic illustration of the interface of the curing automation system has been shown in Figure 2.24.

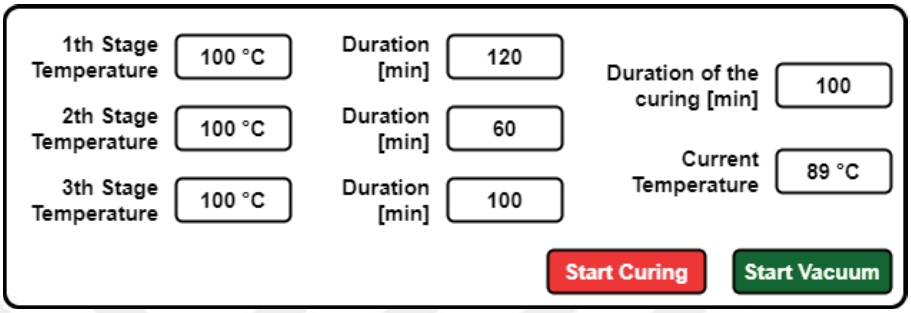

Figure 2.24 The interface of the curing automation system.

After the curing, laminated PV modules have been shown in Figure 2.25. For the use of both PV modules, a mechanical frame has been designed and manufactured for mounting the laminated PV modules in the test environment. Another feature of this frame is that PV modules can be adjusted according to the changing global tilting angle.

Figure 2.25 The laminated PV module and produced mechanical frame for the adjustment of the tilting angle.

With respect to the scope of the study, one of the laminated PV modules should be thermally developed. In the conventional type of PV/T modules, metals with high heat conductivity are used to increase the heat transfer capability between the cooling system and the PV module. Generally, these materials are copper and aluminum. For this study, a dispersed material, carbon fiber has been used to increase HTP between the PV module and the cooling channel. The VARTM method has been also implemented as the manufacturing method. A schematic illustration of the assembly formed by carbon fiber together with the cooling system and photovoltaic module as shown in Figure 2.26. In this context, manufacturing preparations have been shown in Figure 2.27.

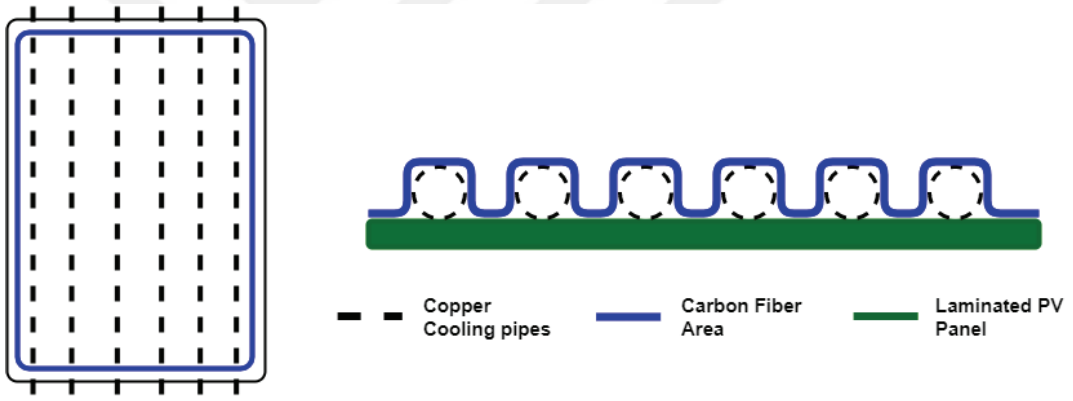

(a) Back view of the PV/T module. (b) Side view of the PV/T module.

Figure 2.26 Schematic illustration of the PV/T module from the two views: (a) back and (b) side view.

In order to obtain a maximum HTP, dispersed material is contacted the MAX area of the cooling system and also adhered to the PV modules. The preparation of the manufacturing of the laminated PV module, cooling system, and carbon fiber by the VARTM method have shown in Figure 2.27. The manufacturing method has taken reference with the same manufacturing method for the lamination of PV cells. The manufacturing of the cooling system based on the VARTM method and the produced PV/T module has been shown in Figure 2.28 and Figure 2.29.

Figure 2.27 Preparation of the cooling system components for VARTM-based production.

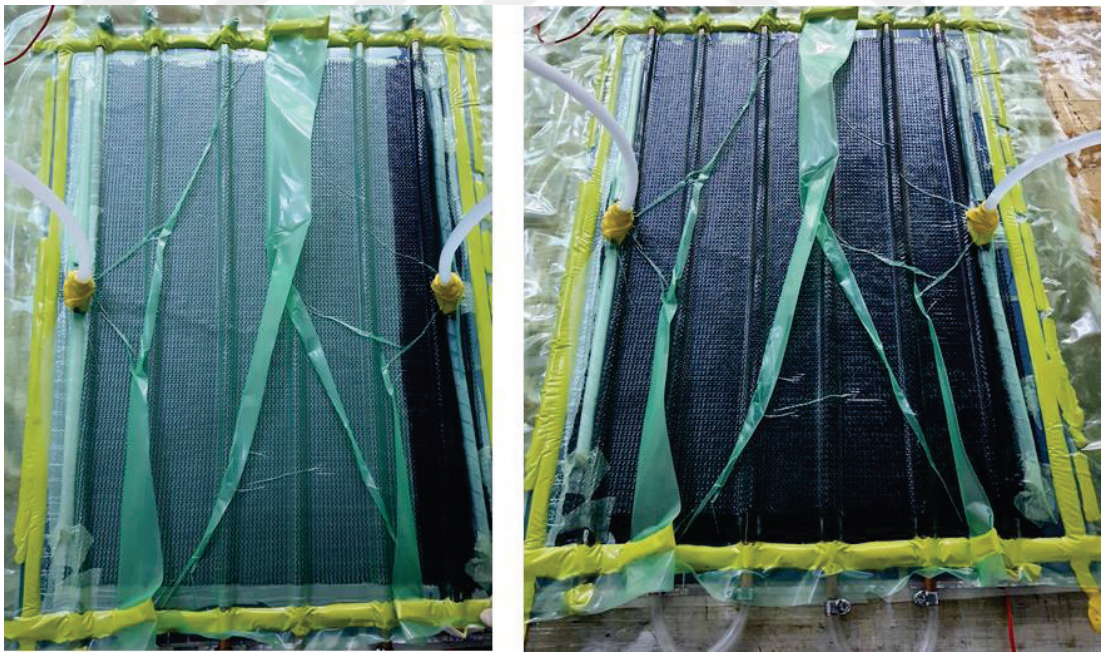

Figure 2.28 The progress of the epoxy resin homogeneously during the vacuum.

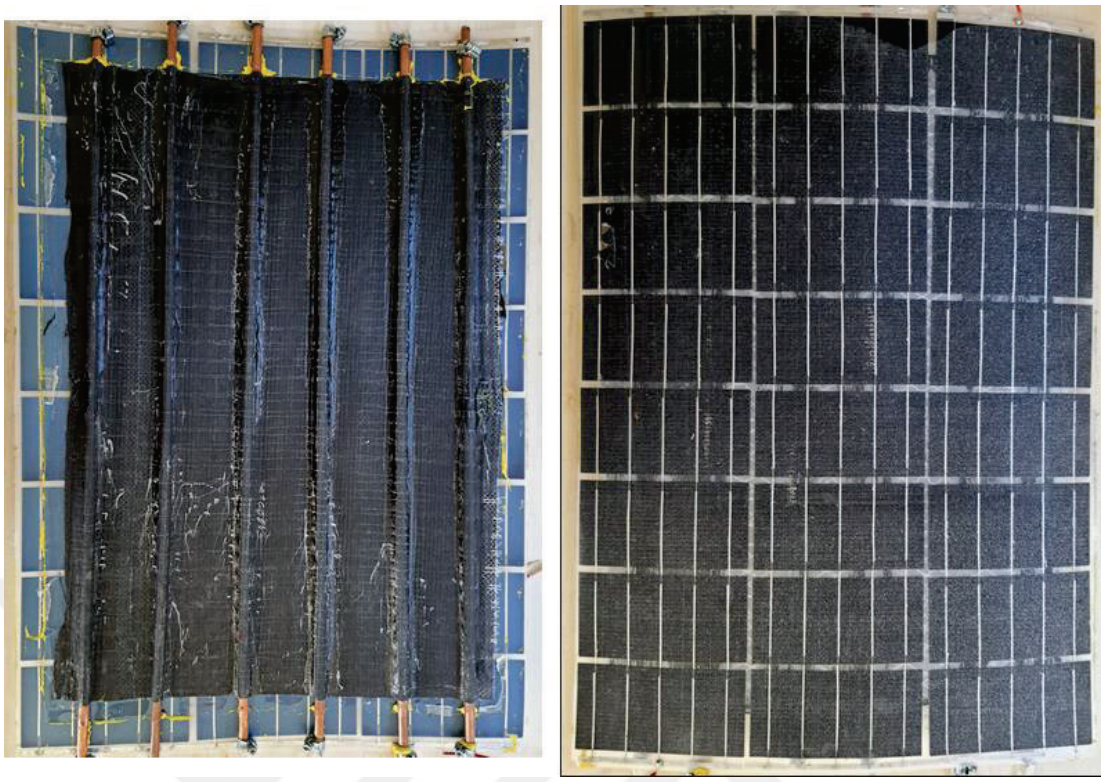

Figure 2.29 Produced thermally developed PV/T module.

2.6 Computational Fluid Dynamics (CFD) Method

2.6.1 Geometry and Grid Discretization

The computational fluid dynamics (CFD) studies start with the preparation of the geometries of PV and PV/T modules followed by the grid discretization. The computational dimensions of PV and PV/T modules have been shown in Figure 2.30 and Figure 2.31. Also, as mentioned in subsection 2.5, each PV and PV/T module is comprised of 3x8, 24 cells, and the total dimensions are 680 mm in length and 491.45 mm in width.

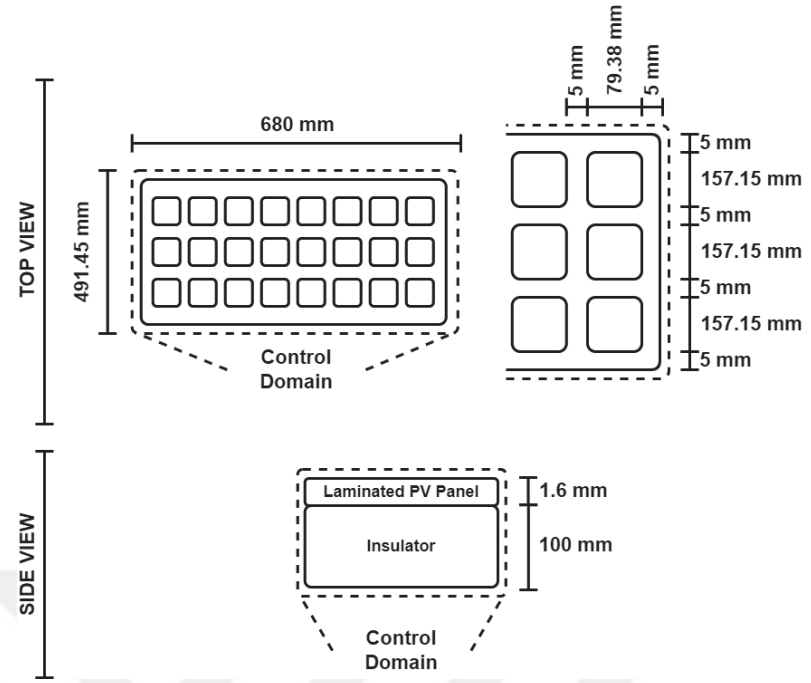

Figure 2.30 Computational dimensions of the PV module.

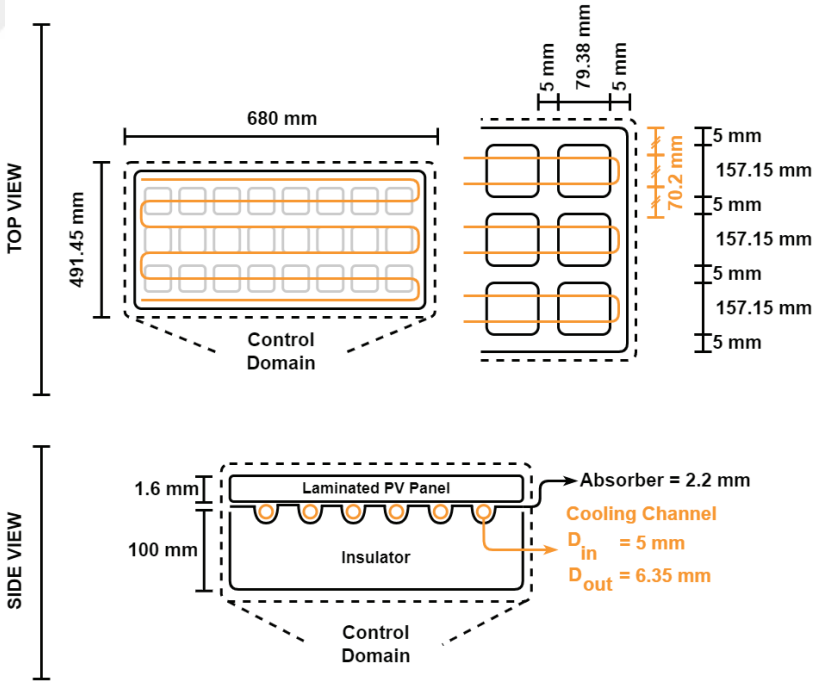

Figure 2.31 Computational dimensions of the PV/T module.

The PV module has consisted of the laminated PV module (1.6 mm) and the insulator (100 mm). Besides the PV module, the PV/T module has consisted of the laminated PV module (1.6 mm), absorber (2.2 mm), cooling channel (D_{in} = 5 mm, D_{out} = 6.5 mm), and insulator (100 mm). Thus, the total thicknesses of PV and PV/T modules are 101.6 mm and 103.8 mm. For the mesh independency study, PV and PV/T module computational geometries have been investigated under different grid sizes to reduce the deviation of results obtained from CFD studies. Contrary to the investigation of all-day conditions, a specific operational condition has been implemented simultaneously on PV and PV/T modules to define the appropriate grid size.

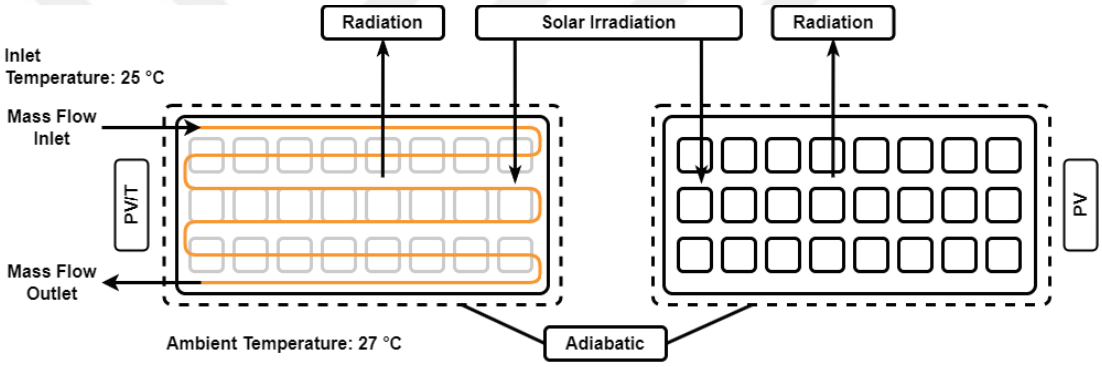

Figure 2.32 BCs of the grid independence study.

As indicated in Figure 2.32, SR and wind speed (WS) have been assumed as 800 W/m^2 and 0 km/h. Ambient and coolant temperatures have been defined as 27 °C and 25 °C. Also, the lateral and bottom surfaces of PV and PV/T modules have been assumed as adiabatic. End of each CFD study, the T_{avg} of PV and PV/T modules have been tracked and logged. Results have been shown in Figure 2.33.

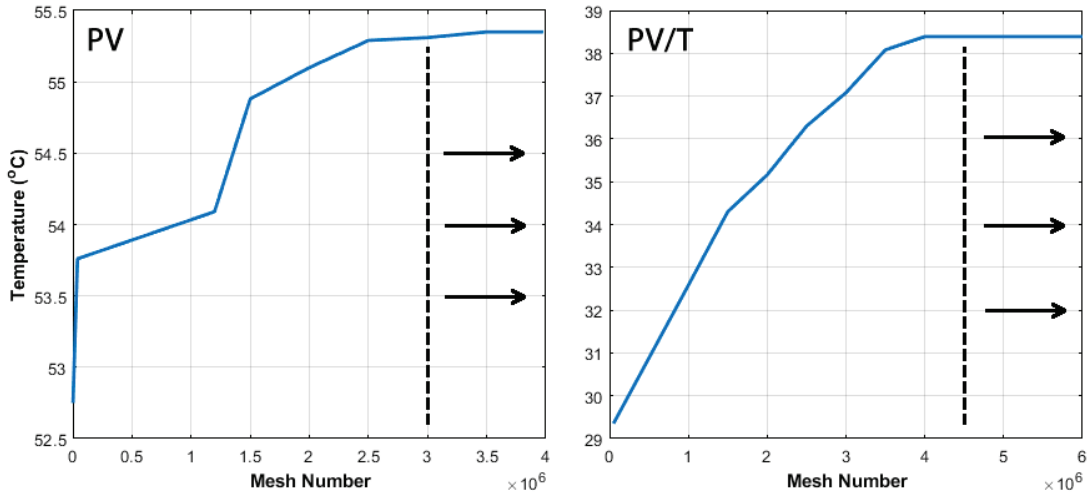

Figure 2.33 Average PV/T and PV module temperatures with respect to the increasing mesh number.

For the computational geometry of the PV module, the CFD model has been discretized from 1.500 to 3.900.000 cells. Results showed that the average temperature (T_{avg}) of the PV module surface has found as constant after 3.000.000 cells. For the PV/T module, the CFD model has been discretized from 50.000 to 6.000.000 cells. Results showed that the T_{avg} of the PV/T module surface has found as constant after 4.500.000 cells. In this way, mesh structures have 3.000.000 and 4.500.000 cells have been defined for the PV and PV/T modules.

2.6.2 Boundary Conditions

In computational fluid dynamics (CFD) simulations, PV and PV/T modules have been modeled as 3D and assumed as isolated except for sun-facing sides. In NUM simulations, it has been assumed as the heat transfer is only from the sun-facing side with convection and radiation. Schematic illustrations of the BCs of PV and PV/T modules have shown in Figure 2.34, and Figure 2.35. Besides, mass flow inlet and outlet BCs have been defined at the start and end of the water-type cooling channel.

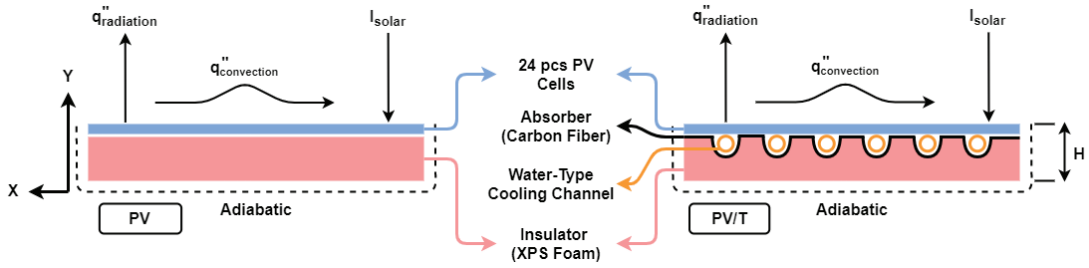

Figure 2.34 BCs of PV and PV/T modules (side-view).

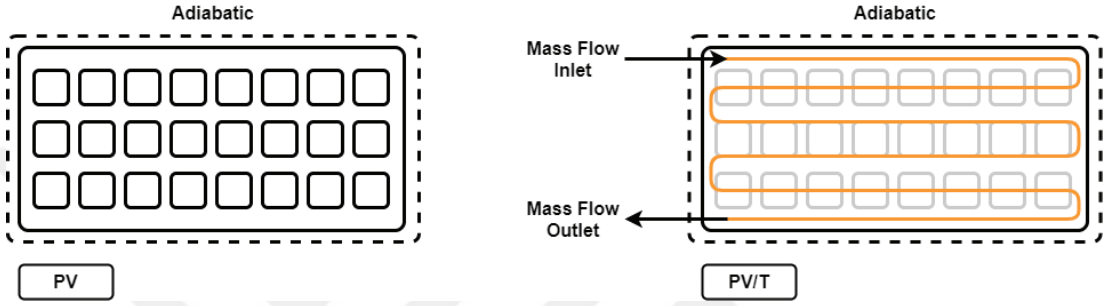

Figure 2.35 BCs of PV and PV/T modules (top-view).

The energy balance equation of these modules has shown in Equation 2.6.

$$-k\frac{dT}{dy}\bigg|_{y=H} = I_{solar}\alpha_{gls} - q''_{conv} - q''_{rad} \tag{2.6}$$

where I_{solar} is the solar radiation, α_{gls} is the absorptivity constant, q''_{conv} and q''_{rad} are the heat losses through convective and radiative. The Stefan-Boltzmann rule is used to calculate the radiative heat losses from the sun-facing sides of PV and PV/T modules, and it can be expressed as

$$q''_{rad} = \epsilon\sigma\left(T^4_{surf} - T^4_{sky}\right) \tag{2.7}$$

where ϵ is the emissivity constant, σ is the Stefan-Boltzmann constant, T_{surf} and T_{sky} are represent the temperature of the laminated PV module and sky temperature. The Swinbank equation is used to calculate the sky's temperature as

$$T_{sky} = 0.037536T^4_{amb} + 0.32T_{amb} \tag{2.8}$$

where T_{amb} is the ambient temperature and convective heat losses can be

$$q''_{conv} = h_{total}\left(T_{surf} - T_{amb}\right) \tag{2.9}$$

where h_{total} is the heat transfer coefficient from the laminated PV modules. Eq. 2.10 provides the heat transfer coefficient.

$$h_{total} = \left(h^3_{natural} - h^3_{forced}\right)^{1/3} \tag{2.10}$$

where Equations 2.11 and 2.12 express natural and forced convections, respectively, as $h_{natural}$ and h_{forced}.

$$h_{natural} = 1.78\left(T_{surf} + T_{amb}\right)^{1/3} \tag{2.11}$$

$$h_{forced} = 2.8 + 3.0V_{wind} \tag{2.12}$$

where V_{wind} represents the WS in m/s. Thermophysical properties of material used in CFD simulations have shown in Table 2.5.

Table 2.5 Thermophysical properties of materials used in PV and PV/T modules.

#	Material	c_p (J/kgK)	ρ (kg/m^3)	k (W/mK)
1	PV Cell (Si)	677	2330	148.0
2	Carbon Fiber	719	-	349.8
3	Glass Fiber	810	-	1.3
4	XPS Foam	1500	45	0.035

2.6.3 Solution Method

The Navier-Stokes equations, which are based on the conservation of mass, momentum, and energy, control the behavior of the CFD model. Additionally, all outside PV and PV/T module surfaces other than the sun-facing side are considered to be thermally isolated, and thermophysical characteristics of materials are assumed to be constant. In order to calculate large flow rates, the realizable k-ε turbulence model

is employed, and the SIMPLE scheme is recommended in order to establish pressure-velocity coupling.

For continuity:

$$\frac{\partial}{\partial x}(u) + \frac{\partial}{\partial y}(v) + \frac{\partial}{\partial z}(w) = 0 \tag{2.13}$$

For x-momentum:

$$\frac{\partial}{\partial x}(uu) + \frac{\partial}{\partial y}(vu) + \frac{\partial}{\partial z}(wu) = -\frac{dp}{\rho dx} + \frac{(\mu + \mu_t)}{\rho}\left[\frac{\partial^2 u}{\partial x^2} + \frac{\partial^2 u}{\partial y^2} + \frac{\partial^2 u}{\partial z^2}\right] \tag{2.14}$$

Newton's second law, which yields the concept of momentum conservation, describes how a body moves when subjected to variable forces. Equation 2.14 illustrates the conservation of momentum along the x-axis, and the ANSYS Fluent Theory Guide has the conservation of momentum equations along the y and z-axes (Manual, 2009).

For energy:

$$\frac{\partial}{\partial x}\left(\rho \mu_j c T\right) = \frac{\partial}{\partial x_j}\left[k \frac{\partial T}{\partial x_j}\right] - \frac{\partial}{\partial x_j}\left[\left(\frac{c\mu_t}{\sigma_k}\right)\frac{\partial T}{\partial x_j}\right] \tag{2.15}$$

The turbulent viscosity, denoted by the symbol μ_t, is where

$$\mu_t = \rho c_\mu \frac{k^2}{\varepsilon} \tag{2.16}$$

The fluid flow and circulation inside the serpentine cooling pipe were simulated using the realizable k-ε turbulence model (Khelifa, et al., 2015). The SIMPLE algorithm with the second-order upwind scheme was also chosen as the pressure-velocity coupling method (Patankar, 2018). The theory guide of the software program includes mathematical formulae for the selected turbulence model (Manual, 2009). All of the walls had a no-slip condition defined on them. The PV cell domain's energy equation is as follows:

$$\frac{\partial}{\partial x}\left(k\frac{\partial T}{\partial x}\right)+\frac{\partial}{\partial y}\left(k\frac{\partial T}{\partial y}\right)+\frac{\partial}{\partial z}\left(k\frac{\partial T}{\partial z}\right)-P'''_{out}+Q'''_{gen}=0 \tag{2.17}$$

where P'''_{out} and Q'''_{gen} are source terms that exemplify the electrical power output and heat generation (Armstrong and Hurley, 2010). The source terms in Equation 2.17 are expressed as

$$P'''_{out}=\eta_e\left(\alpha_{PV}\tau_{gls}I_{solar}\right)/t_{PV} \tag{2.18}$$

where t_{PV} stands for the PV cell's thickness.

$$Q'''_{gen}=(1-\eta_e)\left(\alpha_{PV}\tau_{gls}I_{solar}\right)/t_{PV} \tag{2.19}$$

where α_{PV} and τ_{gls} stand for the PV cell's absorptivity and the lamination layer's transmissivity, respectively. Transmissivity and absorption values were taken to be 0.9 and 0.95, respectively (Joshi and Dhoble, 2018).

$$\eta_e=\eta_{ref}\left[1-\beta_{PV}\left(T_{PV}-T_{ref}\right)\right] \tag{2.20}$$

where η_e denotes the PV cell's electrical efficiency. In this investigation, the temperature coefficient (β_{PV}) of the m-Si type PV cell was taken as 0.00392 and the reference temperature (T_{ref}) was set to 298 K. The values of η_{ref} of the m-Si type PV cell was set to 21.8%. For the mass and momentum equations, the convergence is dependent on certain levels of precision, which were set at 10^{-4}, and for the energy equation, at 10^{-6}. The η_e, η_{th}, and η_{total} were computed for this investigation. Equation 2.20 was used to assess the PV and PV/T modules' electrical efficiency. Thermal efficiency was also described as

$$\eta_{th}=\dot{Q}\Big/I_{solar}A_s \tag{2.21}$$

Equation 2.21 illustrates the thermal efficiency of the water-type PV/T system. A_s and $\dot{Q}$ represent the PV module area and thermal power.

$$\dot{Q} = \dot{m}c(T_{out} - T_{in}) \tag{2.22}$$

where T_{in} and T_{out} represent water inlet and outlet temperatures, and $\dot{m}$ represents the mass flow rate of the cooling channel. The PV/T module's total efficiency is stated as

$$\eta_{total} = \eta_e + \eta_{th} \tag{2.23}$$

where η_e and η_{th} represent the electrical and thermal efficiencies.

CHAPTER THREE
DATA ANALYSIS AND RESULTS

3.1 Experimental Environment

Within the scope of this study, an experimental (EXP) environment has been established at Dokuz Eylul University (DEU), Tınaztepe Campus, Engineering Department Zone. As shown in Figure 3.1, a workshop has been employed to serve EXP studies. This workshop has two rooms and one of these rooms belongs to electric vehicle (EV) charging. The other room named as test and monitoring room, includes measurement system monitors, a water tank, and a water pump for the photovoltaic/thermal (PV/T) module. On the roof of this workshop, there are photovoltaic (PV) modules laminated within this study and conventional types of PV modules. Besides the PV modules, the sensors of the weather station are also allocated on the roof.

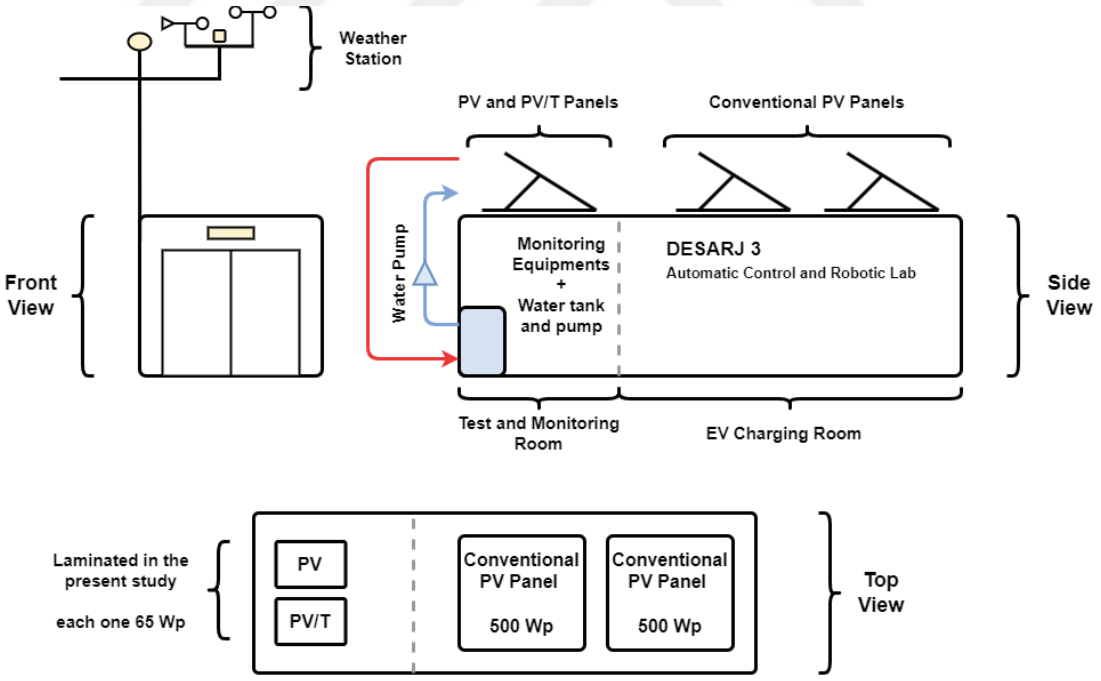

Figure 3.1 From different views, the schematic illustration of the EXP environment.

During the experiment, weather station logs are transmitted wirelessly to the test and monitoring room, and the generated electrical energy logs of the PV and PV/T

modules are transferred to the test and monitoring room by cable. As shown in Figure 3.1, water is pumped from the test and monitoring room to the PV/T module on the workshop's roof. After the heat transfer between the water and the PV/T module, the hot water turns back to the water tank. Pictures of the EXP environment and the PV/T and PV modules located on the roof are given in Figure 3.2, and Figure 3.3.

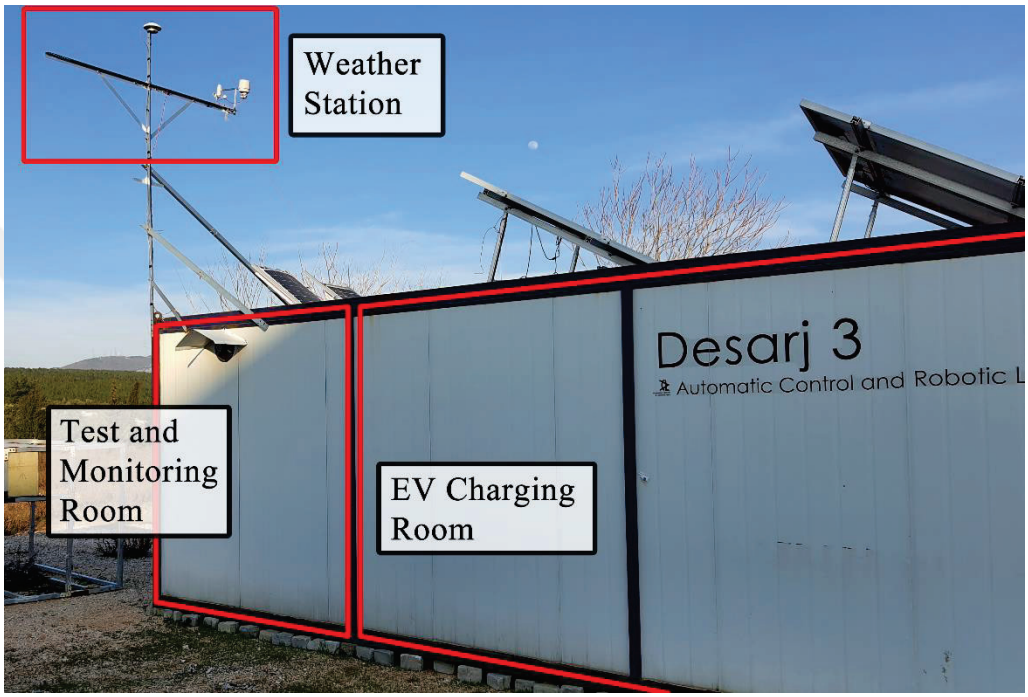

Figure 3.2 The experimental environment and the testing area of PV and PV/T modules.

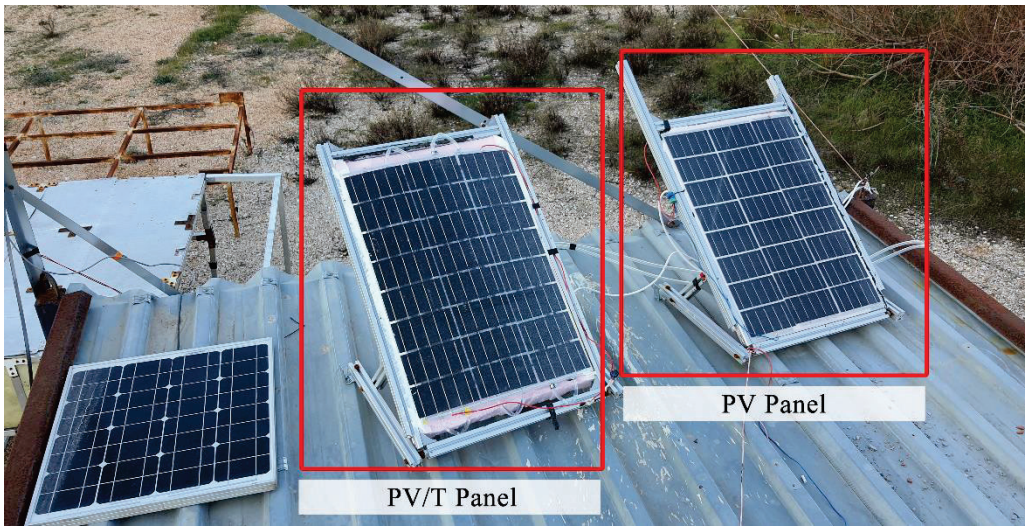

Figure 3.3 Laminated PV and PV/T modules that emplaced on the roof of the workshop.

Thus, the EXP environment provides the measurement of the ambient temperature (AT), wind speed (WS), solar radiation (SR), and generated electrical energy values of the PV and PV/T modules. Also, the water T_{in} and T_{out} of the PV/T module are measured, simultaneously.

3.1.1 Weather Station

One of the data packages we need to know in order to the validation of the computational fluid dynamics (CFD) model is weather conditions. The weather data package contains AT, WS, and SR. The components of the weather station have been indicated in Figure 3.4. The transmitter of the weather station (a) measures and sends the weather conditions to the receiver (b) every 48 seconds via RF signals.

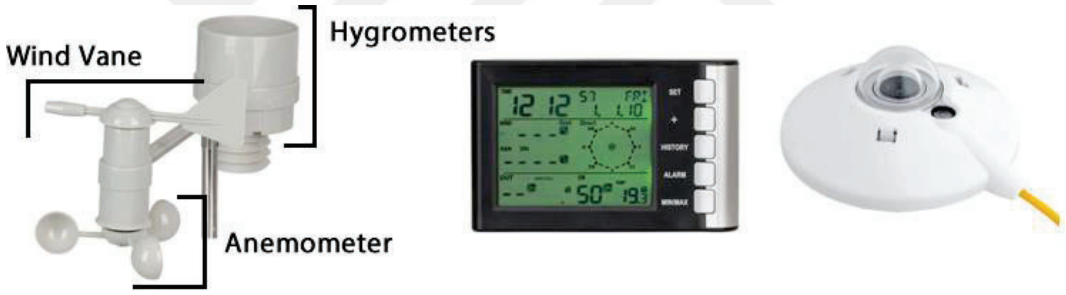

(a) (b) (c)

Figure 3.4 Components of the weather station. (a) Transmitter, (b) receiver, and (c) pyranometer.

The measurement ranges and accuracy/sensitivity values of the weather station components have been indicated in Table 3.1. The pyranometer (Figure 3.4.c) measures a maximum (MAX) of 2000 W/m^2 and has a 7 µV/W/m^2 sensitivity rate. The anemometer measures the WS between 0 and 180 km/h and has a +/- 3.6 m/s accuracy rate. Also, the wind vane measures between 0° and 360°. The hygrometer measures the humidity between 1% and 99% with 5% accuracy. Besides the humidity, AT is measured between -40 °C and 60 °C with an accuracy of 1 °C.

Table 3.1 Technical specifications of the weather station and accuracy/sensitivity values.

Equipment	**Brand**	**Range**	**Accuracy/Sensitivity**	
Pyranometer	MS-410	Max. Irr. 2000 W/m^2	7 μV/W/m^2	Sens.
Anemometer	Digitech XC-0400	0 – 180 km/h	+/- 3.6 m/s	Acc.
Wind Vane		0° - 360°	-	-
Hygrometer		1% - 99%	+/- 5%	Acc.
Temperature		-40 °C - 60 °C	+/- 1 °C	Acc.

The presented weather station (Digitech XC-0400) cannot log the real-time measured weather conditions, it just presents the real-time data on its receiver screen (Figure 3.4.b). For this reason, an electronic device that can receive weather data packages from the weather station transmitter and log into the SD card simultaneously has been designed and produced as shown in Figure 3.5. Also, the wiring diagram and its source code have been shown in Appendices 3 and 4.

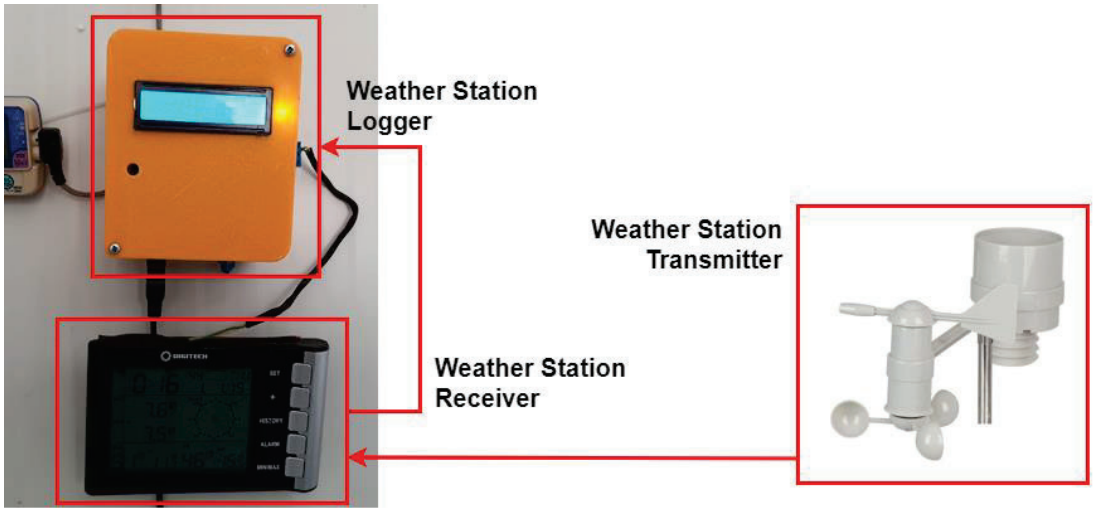

Figure 3.5 Weather station receiver and logger.

ATmega2560 has been used as a microcontroller in this device and operates at 5 voltages. Besides, DS1302 RTC and SD card modules have been employed for the instant time and taking logs. The relevant component operates at the frequency at

which the receiver and transmitter components of the weather station communicate and receives and records the relevant data at the same time. Technical specs of the weather station logger have shown in Table 3.2.

Table 3.2 Technical specs of the weather station logger.

Microcontroller	ATmega2560
OV	5 V
IV	7 – 12 V
Digital I/O Pins	54
Analog Input Pins	16
CS	16 MHz

3.1.2 MPPT and Generated Energy Meter (GEM)

Another data package we need to know in order to validate the CFD model is the generated electrical energy values of PV and PV/T modules. A maximum power point tracker (MPPT) has been employed to catch the MAX power efficiency of PV and PV/T modules. Besides, MPPT reduces the DC voltage output from the solar modules to a lower DC voltage value to charge the batteries. By tracing the path of the sun across the sky for the most sunlight, MPPTs maximize output. These normally offer you a rise of up to 35% in the summer and 15% in the winter. For MPPT controllers, this is exactly the reverse of the seasonal fluctuation. In the winter, modules produce more power since the temperatures are lower. Due to fewer days, winter is often when you need your solar modules to produce the most electricity. Therefore, MPPT plays an important role in this field. In this study, MPPTs designed and produced in partnership with Destek Automation and Solaris Solar Cars Team were used (Figure 3.6). The technical specifications of the related product are given in Table 3.3.

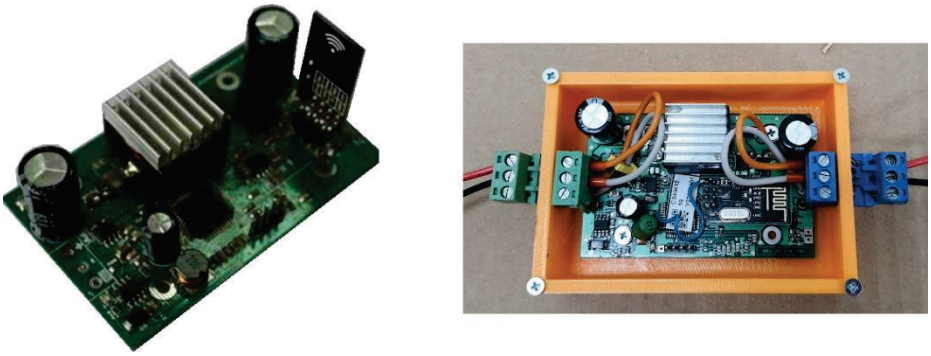

Figure 3.6 Destek Automation Version 5, MPPT.

The MAX efficiency of the relevant MPPT product is 98% and it's topology is boost type. The input voltage (IV) is between 12 - 24 Volts and it can work with PV modules up to 100 Wp. It can provide output voltage between 18 - 36 Volts and can work with Li-Ion, Li-Po, LiFePo4, and NiMH-type batteries. Before the power circuit design and production, the CV and power-voltage circuits of the relevant PV modules were obtained. Related circuits are shared in Figure 3.7, and Figure 3.8. With the determination of the MAX points on these graphs, the values of the electrical loads to be used in the power circuit were determined. As a result of the investigations, it was deemed appropriate to use a 4.7-ohm load.

Table 3.3 Technical properties of the MPPT.

Properties	**Value**
Input Power	100 W
Maximum Efficiency	98%
Type	Boost
Maximum Boost Rate	1.5
Input Voltage	12 – 24 V
Output Voltage	18 – 36 V
Battery	Li-Ion, Li-Po, LiFePo4, NiMH
Physical Properties	80 mm x 60 mm x 25 mm, 58 gr

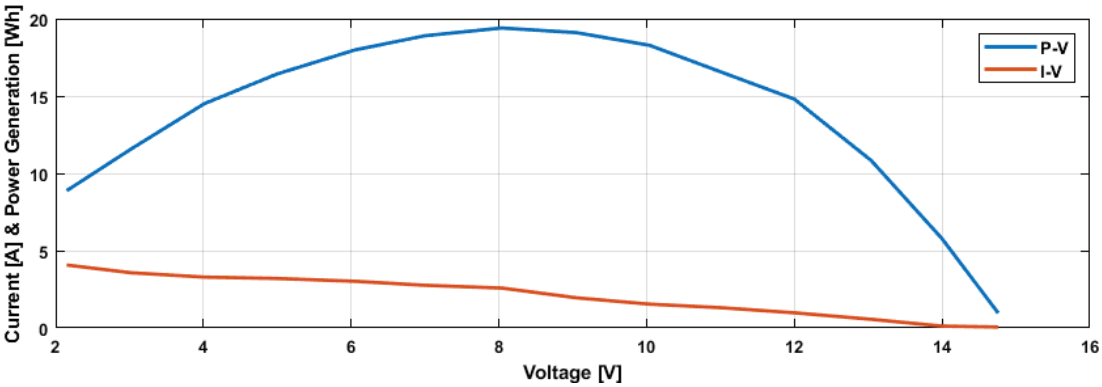

Figure 3.7 Current-voltage and power-voltage schematics of the PV/T module (SR = 600 W/m^2).

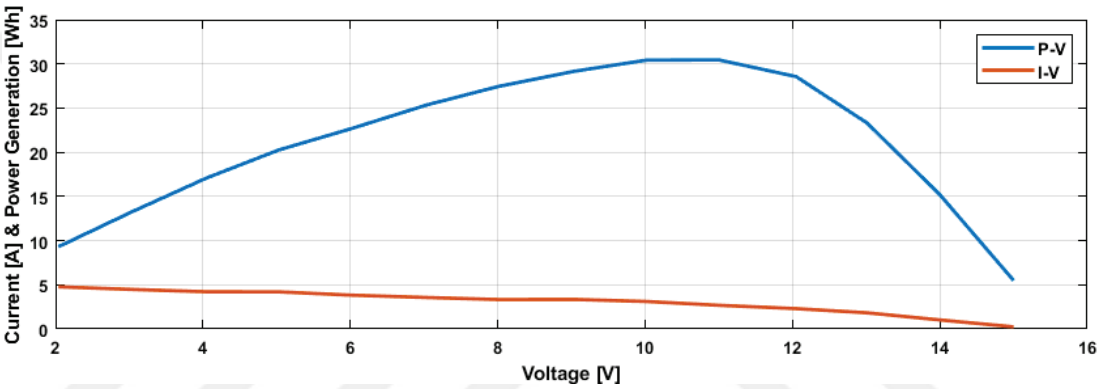

Figure 3.8 Current-voltage and power-voltage schematics of the PV module (SR = 600 W/m^2).

A device has been designed and produced for the tracking and logging of the generated electrical energy values of PV and PV/T modules, simultaneously. In the device, the ATmega328 microcontroller has been used with the RTC, SD, and ACS712 modules. A wiring diagram and source code of this device have been shown in Appendices 5 and 6. According to this diagram, PV and PV/T modules have been connected by MPPTs. In this way, MPPTs scan the instantaneous MAX point and direct the instantaneous voltage to electrical loads. At this point, the current values passing over the electrical loads of known power are read. These read values are processed in the microcontroller and stored on an SD card. The designed and produced device, the generated energy meter (GEM), for the generated electrical energy measurements and logs, has been shown in Figure 3.9.

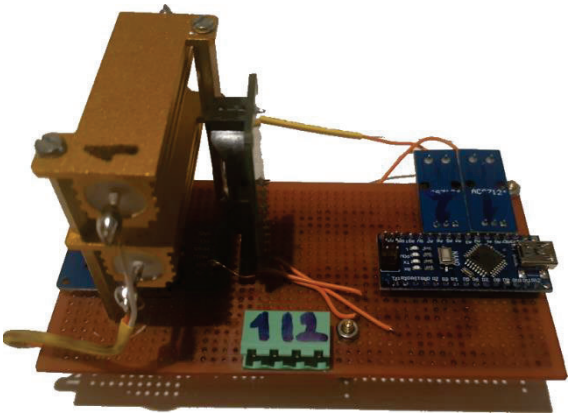

Figure 3.9 Generated energy meter (GEM).

3.1.3 Temperature Measurement

Another measurement in the present study was the temperature measurements of the PV/T, PV modules, water inlet, and outlet of the cooling system. As mentioned before, these component measurements have importance to the definitions of the generated energies of PV/T and PV modules.

For the tracking of the PV/T and PV module temperatures, an infrared camera (IRISYS 1001) has been employed, as shown in Figure 3.10. The infrared camera has been emplaced in front of the modules with taken reference to the laser pointer and logged thermal images of the PV/T and PV modules every 15 minutes during EXP studies. Thermal images of experiments in February, March, and April have also been shown in appendices 8, 9, and 10.

Figure 3.10 IRISYS 1001 infrared camera.

Technical specifications of the infrared camera used in the present study have been shown in Table 3.4. It measures temperatures between -20 °C and 90 °C with 0.5 °C sensitivity. Its frame rate is 6 Hz and could take frames up to 10 with a spectral response of 8 to 14 micrometers. Taken thermal pictures from the infrared camera up to 128x128 pixels. The infrared camera works with a Compaq iPAQ H3600-type pocket PC.

Table 3.4 Technical specifications of the infrared camera (IRISYS 1001).

Properties	**Value**
Temperature Range	-20 - +90 °C
Spectral Response	8 to 14 micrometers
Temperature Sensitivity	0.5 °C
Displayed Image	up to 128x128 pixels
Frame Integration	up to 10 frames
Frame Rate	6 Hz

The other measurements, T_{in} and T_{out} of the cooling system of the PV/T module have been tracked with a digital thermometer (Meterman TMD90). The pictures of the digital thermometer has been shown in Figure 3.11. As shown in this Figure, the digital thermometer has dual-input thermometer. Thus, one of them measures the water inlet temperature, and the other one measures the water outlet temperature of the cooling system.

Figure 3.11 Meterman TMD90 digital thermometer.

Technical specifications of the digital thermoemeter used in the present study have been shown in Table 3.5. The digital thermometer works with K, J, T, R, S, and E types of thermocouples. Its operating conditions are between 0 °C and 50 °C, and the data acquisition interface is RS-232. In the present study, K type thermocouples have been preferred, and its temperature ranges are between -200 °C and 650 °C. The resolution and accuracy of this measurement instrument are 0.1 °C and 0.1%.

Table 3.5 Technical specifications of the digital thermometer (Meterman TMD90).

Properties	**Value**
Thermocouple Type	K, J, T, R, S, and E
Operating Conditions	0 °C and 50 °C
Data Acquisition Interface	RS-232
For the type K thermocouple	
Range	-200 °C to 650 °C
Resolution	0.1 °C
Accuracy	0.1%

3.2 Examination of the Experimental Environment and Preliminary Study

Before the EXP study of laminated PV and PV/T modules, two m-Si PV cells have been laminated separately and one of them has been developed thermally in this subsection for the implementation of preliminary experiments and to define deviations between the numerical (NUM) approach and EXP outcomes. The EXP study has been performed on 23 June 2021 and logged weather data has been shown in Figure 3.12. The experiment was performed for nine hours, finishing at 17 p.m. and after beginning at 8 a.m. The highest SR recorded was 800 W/m^2. The values for the AT and WS ranged from 0 to 25 km/h and 20 to 35 °C, respectively (Korkut, et al., 2022).

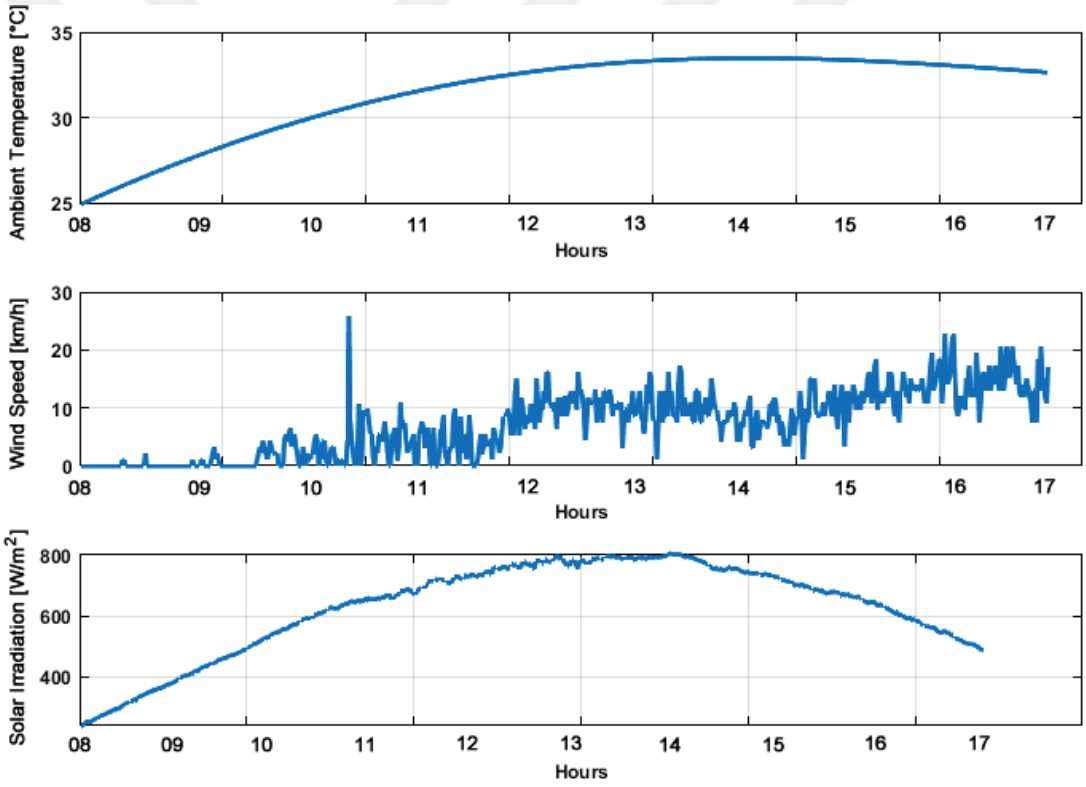

Figure 3.12 Logged weather data on 23 June 2021.

Besides the weather measurements, temperature measurements of PV and PV/T cells by thermocouples have been taken from five different points of each and the schematic diagram of thermocouples has been shown in Figure 3.13. Temperature

measurements of PV and PV/T cells have also been verified by the measurements of the infrared camera hour by hour.

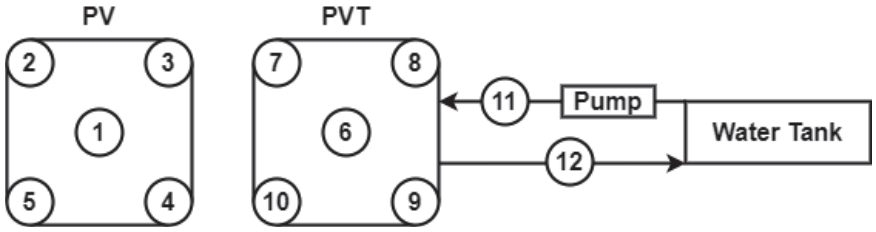

Figure 3.13 Temperature measurement points from PV and PV/T cells.

Simultaneously, measured average PV and PV/T cell temperatures have been shown in Figure 3.14. With respect to temperature logs, the maximum T_{avg} of PV and PV/T cells were 55.95 °C and 33.22 °C. Contrarily, the minimum T_{avg} have been measured as 35.29 °C and 24.98 °C. For this reason, the MAX temperature differences between PV and PV/T cells have been calculated as 20.66 °C and 8.24 °C.

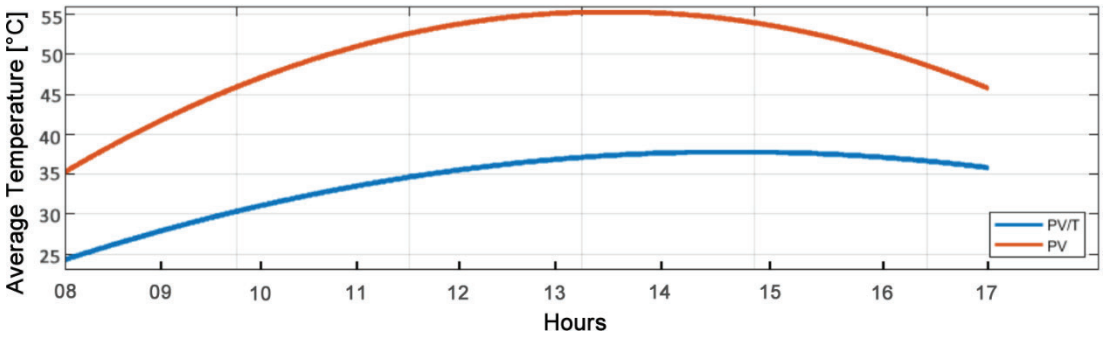

Figure 3.14 Average temperature values of PV and PV/T cells.

η_e and η_{th} measurements of PV and PV/T cells have been shown in Figure 3.15. η_e of PV cell varied between 19% and 21%, whereas the η_e of PV/T cells varied between 20.8% and 21.8%. Besides electrical efficiencies, η_{th} of PV/T cell have been varied between 23.9% and 55.2%. Thus, the η_{total} of PV/T cell varied between 75% and 45%. It has been found that the convective and radiative heat transfer from the PV/T cell during the morning and afternoon was lower than at noon (between 11.30

a.m and 02 p.m.). Because, temperatures of PV and PV/T cell temperatures were close to the AT during indicated parts of the experiment day. At noon, it has been observed that the temperature differences between the PV and PV/T cell surfaces have been increased and it means more possible heat energy to capture by the cooling system of the PV/T cell.

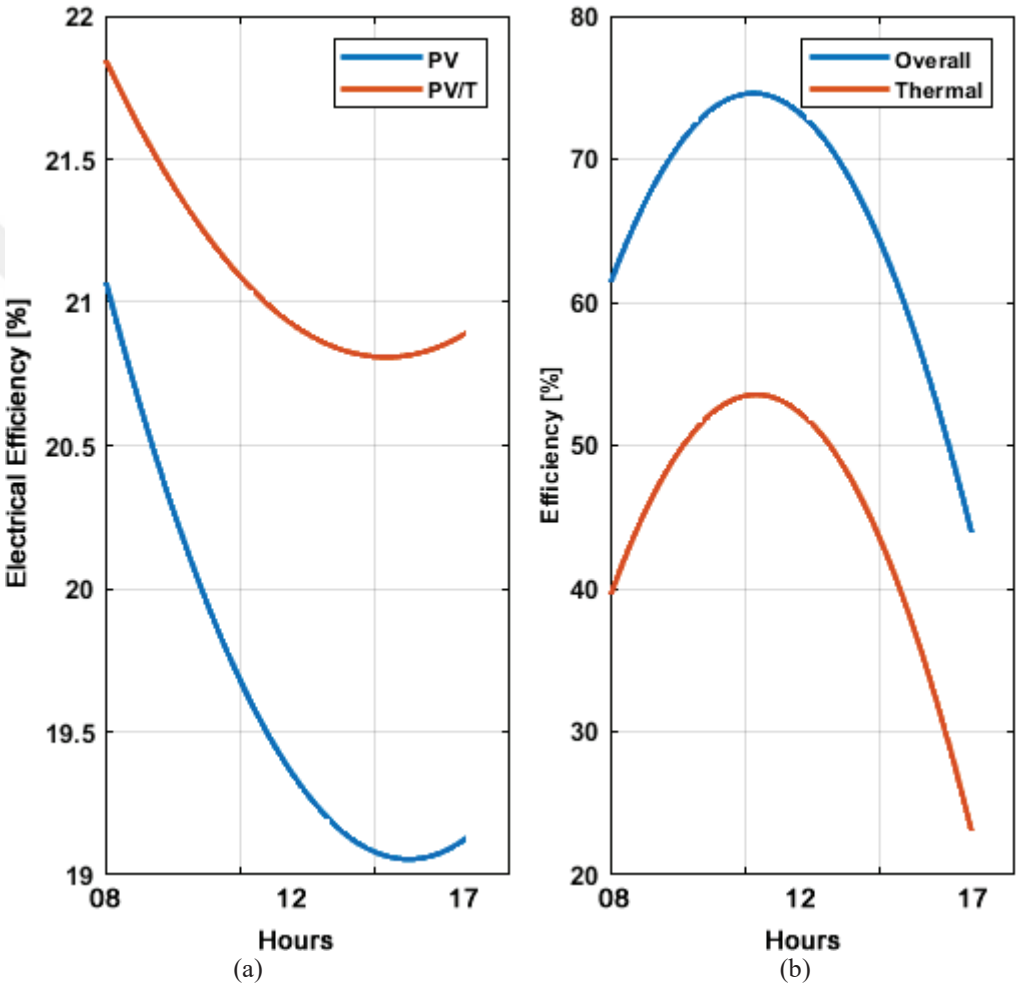

Figure 3.15 η_e of PV and PV/T cells (a), and η_{th} of the PV/T cell (b).

Comparison between the NUM approach outcomes and EXP measurements of PV and PV/T cells have been shown in Figure 3.16. Besides, the thermocouple measurements from PV and PV/T cells have been verified by the infrared camera hour by hour. It has been seen that the results taken from NUM studies have been perfectly matched with the EXP measurements. Deviations between NUM and EXP studies

have been observed between 0.3 °C and 2.2 °C. This means the NUM approach presented in the present study has a 0.2% MAX deviation in η_e of PV and PV/T cells.

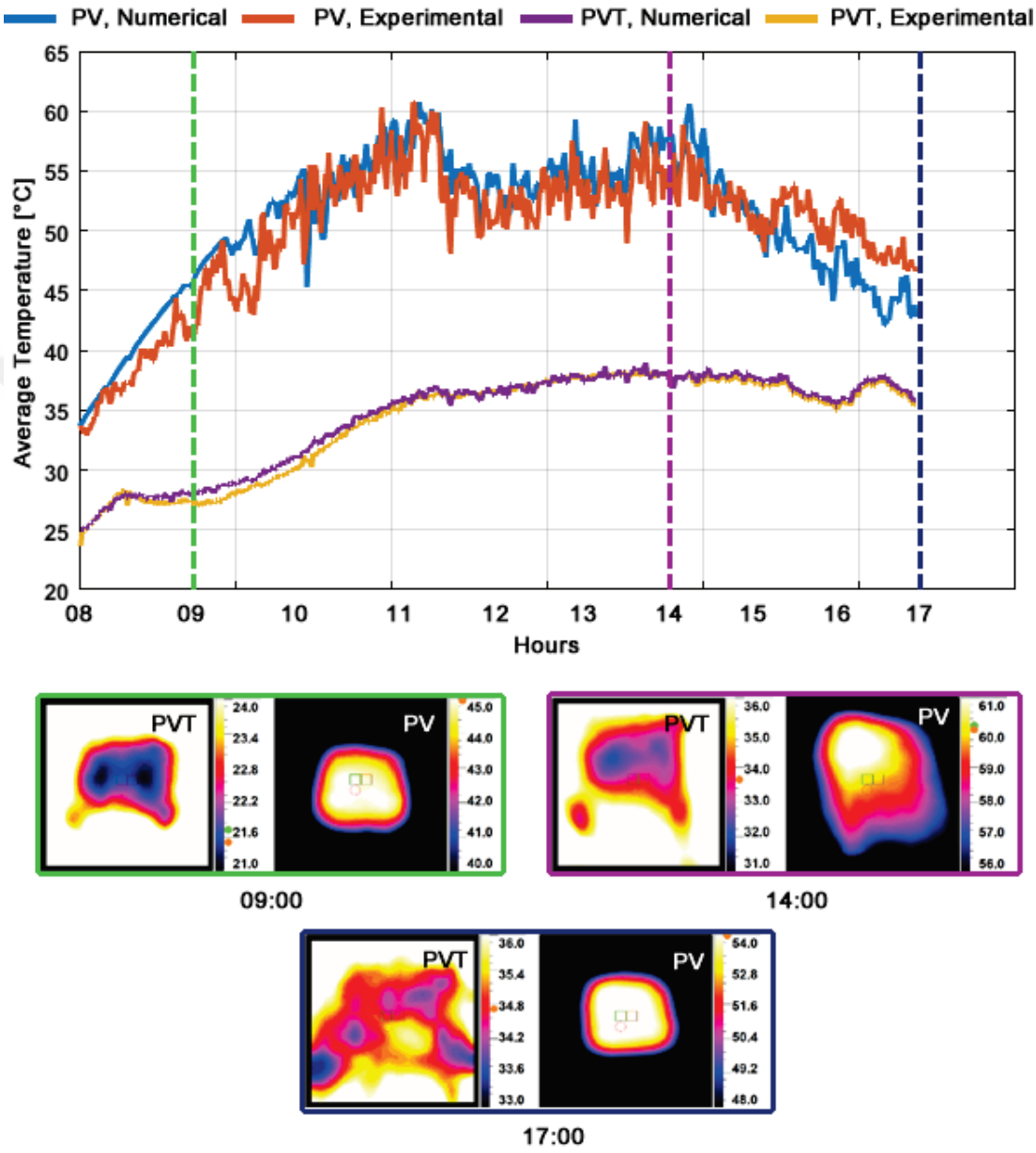

Figure 3.16 Comprehensive results.

Consequently, deviations between NUM and EXP studies showed that the presented NUM approach has been found compatible for performing in future studies.

CHAPTER FOUR
RESULTS AND DISCUSSION

4.1 Definition of the Experimental Conditions

The present study has performed experiments three times, on 23 February, 21 March, and 28 April 2023. Weather conditions are one of the most critical parameters for verifying the defined numerical (NUM) methods with respect to PV and PV/T module performances. For this reason, ambient temperature (AT) (°C), solar radiation (SR) (W/m^2), and wind speed (WS) (km/h) values logged during the experiments have been shown in Figure 4.1, Figure 4.2, and Figure 4.3.

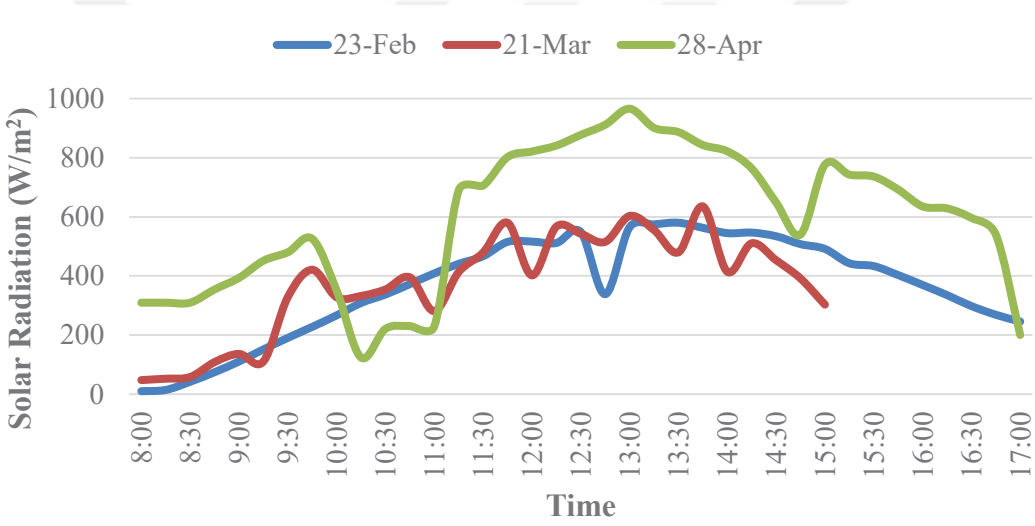

Figure 4.1 Measured solar radiation (W/m^2) values during experiments.

Based on the SR values, experiments in February and March have similar SR characteristics. During these experiments, the maximum (MAX) SR values have been logged 580 W/m^2 in February, and 635 W/m^2 in March experiments. It has been seen that the weather was cloudy in some parts of the experiment period in March. However, the weather was sunny during the February experiment. In the April experiments, it has been seen that the SR values show a strict increase compared to the values in the other two months, February, and March. The MAX SR value has been logged at 965 W/m^2.

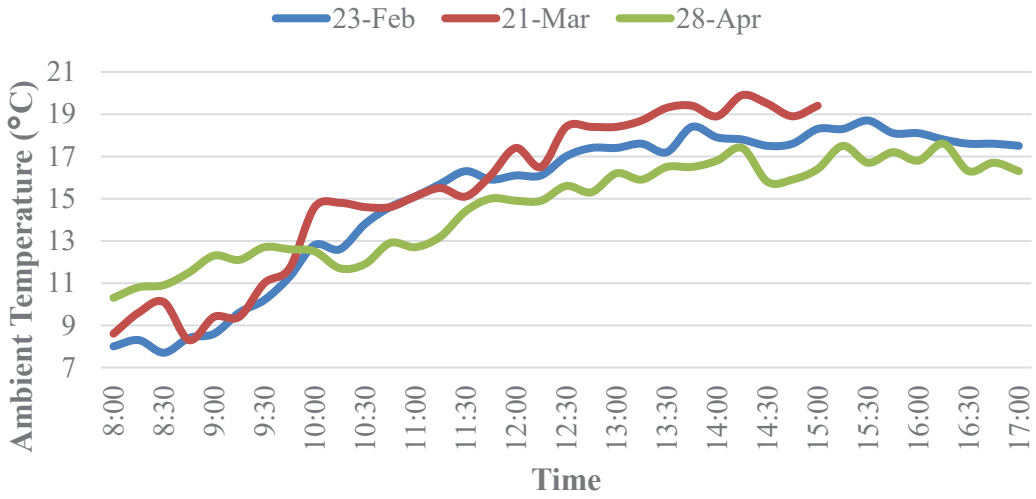

Figure 4.2 Measured ambient temperature (°C) values during experiments.

As mentioned above, based on the AT, February and March experiments have similar characteristics. The MAX and minimum (MIN) values during February experiments have been logged at 8 °C and 18.7 °C. Besides, the AT values in March experiments varied between 8.6 °C and 19.9 °C. Contrary to these months, the MAX and MIN AT values have been logged at 10.3 °C and 17.6 °C in April. Also, it has been seen that the lowest AT value in the April experiment is greater than in the previous months.

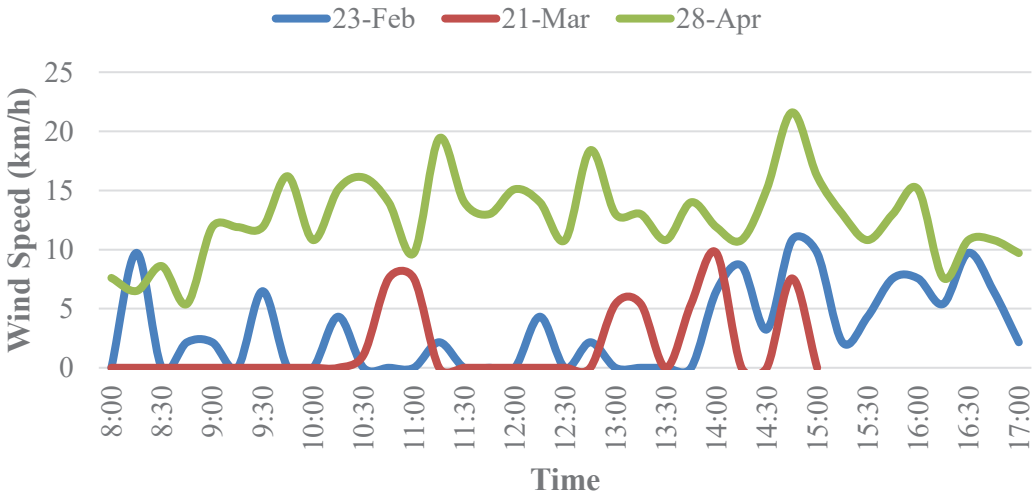

Figure 4.3 Measured wind speed (km/h) values during experiments.

For the WS values, experiments in February and March have similar characteristics. The MAX WS values have been logged at 9.72 km/h and 10.06 km/h during experiments in February and March. Figure 4.3 shows that WS values in the April experiments are more critical than in previous experiments. The weather was generally windy, and the WS value reached 21.6 km/h.

To summarize the weather condition characteristics during the February, March, and April experiments, a table has been represented below.

Table 4.1 Maximum and minimum values of the measured SR, AT, and WS.

1	Solar Radiation (W/m^2)	23 Feb 2023		21 Mar 2023		28 Apr 2023	
		Min	Max	Min	Max	Min	Max
		10	580	47	635	123	965
		Average		Average		Average	
		366		372		590	
2	Ambient Temperature (°C)	23 Feb 2023		21 Mar 2023		28 Apr 2023	
		Min	Max	Min	Max	Min	Max
		8	18.7	8.6	19.9	10.3	17.6
		Average		Average		Average	
		15.10		15.22		14.61	
3	Wind Speed (km/h)	23 Feb 2023		21 Mar 2023		28 Apr 2023	
		Min	Max	Min	Max	Min	Max
		0	9.72	0	10.06	5.40	21.60
		Average		Average		Average	
		3.18		1.71		12.64	

According to Table 4.1, the weather characteristics of these three experiments could be summarized as follows.

- February and March have similar weather characteristics. With the weather conditions in April, spring season characteristics have become more palpable.
- SR in February experiments has continuously increasing trend. March and April were partly cloudy. Average SR values in February, March, and April were 366, 372, and 590 W/m^2.
- February and March have similar ATs, and April is colder than in previous experiments. Average AT values in February, March, and April were 15.1, 15.22, and 14.61 °C.
- February was partly windy, there was no wind in March, and April was generally windy. Average WS values in February, March, and April were 3.18, 1.71, and 12.64 km/h.

4.2 Investigation of the PV and PV/T Module Performances

In this subsection, changing electrical efficiencies, total generated electrical energy values of the PV/T and PV modules, and the overall/thermal efficiency of the PV/T module have been investigated with respect to changing weather conditions, simultaneously.

The average temperatures of the PV module under indicated weather conditions have been shown in Figure 4.4. For the PV module, average temperatures have varied between 6.12 °C and 57.81 °C in February and varied between 6.12 °C and 53.48 °C in March. Besides February and March, the MAX and MIN T_{avg} of the PV module have been logged at 9.57 °C and 53.58 °C in April. Each experiment has been started at 08 a.m., thus, it has been seen that the SR values at the beginning of each experiment increased month by month. This affects the temperature values of the PV modules at the beginning of each experiment. As indicated before, March and April were partly cloudy, the AT values of April were lower than the other months, and the average WS in April was greater than the other months. For this reason, the temperature values of the PV module in March and April have been obtained lower than the experiment in February. Besides, the average temperature values in March and April were more variable than in February because of the cloudy weather in these months.

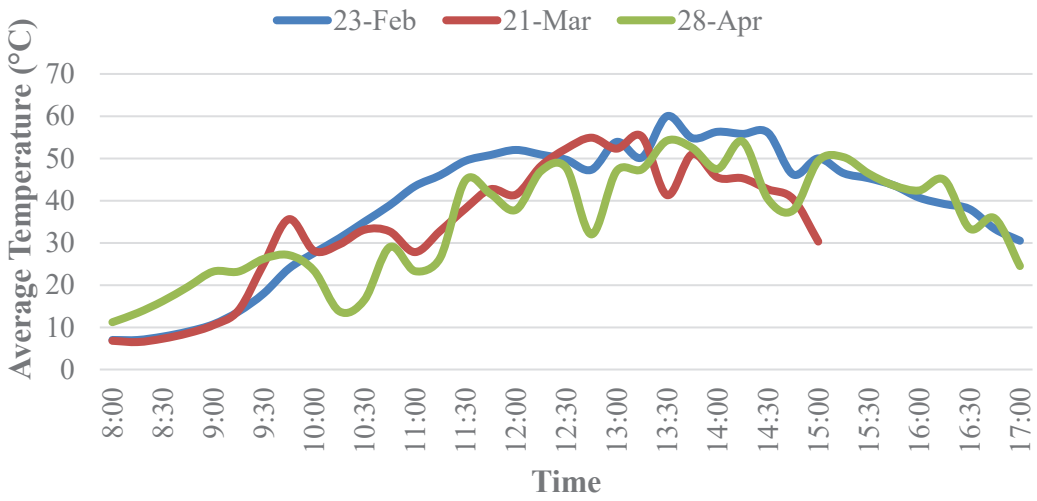

Figure 4.4 Average temperature values (°C) of the PV module.

The average temperatures of the PV/T module under indicated weather conditions have been shown in Figure 4.5. For the PV/T module, temperatures have varied between 7.12 °C and 38.56 °C in February and varied between 6.23 °C and 38.27 °C in March. Besides February and March, the MAX and MIN temperatures of the PV/T module have been logged at 10.84 °C and 37.12 °C.

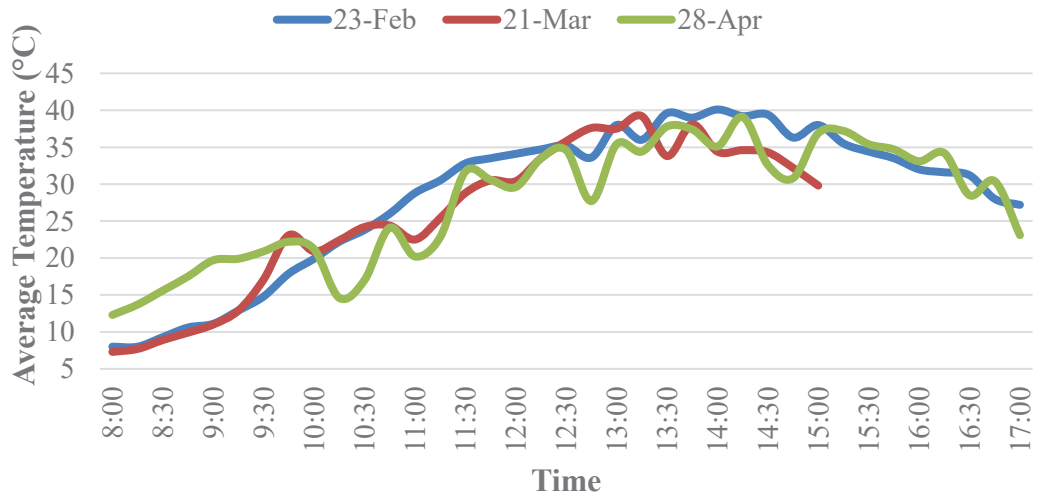

Figure 4.5 Average temperature values (°C) of the PV/T module.

As observed in the PV module, variable temperatures have also been observed on the PV/T module in March and April caused by the windy and cloudy weather conditions in these months. As mentioned in subsubsection 2.6.3, the electrical efficiency of PV modules is affected by changing temperatures. For this reason, PV and PV/T module temperatures have also been investigated to the definition of the changing electrical efficiencies under different weather conditions. Electrical efficiency and measured generated electrical energy values of the PV module have been shown in Figure 4.6, and Figure 4.7.

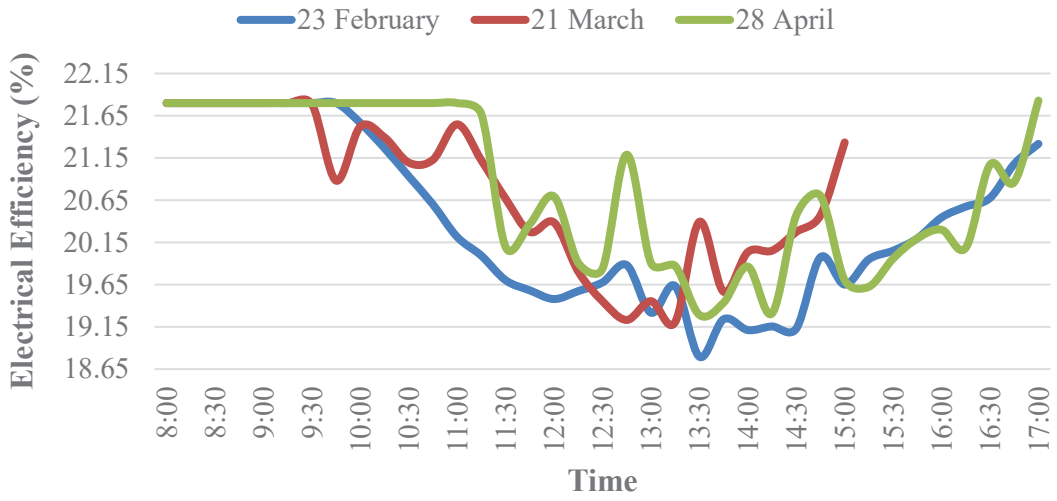

Figure 4.6 η_e of the PV module.

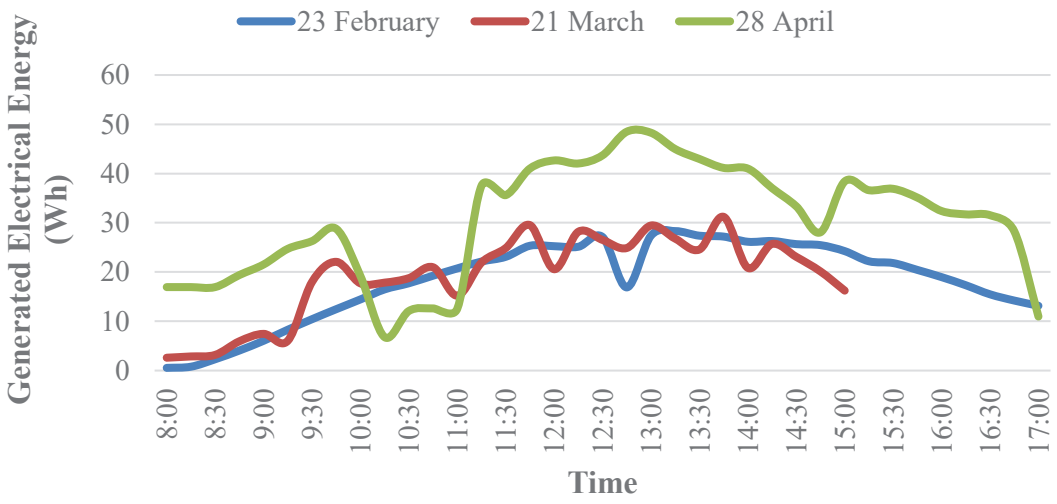

Figure 4.7 Generated electrical energy values (Wh) of the PV module.

For the PV module, the MIN electrical efficiency values have been observed at 18.98% in February, 19.35% in March, and 19.34% in April. A decrease in η_e has been started at 09:45 a.m. in February, 09:30 a.m. in March, and 11:00 a.m. in April experiments. The generated electrical energy values of the PV module have varied between 0.54 Wh and 28.31 Wh in February and varied between 2.61 Wh and 31.21 Wh in March. Besides February and March, the MAX and MIN generated electrical energy values of the PV module have been logged at 6.78 Wh and 48.49 Wh. Electrical efficiency and measured generated electrical energy values of the PV/T module have been shown in Figure 4.8, and Figure 4.9.

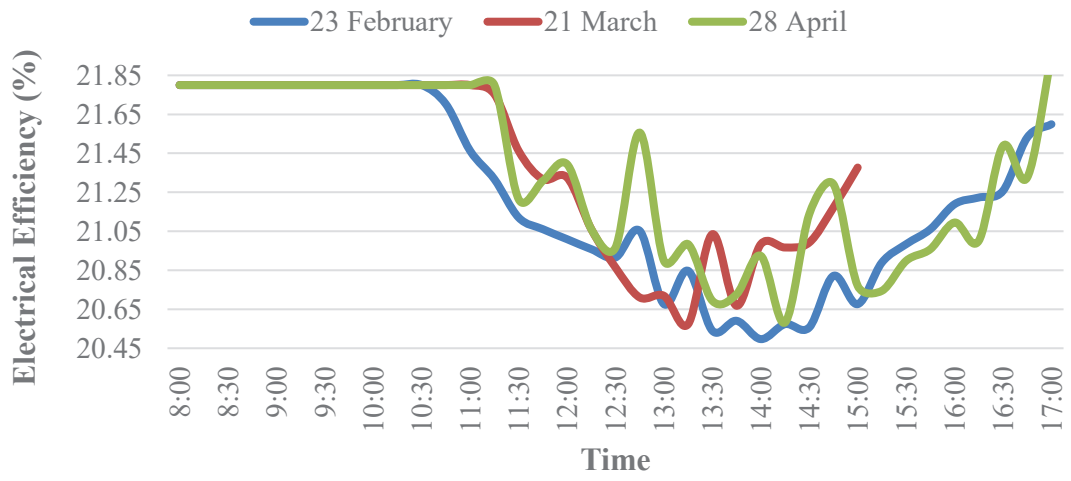

Figure 4.8 η_e of the PV/T module.

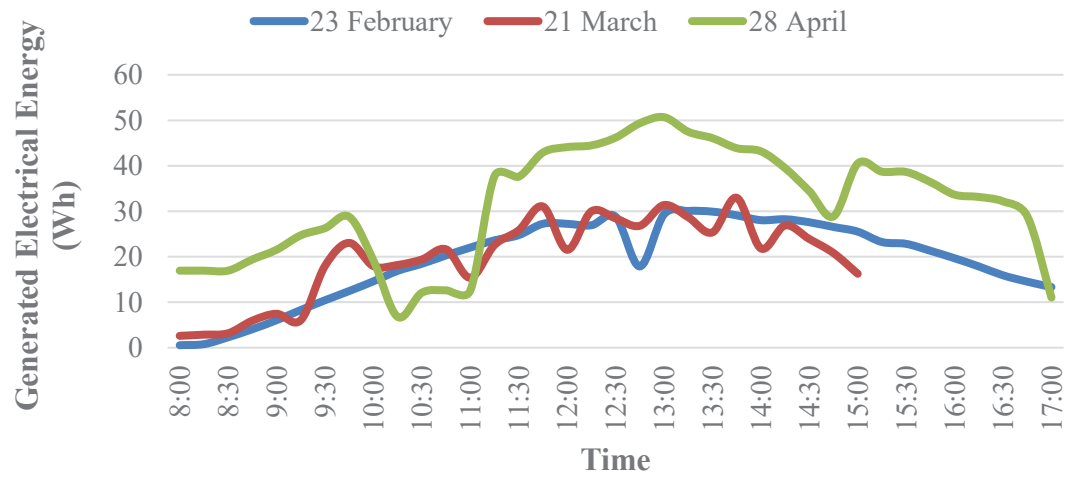

Figure 4.9 Generated electrical energy values (Wh) of the PV/T module.

For the PV/T module, the MIN electrical efficiency values have been observed at 20.63% in February, 20.65% in March, and 20.75% in April. Similar to the PV module, a decrease in electrical efficiency has been started at 10:30 a.m. in February, 11:00 a.m. in March, and 11:15 a.m. in April experiments. Generated electrical energy values of the PV/T module have been varied between 0.54 Wh and 30.06 Wh in February and varied between 2.61 Wh and 32.96 Wh in March. Besides February and March, the MAX and MIN generated electrical energy values of the PV/T module have been logged 6.78 Wh and 50.68 Wh. η_{total} and η_e values of the PV/T module have been shown in Figure 4.10.

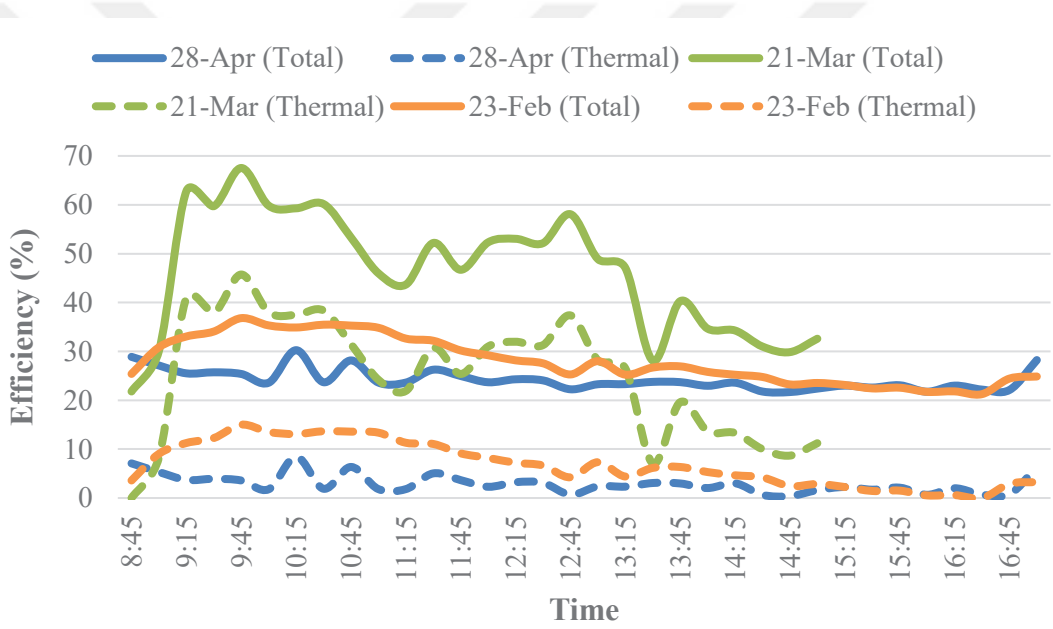

Figure 4.10 η_{total} and η_e values of the PV/T module.

The maximum η_{total} of the PV/T module has been observed in March, and the η_{total} values have varied between 28% and 67%, in this month. The MAX η_{total} in the experiment of March has been followed by experiments in February. In February, the MAX η_{total} value reached 36%, and varied between 21.25% and 36%. In April, the η_{total} values varied between 21.67% and 30.25%. The summary of the PV/T and PV module performances have been shown in Table 4.2.

Table 4.2 Summary of the PV and PV/T module performances.

		PV Module				
		Temperature (°C)		E. Efficiency (%)	Generated Energy (Wh)	
		Max	Min	Min	Max	Min
Months	February	57.81	6.12	18.98	28.31	0.54
	March	53.48	6.12	19.35	31.21	2.61
	April	53.58	9.57	19.34	48.49	6.78
		PV/T Module				
		Temperature (°C)		E. Efficiency (%)	Generated Energy (Wh)	
		Max	Min	Min	Max	Min
Months	February	38.56	7.12	20.63	30.06	0.54
	March	38.27	6.23	20.65	32.96	2.61
	April	37.12	10.84	20.75	50.68	6.78

At the end of the experiments, it has been seen that the PV and PV/T modules have differences in generated electrical energy values and each PV and PV/T modules area were 0.3 m^2. MAX generated electrical energy differences between PV and PV/T modules have been observed at 2.54 Wh at 13:30 p.m. in February, 1.92 Wh at 12:30 p.m. in March, and 3.12 Wh at 13:30 p.m. in April. This means that more generated electrical energy could be obtained with the increasing PV module area. Possible improvements in the generated electrical energy values have been shared in Table 4.3 with respect to obtained MAX generated electrical energy differences between PV and PV/T modules.

Table 4.3 Estimation of the generated electrical energy values (Wh) with respect to increasing PV module area.

		PV Module Area (m^2)				
		0.3 m^2	1 m^2	5 m^2	10 m^2	20 m^2
Months	February	2.54	8.46	42.32	84.63	169.26
	March	1.92	6.41	32.03	64.06	128.14
	April	3.12	10.40	52.00	104.00	208.02

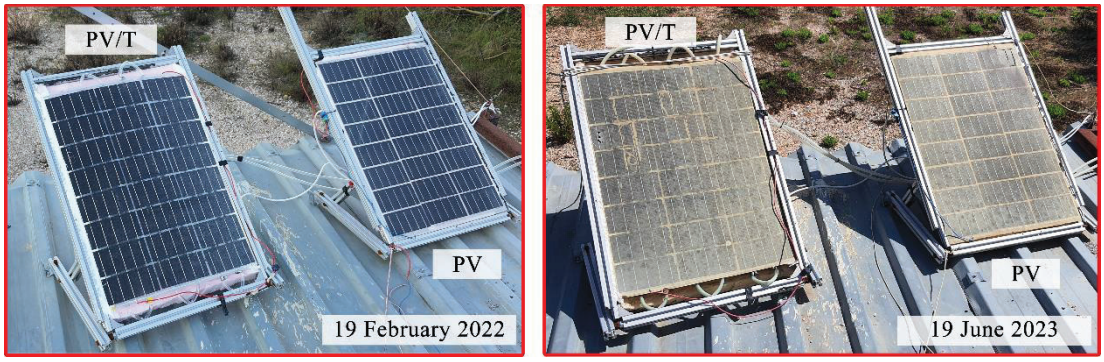

(a)

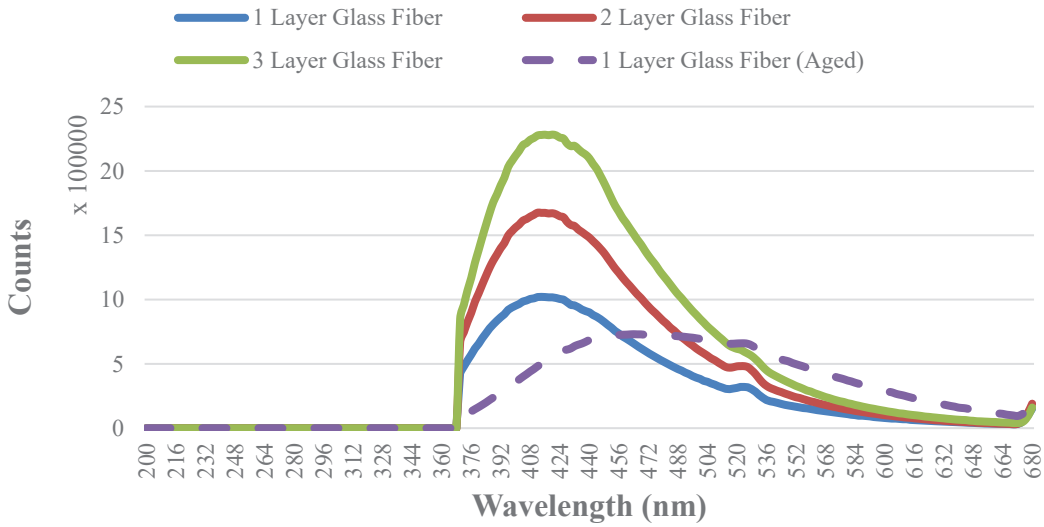

(b)

Figure 4.11 Change of appearance on the PV/T and PV modules and performed emission test results.

At the end of the study, an optical change in the PV/T and PV modules, with more yellowish surfaces than the first time, has been noticed. The change in the appearance of PV/T and PV modules and performed emission test results have been shown in Figure 4.11.a. Besides, performed emission test results have been shown in Figure 4.11.b. Experiments between the wavelength of 370 and 680 nm have been implemented based on four different specimens. These are unaged PV cells with 1 layer, 2 layers, and 3 layers of glass fiber on the sun-facing side, and the aged PV cell with 1 layer of glass fiber on the sun-facing side. Results showed that the increasing number of glass fiber layers increases the emission value of the laminated PV cell.

Besides the number of layers, it has been seen that the emission value decreases with the aged PV cell. For this reason, the author also would like to indicate the outcomes from the optical changes between the aged and unaged PV lamination and optical changes in the laminated PV module could be obtained through accelerated aging techniques (Barbosa, et al., 2017).

4.3 Numerical Verification of Experiments

In this subsection, temperatures of PV and PV/T modules have been validated by the computational fluid dynamics (CFD) methods indicated in subsection 2.6 with respect to changing weather conditions, simultaneously. Temperature distributions (TDIST) of PV and PV/T modules with respect to NUM and experimental (EXP) studies in February have been shown in Figure 4.12.

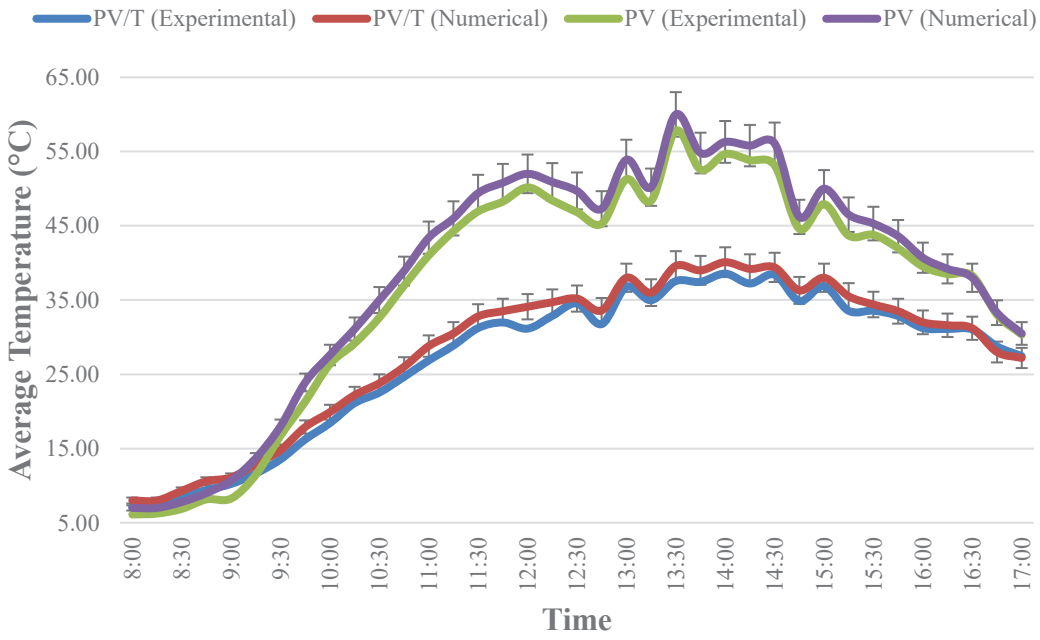

Figure 4.12 Average TDIST and comparison between the numerical and experimental studies in February.

For the PV/T module, the MAX and MIN temperatures have been observed at 40.1 °C (14 p.m.) and 8 °C (08 a.m.). Besides the PV/T module, 60 °C (13:30 p.m.) and 7 °C (08 a.m.) have been measured for the PV module. The MAX temperature variations

between NUM and EXP studies has been calculated at 2.95 °C and 2.82 °C for the PV/T and PV modules. Error bars that cover +/- 2% have been drawn on the EXP curves to obtain a clear understanding of the error rate between the NUM approach and experiments. Results showed that the NUM approach perfectly matched the experiment in February. TDIST of PV and PV/T modules with respect to NUM and EXP studies in March have been shown in Figure 4.13.

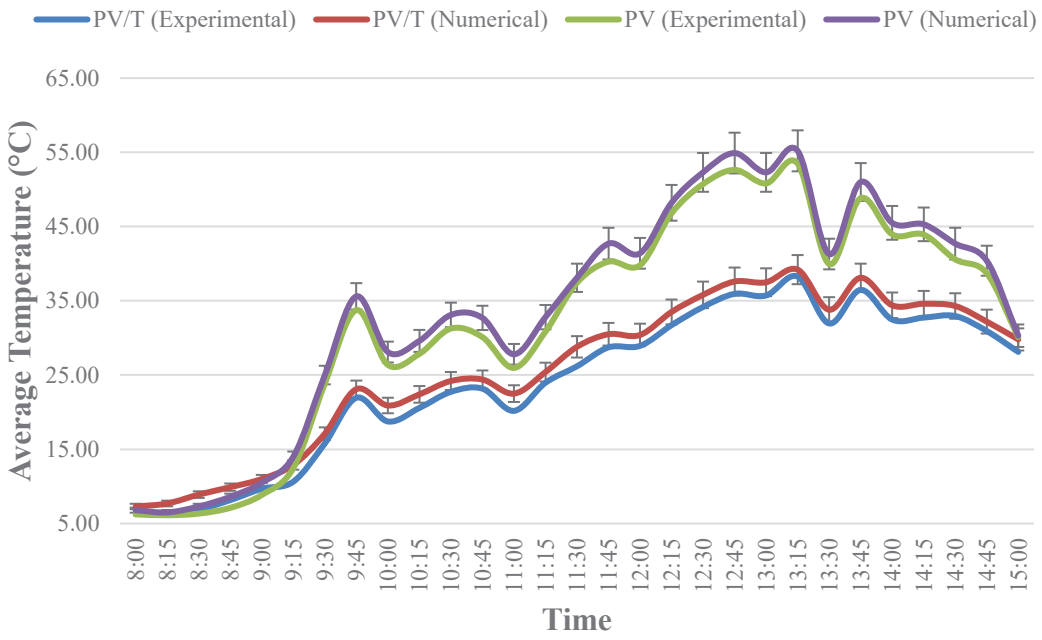

Figure 4.13 Average TDIST and comparison between the numerical and experimental studies in March.

In March, the temperature of the PV/T module has been reached 39.2 °C (13:15 p.m.), and the lowest temperature has been calculated at 7.3 °C (08:15 a.m.). Besides the PV/T module, the MAX and MIN temperatures of the PV module have been observed at 55.2 °C (13:15 p.m.), and 6.5 °C (08:15 a.m.). The MAX temperature difference between NUM and EXP studies has been calculated at 2.62 °C and 2.58 °C for the PV/T and PV modules. Like calculations in February, results showed that the outcomes from NUM studies in March could be acceptable with respect to the defined error rate. TDIST of PV and PV/T modules with respect to NUM and EXP studies in April have been shown in Figure 4.14.

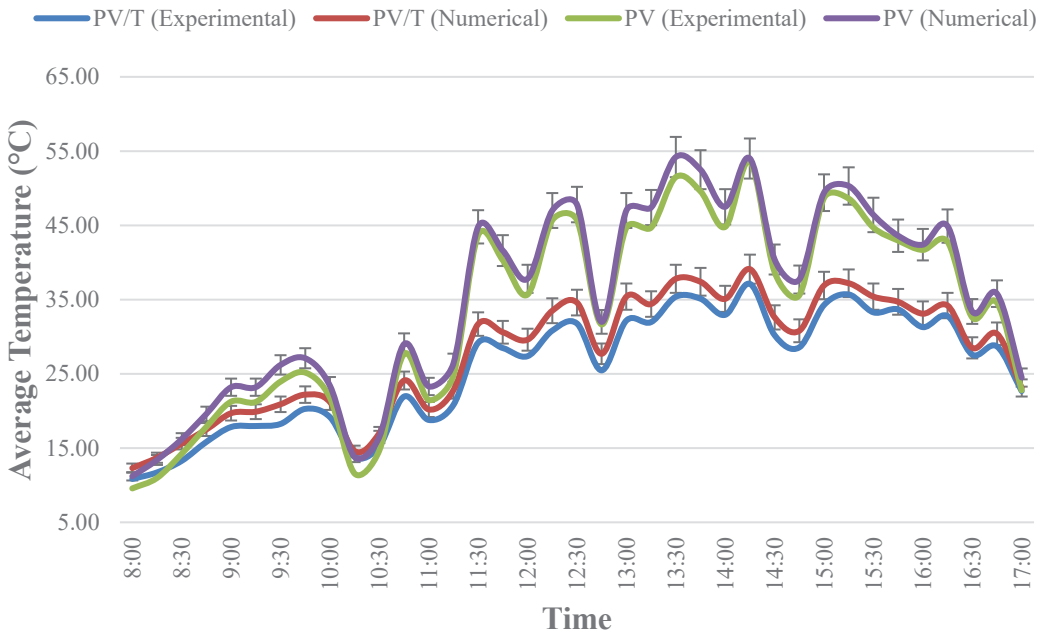

Figure 4.14 TDIST and comparison between the numerical and experimental studies in April.

In April, the MAX and MIN temperatures of the PV/T module have been calculated at 39.1 °C (14:15 p.m.) and 12.3 °C (08 a.m.). Besides, have been calculated 54.2 °C (14:15 p.m.) and 11.2 °C (08 a.m.) for the PV module. The MAX deviation between the NUM and EXP studies has been observed at 3.22 °C and 2.92 °C for the PV/T and PV modules. As mentioned in the previous comparison of the NUM approach and experiments, results showed that the NUM approach perfectly matched the experiment in April. Besides, the TDIST of the PV/T and PV modules pictures have been shown in Figure 4.15 and Figure 4.16 to understand the accuracy of the NUM method.

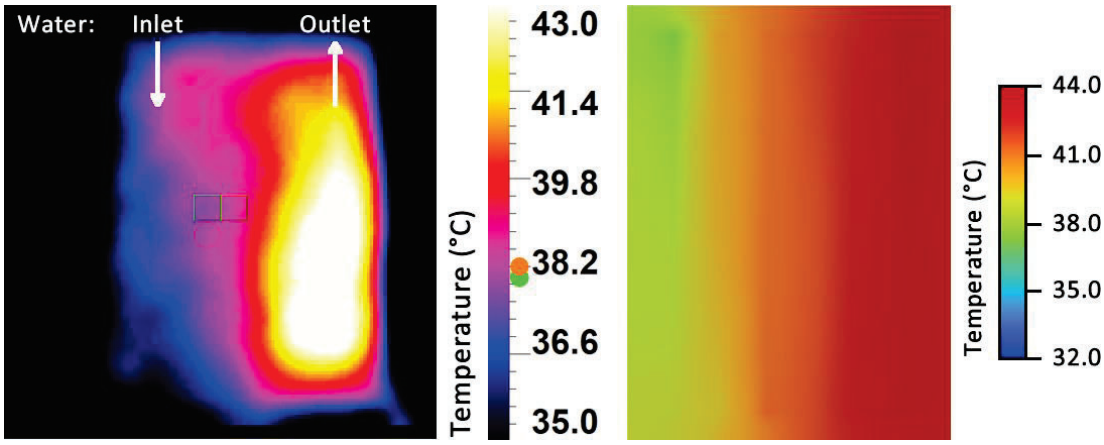

Figure 4.15 The TDIST pictures of the PV/T module from the infrared camera and CFD method at 13 p.m. in February.

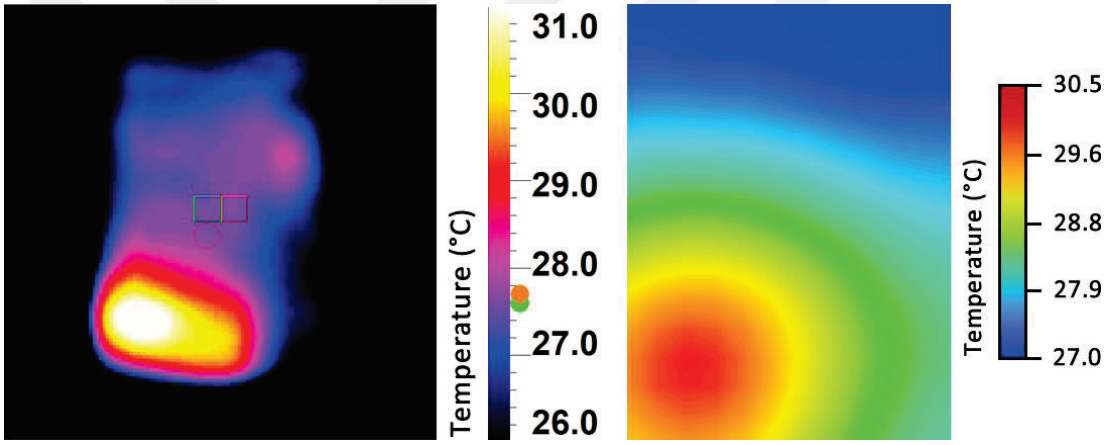

Figure 4.16 The TDIST pictures of the PV module from the infrared camera and CFD method at 10 a.m. in February.

After the comparison of results from the NUM studies and experiments, another comparison, graphical outcomes from the infrared camera and CFD method have been obtained and compared to the verification of the NUM method used in the present research. In Figure 4.15, pictures from the infrared camera and CFD method at 13 p.m. in February have been shown to detailed analyze the TDIST on the PV/T module. The active cooling system of the PV/T module was designed as serpentine, and as expected, the water inlet side (left side) of the PV/T module temperature was lower than the water outlet side (right side) of this PV/T module. It has been seen that the TDISTs and values obtained from the CFD method were matched with the experiment, picture from the infrared camera. As obtained from experiments, the CFD method also has a

TDIST from left to right side warmer. It has temperature values within the 1.5 °C average deviation with respect to the picture from the infrared camera.

PV/T and PV modules have different thermal characteristics during the present study. For this reason, the TDIST of the PV module has also been investigated besides the PV/T module. The TDISTs obtained from the infrared camera and CFD method of the PV module at 10 a.m. in February have been shown in Figure 4.16. During the experiments, the bottom-left side of the PV module temperatures were warmer than the top side. Outcomes from the CFD method have similar responses to the implemented experiments. The bottom-left side of the PV module has also been warmer than the top side of the PV module. Besides the TDISTs, the temperature values within the 1.1 °C average deviation with respect to the picture from the infrared camera.

CHAPTER FIVE
CONCLUSION

The aim of this study is to lamination of PV cells with the use of FRPMC materials and VARTM method and definition of the performance with and without a thermally development under different weather conditions. In the continuation of the study, experimental outcomes of the PV/T and PV modules have been verified by the CFD method.

Contrary to the conventional lamination techniques of PV cells, PV cells laminated with the use of FRPMC materials have shown promise for future studies on increasing power generation with respect to the increase of heat transfer performance away from PV cells. With the thermally developed PV module, an improvement in generated electrical energy between 6.41 Wh and 10.4 Wh has been achieved for a 1 m^2 PV array area. Implemented CFD method has been perfectly matched with the experimental studies. It has been seen that the TDIST on PV/T and PV modules are compatible with pictures taken from the infrared camera and CFD studies. The maximum temperature difference between experiments and CFD studies has been obtained at 3.22 °C in April. After the comparison with experiments, the T_{avg} values of PV/T and PV modules from CFD studies have been found within the +/- 2% deviation. Apart from the PV/T and PV module performances, the author would like to indicate that the effects of optical changes on the PV module laminations, and an efficient controller design for the active cooling systems depending on yearly generated electrical energy yields could be studied in further research studies.

REFERENCES

Alzaabi, A. A., Badawiyeh, N. K., Hantoush, H. O., & Hamid, A. K. (2014). Electrical/thermal performance of hybrid PV/T system in Sharjah, UAE. *International Journal of Smart Grid and Clean Energy, 3*(4), 385-389. https://doi.org/10.12720/sgce.3.4.385-389

Armstrong, S., & Hurley, W. G. (2010). A thermal model for photovoltaic panels under varying atmospheric conditions. *Applied thermal engineering, 30*(11-12), 1488-1495. https://doi.org/10.1016/j.applthermaleng.2010.03.012

Atmaca, M., & Pektemir, I. Z. (2019). An investigation on the effect of the total efficiency of water and air used together as a working fluid in the photovoltaic thermal systems. *Processes, 7*(8), 516. https://doi.org/10.3390/pr7080516

Barbosa, A. P. C., Fulco, A. P. P., Guerra, E. S., Arakaki, F. K., Tosatto, M., Costa, M. C. B., & Melo, J. D. D. (2017). Accelerated aging effects on carbon fiber/epoxy composites. *Composites Part B: Engineering, 110*, 298-306. https://doi.org/10.1016/j.compositesb.2016.11.004

Bhatt, P., & Goe, A. (2017). Carbon fibres: production, properties and potential use. *Mater. Sci. Res. India, 14*(1), 52-57. http://dx.doi.org/10.13005/msri/140109

Bird, R. B. (2002). Transport phenomena. *Appl. Mech. Rev., 55*(1), R1-R4. https://doi.org/10.1115/1.1424298

Blättner, W. (1983). Utilization instruction for the BRITE Monte-Carlo procedure. *Radiation Research Associates, Fort Worth, TX, 104*.

Campbell Jr, F. C. (Ed.). (2003). *Manufacturing processes for advanced composites. Elsevier*.

Cattani, L. (2012). Numerical investigation of the convective heat transfer enhancement in coiled tubes. *In 2012 COMSOL Conference in Milan* (Vol. 320, pp. 330-340).

Charalambous, P. G., Kalogirou, S. A., Maidment, G. G., & Yiakoumetti, K. (2011). Optimization of the photovoltaic thermal (PV/T) collector absorber. *Solar Energy, 85*(5), 871-880. https://doi.org/10.1016/j.solener.2011.02.003

Chawla, K. K. (2012). *Composite materials: science and engineering*. *Springer Science & Business Media*.

Cristofari, C., Notton, G., & Canaletti, J. L. (2009). Thermal behavior of a copolymer PV/Th solar system in low flow rate conditions. *Solar Energy, 83*(8), 1123-1138. https://doi.org/10.1016/j.solener.2009.01.008

Daghigh, R., Ruslan, M. H., Zaharim, A., & Sopian, K. (2011, February). Monthly performance of a photovoltaic thermal (PV/T) water heating system. In *Proceedings of the 6th IASME/WSEAS International Conference on Energy & Environment, Cambridge, UK* (pp. 23-25).

DiBenedetto, A. T. (1987). Prediction of the glass transition temperature of polymers: a model based on the principle of corresponding states. *Journal of Polymer Science Part B: Polymer Physics, 25*(9), 1949-1969. https://doi.org/10.1002/polb.1987.090250914

Dubey, S., & Tay, A. A. (2013). Testing of two different types of photovoltaic–thermal (PVT) modules with heat flow pattern under tropical climatic conditions. *Energy for Sustainable Development, 17*(1), 1-12. https://doi.org/10.1016/j.esd.2012.09.001

Elsanadedy, H. M., Abbas, H., Almusallam, T. H., & Al-Salloum, Y. A. (2019). Organic versus inorganic matrix composites for bond-critical strengthening applications of RC structures–State-of-the-art review. *Composites Part B: Engineering, 174*, 106947. https://doi.org/10.1016/j.compositesb.2019.106947

Evans, D. L. (1981). Simplified method for predicting photovoltaic array output. *Solar Energy, 27*(6), 555-560. https://doi.org/10.1016/0038-092X(81)90051-7

Everett, R., Boyle, G., Peake, S., & Ramage, J. (2012). *Energy systems and sustainability: power for a sustainable future*. Oxford Univerity Press.

Gang, P., Huide, F., Tao, Z., & Jie, J. (2011). A numerical and experimental study on a heat pipe PV/T system. *Solar Energy, 85*(5), 911-921. https://doi.org/10.1016/j.solener.2011.02.006

Giannouli, M., Drakonakis, V. M., Savva, A., Eleftheriou, P., Florides, G., & Choulis, S. A. (2015). Methods for improving the lifetime performance of organic photovoltaics with low‐costing encapsulation. *ChemPhysChem, 16*(6), 1134-1154. https://doi.org/10.1002/cphc.201402749

Gören, A. (2017). Solar energy harvesting in electro mobility. *Energy Harvesting and Energy Efficiency: Technology, Methods, and Applications,* 293-326. https://doi.org/10.1007/978-3-319-49875-1_11

Goren, A., & Atas, C. (2008). Manufacturing of polymer matrix composites using vacuum assisted resin infusion molding. *Archives of materials Science and Engineering, 34*(2), 117-120.

Green, M., Dunlop, E., Hohl‐Ebinger, J., Yoshita, M., Kopidakis, N., & Hao, X. (2021). Solar cell efficiency tables (version 57). *Progress in photovoltaics: research and applications, 29*(1), 3-15. https://doi.org/10.1002/pip.3371

Haddad, S., Touafek, K., & Khelifa, A. (2015, March). Investigation of the electrical and thermal performance of a PV/T hybrid system. In *2015 Tenth International Conference on Ecological Vehicles and Renewable Energies (EVER)* (pp. 1-6). IEEE. https://doi.org/10.1109/EVER.2015.7112928

Hakiki, F., Salam, D. D., Akbari, A., Nuraeni, N., Aditya, W., & Siregar, S. (2015, October). Is epoxy-based polymer suitable for water shut-off application?. In *SPE/IATMI Asia Pacific Oil & Gas Conference and Exhibition*. OnePetro. https://doi.org/10.2118/176457-MS

Hara, O. (1990). Curing agents for epoxy resin. *Three bond technical news, 32*(20), 1-10.

He, W., Zhang, Y., & Ji, J. (2011). Comparative experiment study on photovoltaic and thermal solar system under natural circulation of water. *Applied Thermal*

Engineering, 31(16), 3369-3376. https://doi.org/10.1016/j.applthermaleng.2011.06.021

Hegedűs, G., Sarkadi, T., & Czigány, T. (2017). Analysis of the light transmission ability of reinforcing glass fibers used in polymer composites. *Materials, 10*(6), 637. https://doi.org/10.3390/ma10060637

Hu, M., Zheng, R., Pei, G., Wang, Y., Li, J., & Ji, J. (2016). Experimental study of the effect of inclination angle on the thermal performance of heat pipe photovoltaic/thermal (PV/T) systems with wickless heat pipe and wire-meshed heat pipe. *Applied Thermal Engineering, 106*, 651-660. https://doi.org/10.1016/j.applthermaleng.2016.06.003

Hussain, F., Othman, M. Y. H., Yatim, B., Ruslan, H., Sopian, K., Anuar, Z., & Khairuddin, S. (2015). An improved design of photovoltaic/thermal solar collector. *Solar Energy, 122*, 885-891. https://doi.org/10.1016/j.solener.2015.10.008

Ibrahim, A., Fudholi, A., Sopian, K., Othman, M. Y., & Ruslan, M. H. (2014). Efficiencies and improvement potential of building integrated photovoltaic thermal (BIPVT) system. *Energy conversion and management, 77*, 527-534. https://doi.org/10.1016/j.enconman.2013.10.033

Ibrahim, A., Othman, M. Y., Ruslan, M. H., Alghoul, M., Yahya, M., Zaharim, A., & Sopian, K. (2009). Performance of photovoltaic thermal collector (PVT) with different absorbers design. *WSEAS Transactions on Environment and Development, 5*(3), 321-330.

Jahromi, S. N., Vadiee, A., & Yaghoubi, M. (2015). Exergy and economic evaluation of a commercially available PV/T collector for different climates in Iran. *Energy Procedia, 75*, 444-456. https://doi.org/10.1016/j.egypro.2015.07.416

Jin, F. L., Li, X., & Park, S. J. (2015). Synthesis and application of epoxy resins: A review. *Journal of Industrial and Engineering Chemistry, 29*, 1-11. https://doi.org/10.1016/j.jiec.2015.03.026

Joshi, S. S., & Dhoble, A. S. (2018). Photovoltaic-Thermal systems (PVT): Technology review and future trends. *Renewable and Sustainable Energy Reviews, 92*, 848-882. https://doi.org/10.1016/j.rser.2018.04.067

Khelifa, A., Touafek, K., Moussa, H. B., Tabet, I., & Haloui, H. (2015). Analysis of a hybrid solar collector photovoltaic thermal (PVT). *Energy Procedia, 74*, 835-843. https://doi.org/10.1016/j.egypro.2015.07.819

Kiran, S., & Devadiga, U. (2014). Performance analysis of hybrid PV/Thermal systems. *Int. J. Emerg. Technol. Adv. Eng, 4*(3), 80-86.

Korkut, T. B., & Gören, A. (2022). Güneş panellerinde polimer kompozit malzeme kullanımı ile optimum ısı transferi performansının elde edilmesi. *Uludağ Üniversitesi Mühendislik Fakültesi Dergisi, 27*(3), 1177-1192. https://doi.org/10.17482/uumfd.1107891

Korkut, T. B., Gören, A., & Rachid, A. (2022). Numerical and Experimental Study of a PVT Water System under Daily Weather Conditions. *Energies, 15*(18), 6538. https://doi.org/10.3390/en15186538

Launikitis, M. B. (1982). Vinyl ester resins. *Handbook of composites*, 38-49. https://doi.org/10.1007/978-1-4615-7139-1_3

Lee, B., Liu, J. Z., Sun, B., Shen, C. Y., & Dai, G. C. (2008). Thermally conductive and electrically insulating EVA composite encapsulants for solar photovoltaic (PV) cell. *Express Polym Lett, 2*(5), 357-363. https://doi.org/10.3144/expresspolymlett.2008.42

Levi, D. H., Green, M. A., Hishikawa, Y., Dunlop, E. D., Hohl-Ebinger, J., & Ho-Baillie, A. W. (2017). Solar cell efficiency tables (version 51). *Progress in Photovoltaics, 26*(NREL/JA-5J00-70757). https://doi.org/10.1002/pip.2978

Liu, C., Qin, H., & Mather, P. T. (2007). Review of progress in shape-memory polymers. *Journal of materials chemistry, 17*(16), 1543-1558. DOI https://doi.org/10.1039/B615954K

Long, H., Chow, T. T., & Ji, J. (2017). Building-integrated heat pipe photovoltaic/thermal system for use in Hong Kong. *Solar Energy, 155*, 1084-1091. https://doi.org/10.1016/j.solener.2017.07.055

Makki, A., Omer, S., & Sabir, H. (2015). Advancements in hybrid photovoltaic systems for enhanced solar cells performance. *Renewable and sustainable energy reviews, 41*, 658-684. https://doi.org/10.1016/j.rser.2014.08.069

Manual, U. D. F. (2009). ANSYS FLUENT 12.0. Theory Guide.

Matthews, F. L., & Rawlings, R. D. (1999). *Composite materials: engineering and science*. Woodhead Publishing.

Mera, H., & Takata, T. (2000). High‐performance fibers. Ullmann's Encyclopedia of Industrial Chemistry.

Misha, S., Abdullah, A. L., Tamaldin, N., Rosli, M. A. M., & Sachit, F. A. (2020). Simulation CFD and experimental investigation of PVT water system under natural Malaysian weather conditions. *Energy Reports, 6*, 28-44. https://doi.org/10.1016/j.egyr.2019.11.162

Moosmüller, H., Giri, R., Sorensen, C. M., & Berg, M. J. (2021). Black metal nanoparticles from abrasion processes in everyday life: Bicycle drivetrains and rock-climbing ropes. *Optics Communications, 479*, 126413. https://doi.org/10.1016/j.optcom.2020.126413

Murashov, V. V. (2012). Control of multilayer glued constructions of polymeric composite materials. *Polymer Science Series D, 5*, 109-115. https://doi.org/10.1134/S1995421212020104

Myers, D. R., Emery, K., & Gueymard, C. (2004). Revising and validating spectral irradiance reference standards for photovoltaic performance evaluation. *J. Sol. Energy Eng., 126*(1), 567-574. https://doi.org/10.1115/1.1638784

Nahar, A., Hasanuzzaman, M., & Rahim, N. A. (2017). A three-dimensional comprehensive numerical investigation of different operating parameters on the

performance of a photovoltaic thermal system with pancake collector. *Journal of Solar Energy Engineering, 139*(3). https://doi.org/10.1115/1.4035818

Nishimura, J., & Morishita, K. (1997). Control of spectral characteristics of dispersive optical fibers by annealing. *Journal of lightwave technology, 15*(2), 294-298. https://doi.org/10.1109/50.554380

Page, C. H., & Vigoureux, P. (Eds.). (1974). *The international system of units (SI)* (Vol. 330). US Department of Commerce, National Bureau of Standards.

Palaskar, V. N., & Deshmukh, S. P. (2015). Waste heat recovery study of spiral flow heat exchanger used in hybrid solar system with reflectors. *Science, 5*, 476-82.

Palz, W. (2010). *Power for the world: the emergence of electricity from the Sun*. Pan Stanford Publishing.

Patankar, S. (2018). *Numerical heat transfer and fluid flow*. Taylor & Francis.

Pilato, L. A., & Michno, M. J. (1994). *Advanced composite materials*. Springer Science & Business Media.

Prasad, A. A., Taylor, R. A., & Kay, M. (2017). Assessment of solar and wind resource synergy in Australia. *Applied Energy, 190*, 354-367. https://doi.org/10.1016/j.apenergy.2016.12.135

ullah Qureshi, A. (2022). *Vibration Analysis of Composites Beams Structure*. Concepts Books Publication.

Rosa-Clot, M., Rosa-Clot, P., Tina, G. M., & Ventura, C. (2016). Experimental photovoltaic-thermal Power Plants based on TESPI panel. *Solar Energy, 133*, 305-314. https://doi.org/10.1016/j.solener.2016.03.024

Rosli, M. A. M., Ping, Y. J., Misha, S., Akop, M. Z., Sopian, K., Mat, S., ... & Saruni, M. A. (2018). Simulation study of computational fluid dynamics on photovoltaic thermal water collector with different designs of absorber tube. *J. Adv. Res. Fluid Mech. Therm. Sci, 52*(1), 12-22.

Singh, D. B., Yadav, J. K., Dwivedi, V. K., Kumar, S., Tiwari, G. N., & Al-Helal, I. M. (2016). Experimental studies of active solar still integrated with two hybrid PVT collectors. *Solar Energy, 130*, 207-223. https://doi.org/10.1016/j.solener.2016.02.024

Skoplaki, E., & Palyvos, J. A. (2009). On the temperature dependence of photovoltaic module electrical performance: A review of efficiency/power correlations. *Solar Energy, 83*(5), 614-624. https://doi.org/10.1016/j.solener.2008.10.008

Srivatsan, T. S. (1995). A review of:"Fundamentals of Composites Manufacturing: Materials, Methods and Applications" by A. Brent Strong. *Material and Manufacturing Process, 10*(5), 1121-1122. https://doi.org/10.1080/10426919508935097

Takeichi, T., & Furukawa, N. (2012). Epoxy resins and phenol-formaldehyde resins.

Tiwari, G. N., & Al-Helal, I. M. (2015). Analytical expression of temperature dependent electrical efficiency of N-PVT water collectors connected in series. *Solar Energy, 114*, 61-76. https://doi.org/10.1016/j.solener.2015.01.026

Tripanagnostopoulos, Y., Nousia, T. H., Souliotis, M., & Yianoulis, P. (2002). Hybrid photovoltaic/thermal solar systems. *Solar Energy, 72*(3), 217-234. https://doi.org/10.1016/S0038-092X(01)00096-2

Tripathi, R., Tiwari, G. N., & Dwivedi, V. K. (2016). Overall energy, exergy and carbon credit analysis of N partially covered photovoltaic thermal (PVT) concentrating collector connected in series. *Solar Energy, 136*, 260-267. https://doi.org/10.1016/j.solener.2016.07.002

Tse, K. K., Chow, T. T., & Su, Y. (2016). Performance evaluation and economic analysis of a full scale water-based photovoltaic/thermal (PV/T) system in an office building. *Energy and Buildings, 122*, 42-52. https://doi.org/10.1016/j.enbuild.2016.04.014

Wu, S. Y., Zhang, Q. L., Xiao, L., & Guo, F. H. (2011). A heat pipe photovoltaic/thermal (PV/T) hybrid system and its performance evaluation. *Energy and buildings, 43*(12), 3558-3567. https://doi.org/10.1016/j.enbuild.2011.09.017

Xu, N., Ji, J., Sun, W., Huang, W., Li, J., & Jin, Z. (2016). Numerical simulation and experimental validation of a high concentration photovoltaic/thermal module based on point-focus Fresnel lens. *Applied Energy, 168*, 269-281. https://doi.org/10.1016/j.apenergy.2016.01.077

Yazdanifard, F., Ebrahimnia-Bajestan, E., & Ameri, M. (2016). Investigating the performance of a water-based photovoltaic/thermal (PV/T) collector in laminar and turbulent flow regime. *Renewable Energy, 99*, 295-306. https://doi.org/10.1016/j.renene.2016.07.004

Yunus, C. A., Klein, S., & Beckman, W. (1998). *Heat transfer: a practical approach* (Vol. 141). Boston: WBC McGraw-Hill.

Zondag, H. A. (2008). Flat-plate PV-Thermal collectors and systems: A review. *Renewable and Sustainable Energy Reviews, 12*(4), 891-959. https://doi.org/10.1016/j.rser.2005.12.012

Zondag, H. A., De Vries, D. W., Van Helden, W. G. J., Van Zolingen, R. J. C., & Van Steenhoven, A. A. (2003). The yield of different combined PV-thermal collector designs. *Solar Energy, 74*(3), 253-269. https://doi.org/10.1016/S0038-092X(03)00121-X

Zweben, C. (1998). Advances in composite materials for thermal management in electronic packaging. *Jom, 50*(6), 47-51. https://doi.org/10.1007/s11837-998-0128-6

Zweben, C. H. (2005). Composites: overview.

APPENDICES

APPENDIX 1: Technical Specification of the PV Cell

Technical Specifications:

Tongwei Solar Co.

TW Solar M1585BPERC Monocrystalline Silicon Solar Cells

Mechanical Data and Design

Dimension : 158.75 mm * 79.375 mm ± 0.25 mm

Thickness : 190 ± 30 μm

Front : 5 * 0.7 mm bus bars (silver) and 60 finger grids
Blue anti-reflecting coating (silicon nitride)

Back : Width of back electrode (silver) 1.8 ± 0.3 mm
Back surface field (aluminum)

Tk Voc : (-0.36 ± 0.068) %/K

Tk Isc : (+0.0415 ± 0.0039) %/K

Tk Pmpp : (-0.3467 % ± 0.0085) /K

Rsh > 35 Ω , Irev2 < 0.8 A

Light Intensity Dependence

Take the Voc (Isc) at 1000 W/m2 as the standard, test the range of Voc (Isc) decrease with light intensity.

Intensity (W/m^2)	Uoc	Isc
1000	1.000	1.000
900	0.996	0.903
800	0.991	0.803
600	0.988	0.602
400	0.962	0.403

Solder Ability

Result may be different due to different ribbons, soldering methods and parameters.

Peel Strength Minimum > 1.4 N/mm

Efficiency Parameters

STC (Standard Testing Conditions) : 1000 W/m2, AM 1.5, 25 °C

Specifications subjects to technical changes and tests.

Efficiency (%)	Pmpp (W)	Umpp (V)	Impp (A)
21.8	5.47	0.567	9.648

Uoc (V)	Isc (A)	FF (%)
0.6731	10.188	79.77

APPENDIX 2: The Wiring Diagram of the Experimental Environment

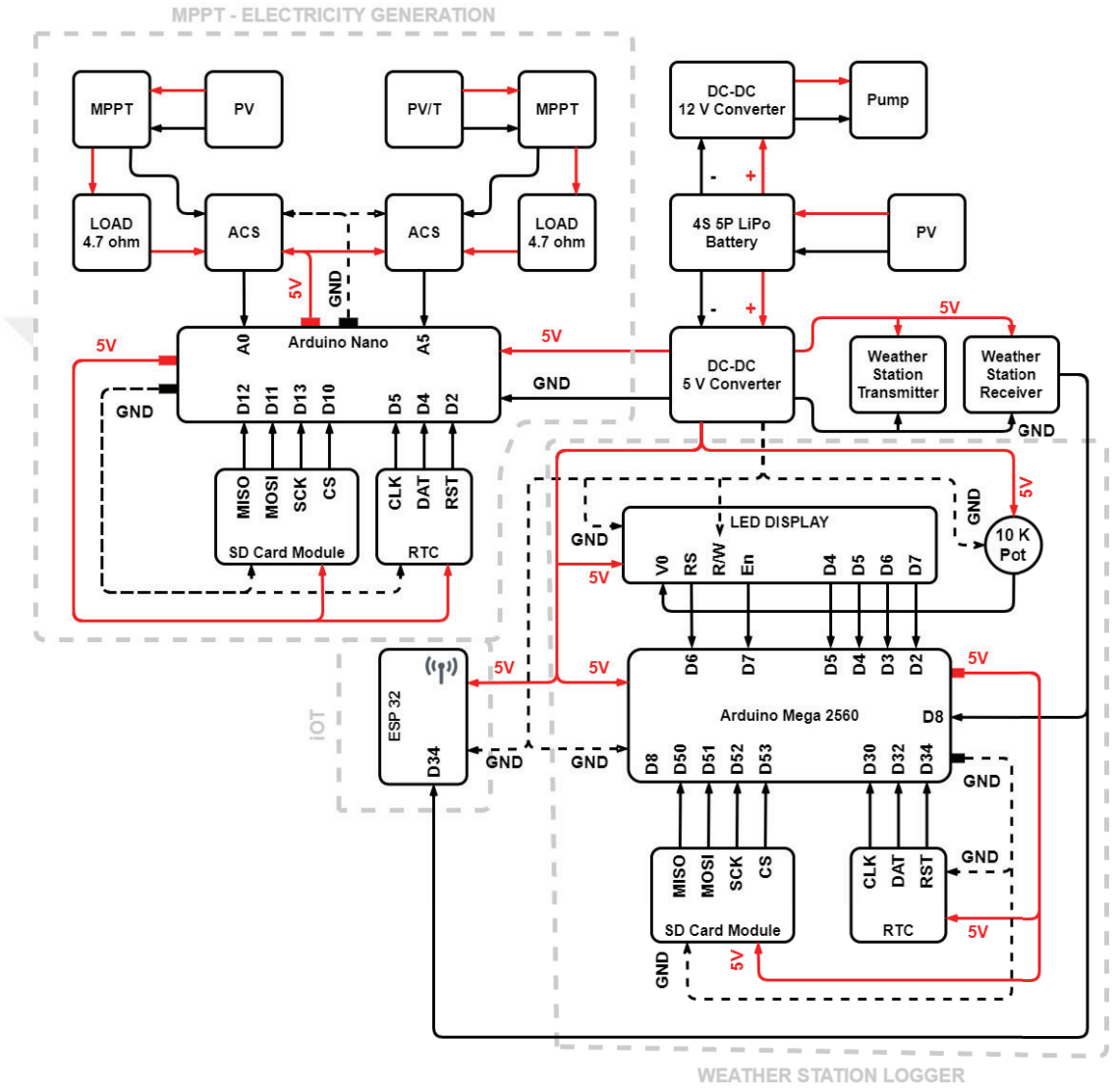

APPENDIX 3: The Source Code of the Weather Station

```
// Calling Libraries.
#include <SPI.h>
#include <SD.h>
#include <Wire.h>
#include <virtuabotixRTC.h>
#include <LiquidCrystal.h>
#include <avr/wdt.h>
// Definitions.
#define FILE_BASE_NAME "Data"
const uint8_t CS_PIN = 53;
File file;
const uint8_t BASE_NAME_SIZE = sizeof(FILE_BASE_NAME) - 1;
char fileName[] = FILE_BASE_NAME "00.txt";
// Definition of the LCD Screen Pins.
const int rs = 7, en = 6, d4 = 5, d5 = 4, d6 = 3, d7 = 2;
LiquidCrystal lcd(rs, en, d4, d5, d6, d7);
#define SHORT_PULSE  500
#define LONG_PULSE  1500
#define SHORT_MARGIN 300
#define LONG_MARGIN 300
// Definition of the RTC Module Pins.
virtuabotixRTC myRTC(30, 32, 34);
// Make a String for Assembling the Data to Log.
String dataString = "";
// Definition of the SD Card Module CS Pin.
const int chipSelect = 53;
```

```
static int wind_dir_degr[]= {0, 23, 45, 68, 90, 113,
135, 158, 180, 203, 225, 248, 270, 293, 315, 338};
int temp_raw;
float temperature;
int val = 0;
unsigned long transition_t = micros();
unsigned long now, duration;
#ifdef DEBUG
  unsigned long short_min = 9999, short_max = 0;
  unsigned long long_min = 9999, long_max = 0;
  unsigned int pulse_buffer[200];
  unsigned int pb_idx = 0;
#endif
#define BUFFER_SIZE  16
byte byte_buffer[BUFFER_SIZE];
byte buffer_idx = 0;
byte sig_seen = 0;
unsigned short shift_register = 0;
byte bit_count = 0;
uint8_t _crc8( uint8_t *addr, uint8_t len)
{
  uint8_t crc = 0;
  while (len--) {
  uint8_t inbyte = *addr++;
  uint8_t i;
  for (i = 8; i; i--) {
  uint8_t mix = (crc ^ inbyte) & 0x80;
  // changed from & 0x01
```

```
 crc <<= 1; // changed from right shift
 if (mix) crc ^= 0x31;// changed from 0x8C;
 inbyte <<= 1; // changed from right shift
 }
 }
 return crc;
}

// Setting Up the Microcontroller.
void setup() {
 // Open Serial Communications and Wait for Port to Open.
 Serial.begin(115200);
 // Wait for serial port to connect.
 while (!Serial) {
  ;
 }
 // Make the LCD Screen Active.
 lcd.begin(16, 2);
 // See If the SD Card is Present and Can be Initialized:
 Serial.print("Initializing SD Card.");
 if (!SD.begin(chipSelect)) {
  Serial.println("Card Failed, or not Present.");
 }
 Serial.println("Card Initialized.");
 // Prints Title With Ending Line Break.
 Serial.println("Weather Station Monitor:");
 // Read Three Sensors and Append to the String:
 dataString= dataString + "Device ID"  +"Battery" +
```

```
"Temperature(C)" + "Humidity(%)" + "Wind Direction(D)" +
"Wind Speed(km/h)" + "Day" + "Month" + "Year" + "Hours" +
"Minute" + "Second";
// Open the File. Note that Only One File can be Open at a Time.
while (SD.exists(fileName)) {
  if (fileName[BASE_NAME_SIZE + 1] != '9') {
    fileName[BASE_NAME_SIZE + 1]++;
  } else if (fileName[BASE_NAME_SIZE] != '9') {
    fileName[BASE_NAME_SIZE + 1] = '0';
    fileName[BASE_NAME_SIZE]++;
  }
} else {
  Serial.println(F("Can't Create File Name"));
  return;
}
// Open the SD Card to Taking Log.
file = SD.open(fileName, FILE_WRITE);
// Check the Current Status of the SD Card Module.
if (!file) {
  Serial.println(F("Open Failed."));
  return;
}
Serial.print(F("Opened."));
Serial.println(fileName);
// If the File is Available, Write to It:
if (file) {
  file.println(dataString);
  file.close();
```

```
  Serial.println(dataString);
 }
 // Set the Current Date, and Time in the Following Format:
 // Seconds, Minutes, Hours, Day of the Week, Day of the Month, Year.
 myRTC.setDS1302Time(0, 30, 2, 3, 9, 6, 2021);
}

// Declare Reset Function at Address 0 - Must be Above the Loop.
void(* resetFunc) (void) = 0;

// Preparation of the Loop.
void loop() {
 // Reset the Embedded Card End of the Day.
 // 1 Second = 1000 Millisecond.
 if (millis() > 5400000) {
  Serial.print("Reset.");
  wdt_enable( WDTO_8S);
 }
 int newVal=0;
 dataString = "";
 for(int i=0; i < 10; i++) {
  newVal += digitalRead(8) ? 1 : 0;
  delayMicroseconds(5);
 }
 newVal = (newVal + 5) / 10;
 now = micros();
 if(transition_t <= now){
  duration = now - transition_t;
```

```
} else {
  duration = (~transition_t) + now;
}
if(newVal != val) {  // then transitioning state
  transition_t = now;
  val = newVal;
  if(duration < (SHORT_PULSE - SHORT_MARGIN)
  || duration > (LONG_PULSE + LONG_MARGIN)) {
  // Meaningless pulse
  return;
  }
  if(newVal == 1) {
  // Rising Edge of a Pulse (0 -> 1)
  } else {
    // falling edge of a pulse (1 -> 0)
    if (duration >= (SHORT_PULSE - SHORT_MARGIN) &&
    duration <= (SHORT_PULSE + SHORT_MARGIN) ) {
      // short pulse is binary '1'
      shift_register = (shift_register << 1) | 0x01;
      bit_count++;
      #ifdef DEBUG
      if(duration < short_min) short_min = duration;
      if(duration > short_max) short_max = duration;
      if(pb_idx < 200) pulse_buffer[pb_idx++] = duration;
      #endif
    } else if (duration >= (LONG_PULSE - LONG_MARGIN) &&
    duration <= (LONG_PULSE + LONG_MARGIN)) {
      // long pulse is binary '0'
```

```
    shift_register = (shift_register << 1);
    bit_count++;
    #ifdef DEBUG
    if(duration < long_min) long_min = duration;
    if(duration > long_max) long_max = duration;
    if(pb_idx < 200) pulse_buffer[pb_idx++] = duration;
    #endif
   }
  }
  // Look for signature of 0xfa (4 bits 0xf0 pre-amble + 0xa)
  if((shift_register & 0xff) == 0xfa && buffer_idx == 0) {
   // Found signature - discard pre-amble and leave 0x0a.
   shift_register = 0x0a;
   bit_count = 4;
   sig_seen = 1;  // Flag that the signature has been seen.
   #ifdef DEBUG
   pb_idx = 0;
   #endif
  } else if(bit_count == 8 && sig_seen) {
   // Got a byte, so store it if we have room.
   if(buffer_idx < BUFFER_SIZE)
   byte_buffer[buffer_idx++] = (byte)(shift_register & 0xff);
   else
   Serial.println("Overflow on byte");
   shift_register = 0;
   bit_count = 0;
  }
 } else {
```

```
if(duration > 5000) {
 if (buffer_idx > 0) {
  Serial.print("A New Data has been Found.");
  Serial.println(buffer_idx);
  for(int i = 0; i < buffer_idx; i++) {
   for (byte mask = 0x80; mask; mask >>= 1) {
   Serial.print(mask & byte_buffer[i] ? '1' : '0');
   }
   Serial.print(' ');
   Serial.println(byte_buffer[i]);
  }
  if(buffer_idx >= 10 && _crc8(byte_buffer, 9) == byte_buffer[9]) {
   Serial.println("CRC Passed");
  }
  int device_id = (byte_buffer[0] << 4 & 0xf0) | (byte_buffer[1] >> 4);
  Serial.print("Device ID=");
  Serial.println(device_id);
  int battery_low = (byte_buffer[8] >> 4) == 1;
  Serial.print("Battery "); battery_low ?
  Serial.println("LOW") : Serial.println("OK");
  temp_raw = ((byte_buffer[1] & 0x03) << 8) | byte_buffer[2];
  // only 10 bits, discard top bits
  temperature = (temp_raw - 400) * 0.1f;
  Serial.print("Temperature=");
  Serial.println(temperature);
  int humidity = byte_buffer[3];
  Serial.print("Humidity=");
  Serial.print(humidity);
```

```
Serial.println("%");
int direction_deg = wind_dir_degr[byte_buffer[8] & 0x0f];
Serial.print("Wind Direction=");
Serial.print(direction_deg);
Serial.println("Deg");
float speeds = (byte_buffer[4] * 0.30f) * 3.6f;
Serial.print("Wind Speed=");
Serial.print(speeds);
Serial.println("km/h");
float gust = (byte_buffer[5] * 0.30f) * 3.6f;
// Here, obtained data from the weather station are
// printed on the LCD screen.
Serial.print("Wind Gust=");
Serial.print(gust);
Serial.println("km/h");
int rain_raw = ((byte_buffer[6] & 0x0f) << 8) | byte_buffer[8];
float rain = rain_raw * 0.3f;
Serial.print("Rain=");
Serial.print(rain);
Serial.println("mm");
buffer_idx = 0;
myRTC.updateTime();
file = SD.open(fileName, FILE_WRITE);
if (file) {
 file.println(dataString);
 file.close();
 Serial.println(dataString);
}
```

```
      else {
        Serial.println("error opening datalog.txt");
      }
    }
    #ifdef DEBUG
    for(int i = 0; i < pb_idx; i++) {
    Serial.print("Pulse ");
    Serial.print(i);
    Serial.print(' ');
    Serial.println(pulse_buffer[i]);
    }
    Serial.print("Short ");
    Serial.print(short_min);
    Serial.print(' ');
    Serial.println(short_max);
    Serial.print("Long ");
    Serial.print(long_min);
    Serial.print(' ');
    Serial.println(long_max);
    short_min = long_min = 9999;
    short_max = long_max = 0;
    #endif
    shift_register = 0;
    bit_count = 0;
    sig_seen = 0;
   }
   // Serial.flush();  }
} // end loop()
```

APPENDIX 4: The Wiring Diagram of the Weather Station

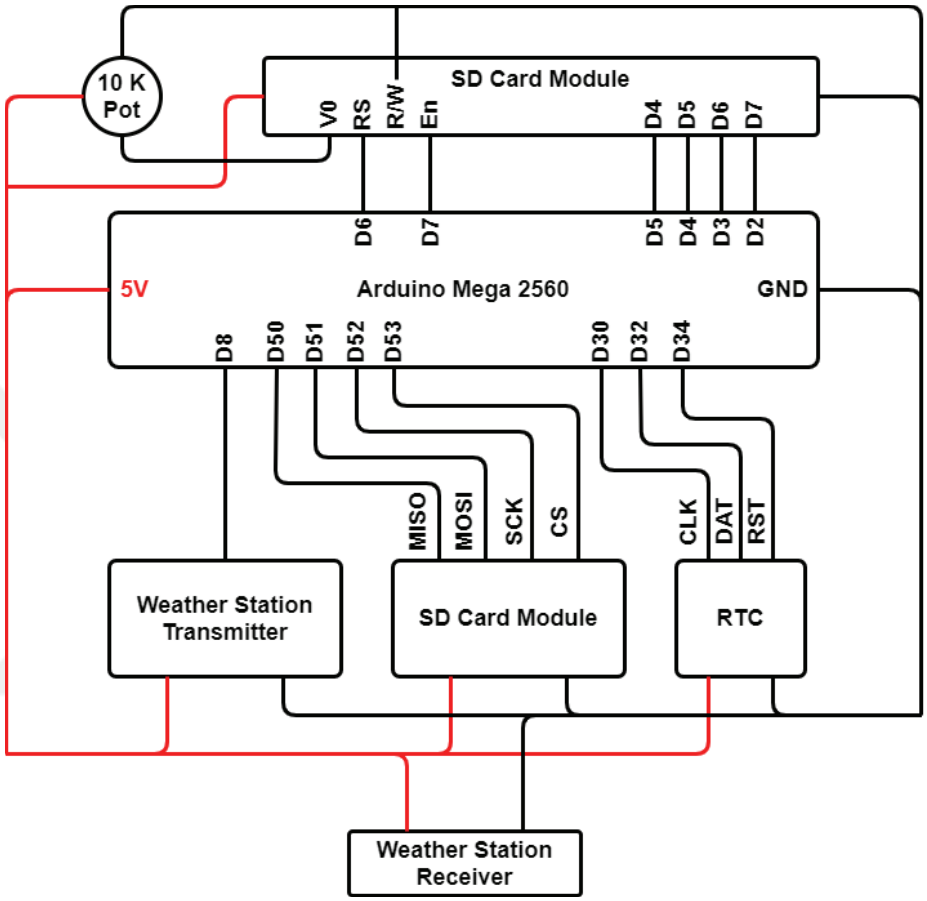

APPENDIX 5: The Source Code of the Power Generation Meter

```
// Calling Library.
#include <virtuabotixRTC.h>
#include <SPI.h>
#include <SD.h>

// Definition of the RTC Module Pins.
virtuabotixRTC myRTC(5, 4, 2);

// Definitions
String dataString = "";
File myFile;
const int chipSelect = 10;
// Define the Microcontroller Pin A0 as Voltage Input (Vin) for the PV Module.
#define VIN A0
// Define the Microcontroller Pin A0 as Voltage Input (Vin) for the PVT Module.
#define VINN A5
// Supply Voltage is From 4.5 to 5.5 V.
const float VCC   = 5.0;
// Enter the Sensor Model Number.
const int model = 2;
// Set the Current.
float cutOffLimit = 1.01;
float sensitivity[] ={
0.185,// for ACS712ELCTR-05B-T
0.100,// for ACS712ELCTR-20A-T
0.066// for ACS712ELCTR-30A-T
```

```
};
// Set Quiescent Output Voltage of 0.5V.
const float QOV =   0.5 * VCC;
// Internal Variable for Voltage of PV Module .
float voltage;
// Internal Variable for Voltage of PVT Module .
float voltagee;

// Setting Up The Microcontroller.
void setup() {
    // Open Serial Communications and Wait for Port to Open.
    Serial.begin(9600);
    // Check the SD Card Module
    Serial.print("Initializing SD Card.");
    if (!SD.begin()) {
        Serial.println("Initialization Failed!");
        return;
    }
    Serial.println("Initialization Done.");
    // Create/Open the File for Logs.
    myFile = SD.open("MPPT.txt", FILE_WRITE);
    if (myFile) {
        // Performing Test for the Current Status of the SD Card Module.
        myFile.println("Writing to Test Data.");
        myFile.close();
        Serial.println("Done.");
    } else {
        // If the File didn't Open, Print an Error.
```

```
        Serial.println("Error Opening MPPT.txt");
    }
}

// Preparation of the Loop.
void loop() {
    // For the PV Module.
    float voltage_raw =   (5.0 / 1023.0) * analogRead(VIN);
    // Read the Voltage from the Sensor.
    voltage =  voltage_raw - QOV + 0.012 ;
    // 0.000 is a Value to Make Voltage Zero when there is No Current.
    float current = voltage / sensitivity[model];
    if (abs(current) > cutOffLimit ){
        Serial.print("V: ");
        Serial.print(voltage,3);
        // Print Voltage with 3 Decimal Places.
        Serial.print("V, I: ");
        Serial.print(current,2);
        // Print the Current with 2 Decimal Places.
        Serial.println("A");
    }else{
        Serial.println("No Current.");
    }
    // For the PVT Module.
    float voltage_raww = (5.0 / 1023.0)* analogRead(VINN);
    // Read the Voltage from the Sensor.
    voltagee =  voltage_raww - QOV + 0.012 ;
    // 0.000 is a Value to Make Voltage Zero when there is No Current.
```

```
float currentt = voltagee / sensitivity[model];
if(abs(current) > cutOffLimit ){
    Serial.print("V: ");
    Serial.print(voltagee,3);
    // Print Voltage with 3 Decimal Places.
    Serial.print("V, I: ");
    Serial.print(currentt,2);
    // Print the Current with 2 Decimal Places.
    Serial.println("A");
}else{
    Serial.println("No Current.");
}
// Update the RTC Module Time.
myRTC.updateTime();
// Preparation Values for the Taking Log.
dataString=String(myRTC.dayofmonth)+", "+String(myRTC.month)+",
"+String(myRTC.year)+", "+String(myRTC.hours)+",
"+String(myRTC.minutes)+", "+String(myRTC.seconds)+",
"+String(current)+", "+String(currentt)+",";
// Open the File to Taking Log.
myFile = SD.open("MPPT.txt", FILE_WRITE);
if (myFile) {
    Serial.print("Writing the Data.");
    myFile.println(dataString);
    // Close the File:
    myFile.close();
    Serial.println("Done.");
} else {
```

```
        Serial.println("Error Opening MPPT.txt");
    }
    // Write Values to the Serial Monitor.
    Serial.println(dataString);
    // Definition of the Delay.
    delay(1000);
}
```

APPENDIX 6: The Wiring Diagram of the Power Generation Meter

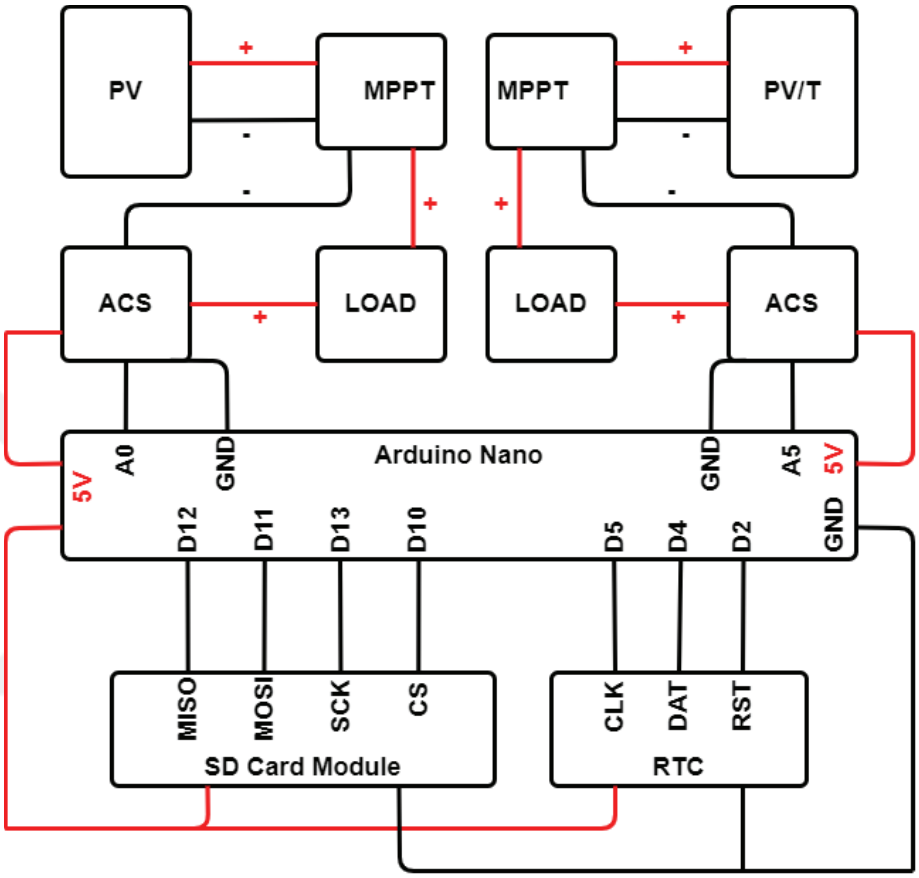

APPENDIX 7: The Wiring Diagram of the Battery

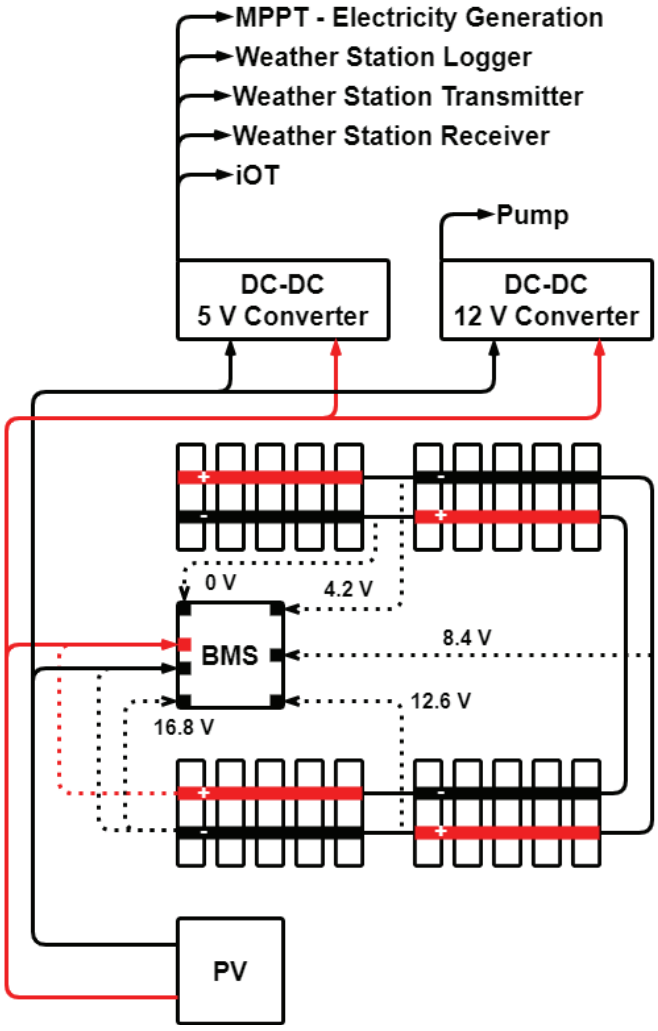

APPENDIX 8: Infrared Camera Pictures on 23th February

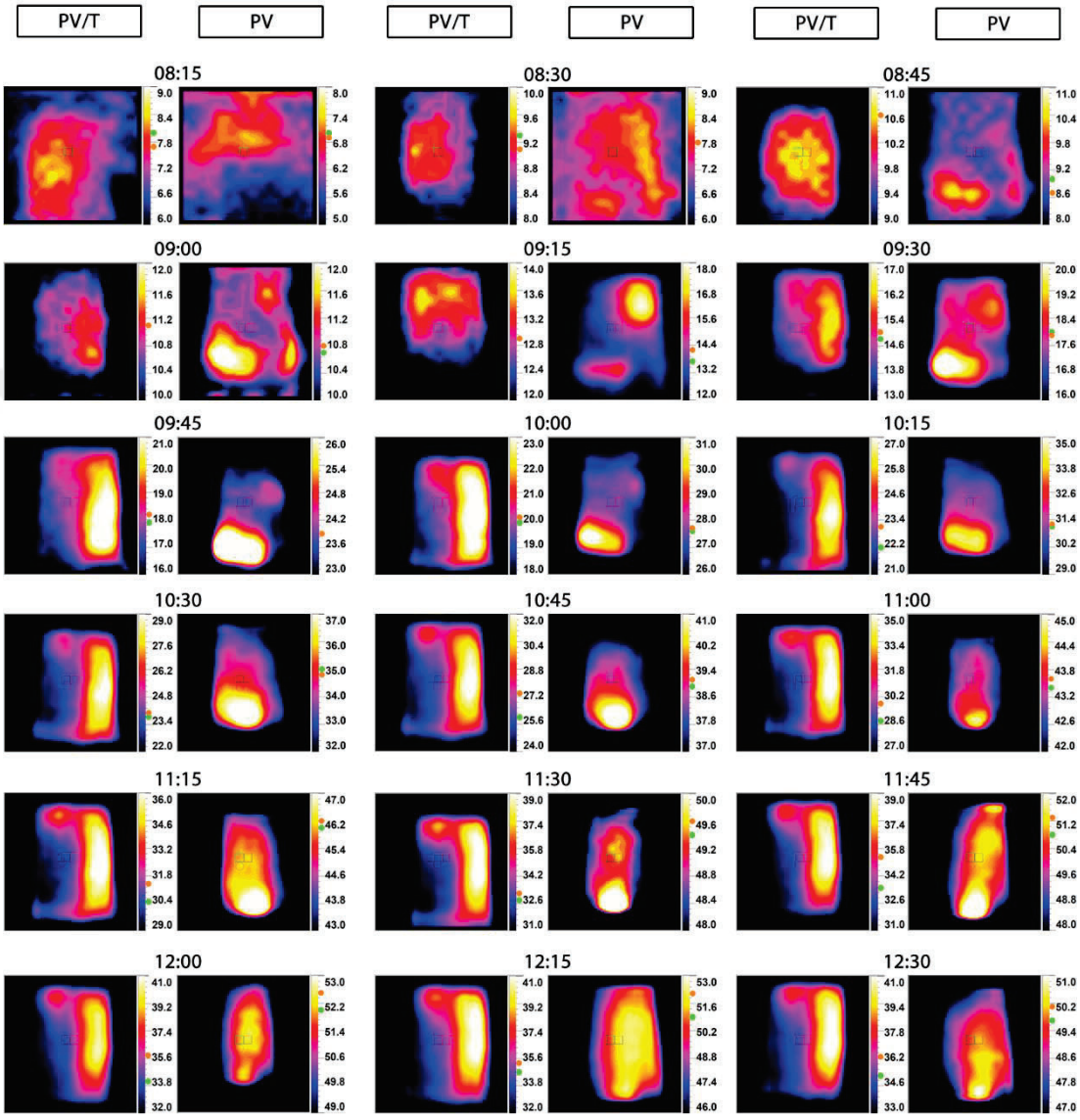

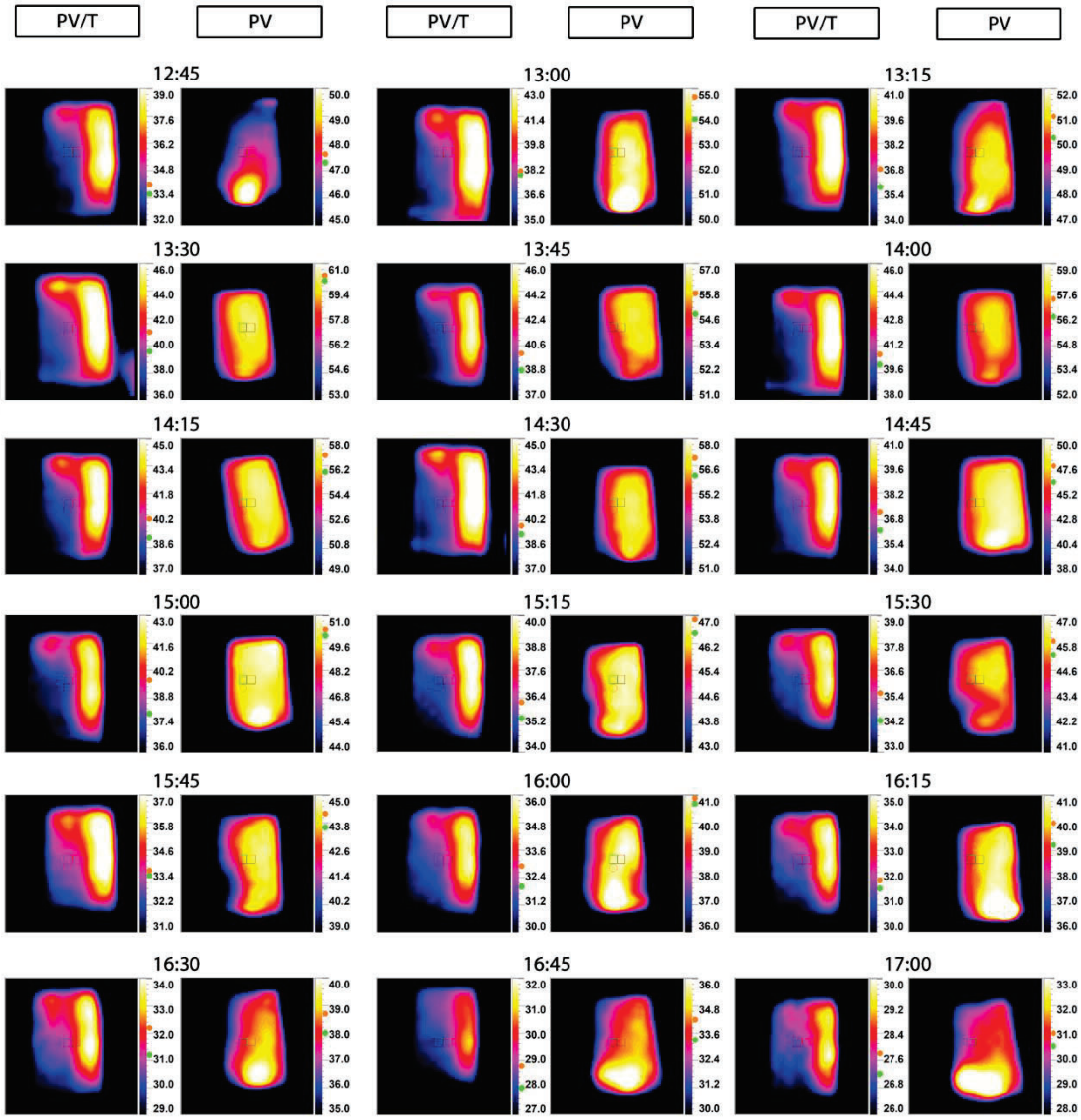
PV/T
PV
PV/T
PV
PV/T
PV
12:45
13:00
13:15
13:30
13:45
14:00
14:15
14:30
14:45
15:00
15:15
15:30
15:45
16:00
16:15
16:30
16:45
17:00

APPENDIX 9: Infrared Camera Pictures on 21th March

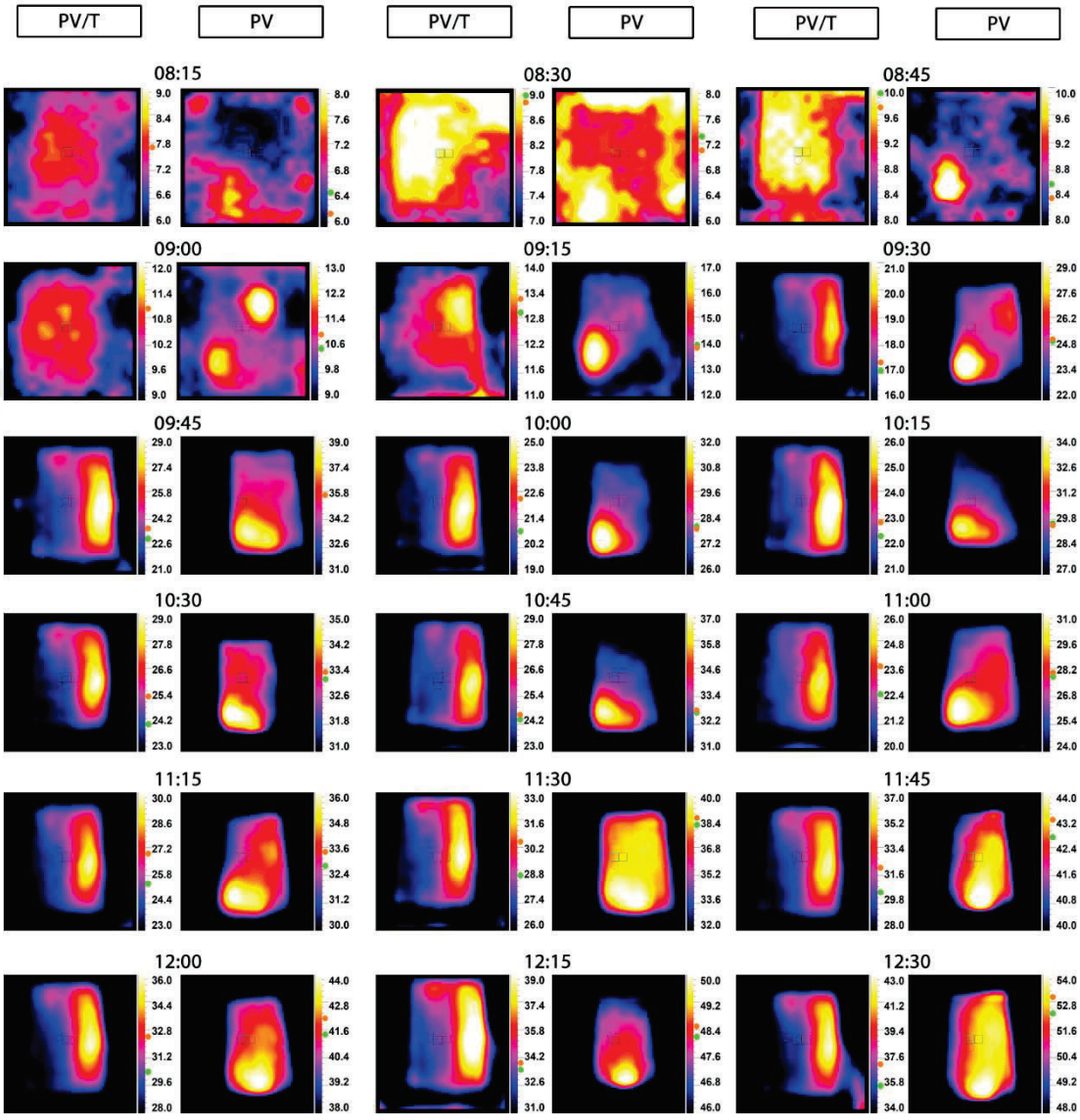

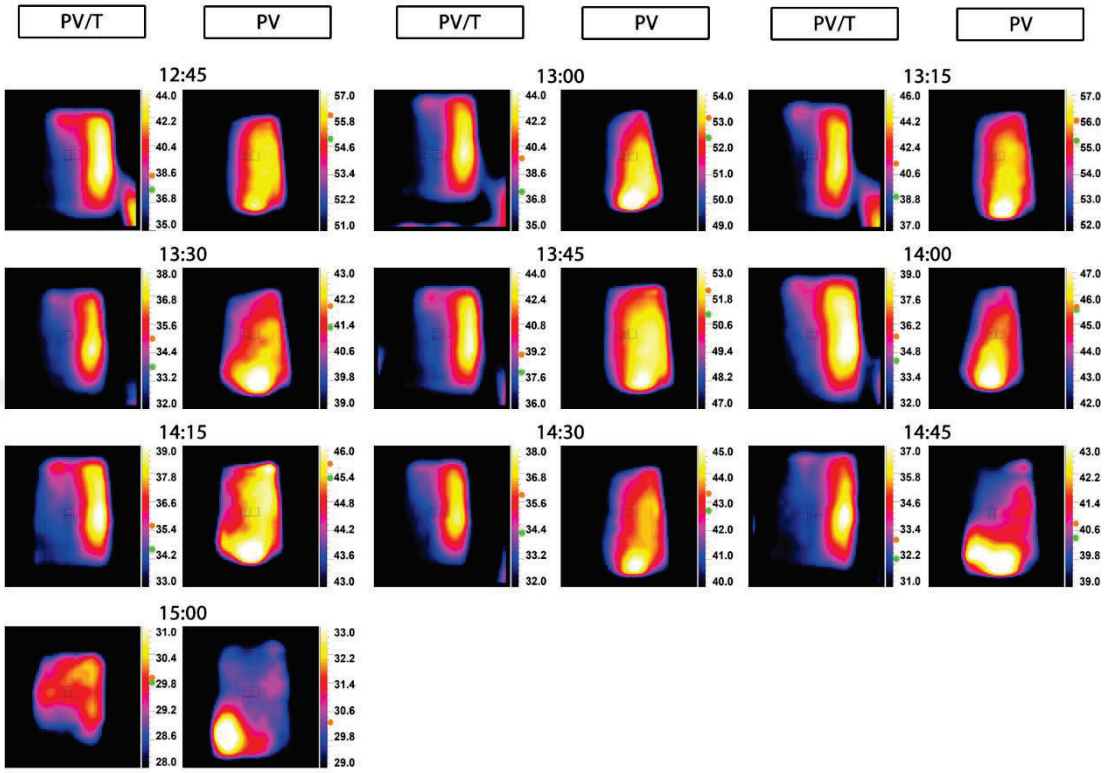
PV/T
PV
PV/T
PV
PV/T
PV
12:45
13:00
13:15
13:30
13:45
14:00
14:15
14:30
14:45
15:00

APPENDIX 10: Infrared Camera Pictures on 28th April

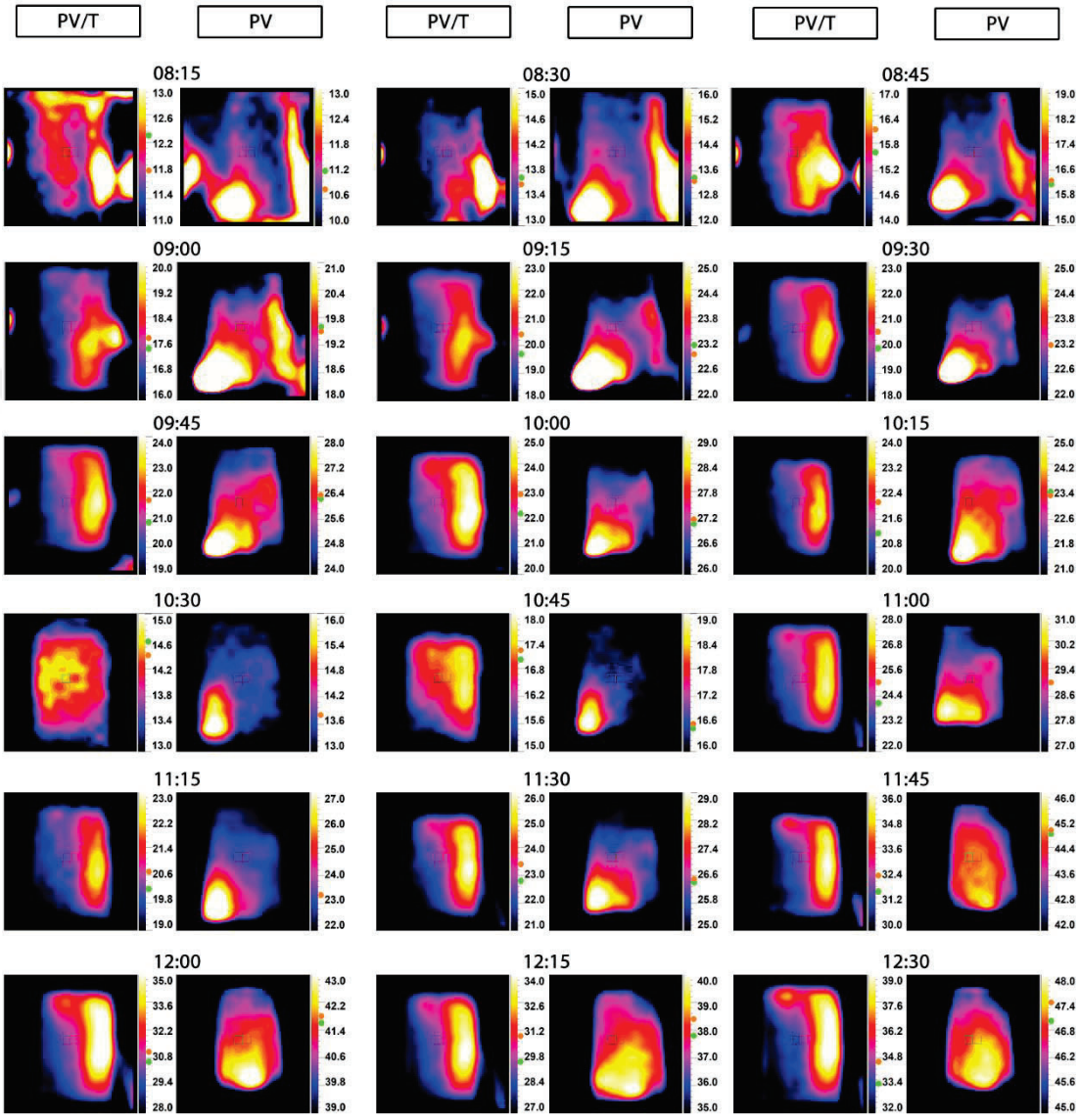

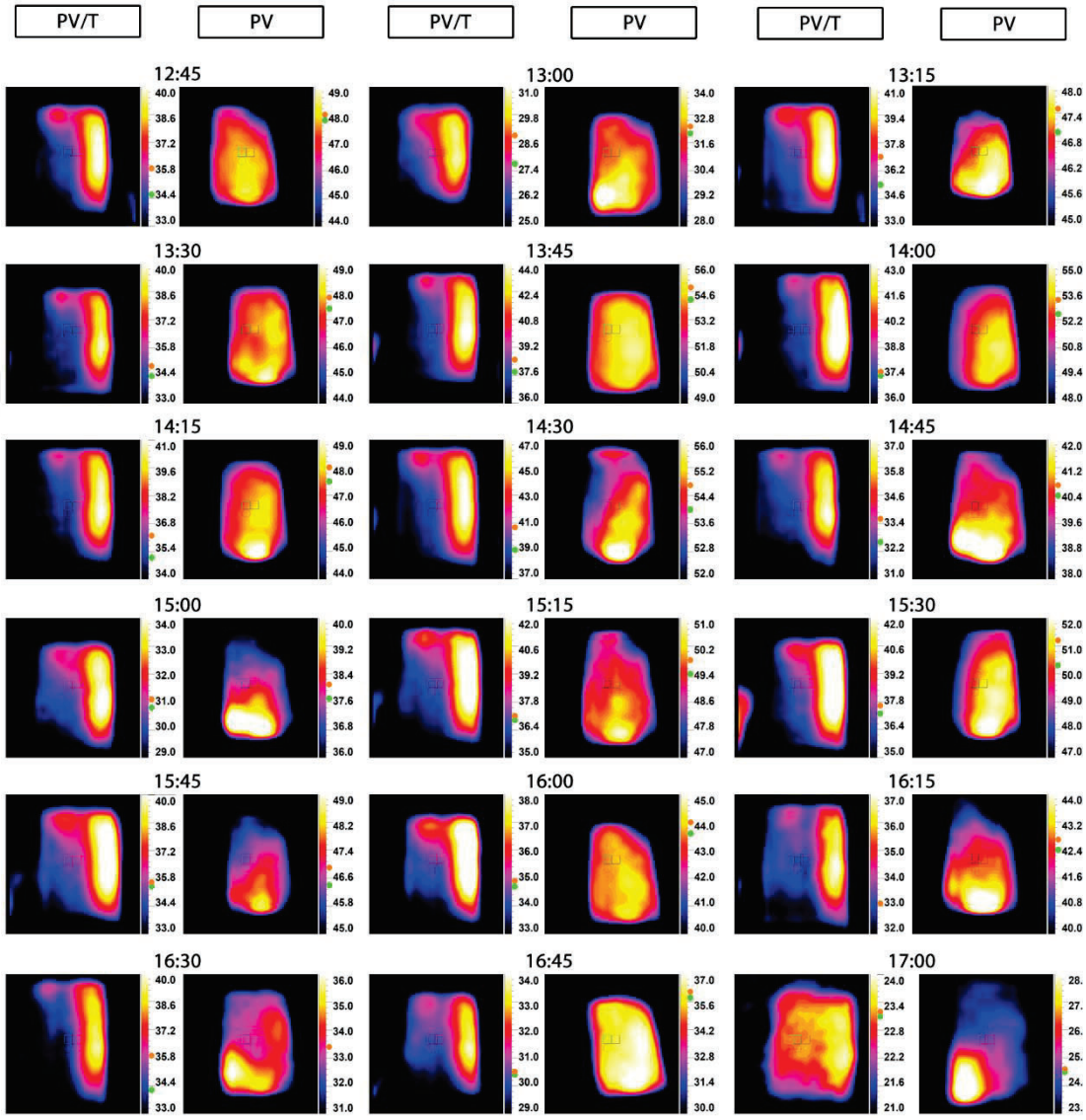
PV/T
PV
PV/T
PV
PV/T
PV
12:45
13:00
13:15
13:30
13:45
14:00
14:15
14:30
14:45
15:00
15:15
15:30
15:45
16:00
16:15
16:30
16:45
17:00